

Investigation of electronic conduction and magnetism in ferromagnetic Gd and ferrimagnetic GdCo alloy nanostructures

A Thesis Submitted for the
Degree of Doctor of Philosophy
in University of Calcutta,
Kolkata

by

Manotosh Chakravorty



Department of Condensed Matter Physics and Material Sciences
S N Bose National Centre for Basic Sciences

Saltlake, Kolkata-700098, India.

September, 2017

Dedicated to my family.....

Acknowledgement

Prof. Arup Kumar Raychaudhuri deserves a special thanks to complete my thesis. He has supervised me from the first day to the end. Without his suggestions initially it was impossible for me to understand this scientific world. I learned from him to do perfect and precise experiments. Except his support it was very difficult for me to explain and connect the experimental results with proper physics.

Next I want to acknowledge my wife Putul. Without her constant support it was difficult to overcome the problems and obstacles which had arisen during my Ph.D. She continuously stayed beside me at the days which were full of frustrations. I got lots of help from her at the time of experiments.

My lab mates are also very helpful. I gathered lots of knowledge from my seniors. I discussed problems with my friends Rajib and Shahnewaz. Juniors were also very helpful.

The technical cell staffs especially Joy and Dipankar have helped me lots at the time of sample preparation and experiment.

I want to thanks Prof. Pratip Kumar Mukhopadhyay and his student Sandeep Agarwal for helping me to prepare alloy samples.

Finally I should thank my family for giving me their constant support. Without the intense desire of my late father Manik Krishna Chakravorty I would have never come to do Ph.D.

I want to acknowledge to the Department of Science and Technology (DST) for financial support and CSIR Govt. of India for fellowship.

Publications:

1. **Temperature dependent resistivity of platinum–carbon composite nanowires grown by focused ion beam on SiO₂/Si substrate**, Manotosh Chakravorty, K. Das, A. K. Raychaudhuri, J. P. Naik and P.D. Prewett, *Microelectronic Engineering*, **88**, 3360 (2011).
2. **Low field magnetoresistance of gadolinium nanowire**, Manotosh Chakravorty and A. K. Raychaudhuri, *J. Appl. Phys.*, **115**, 054308 (2014).
3. **Magnetoresistance of polycrystalline gadolinium with varying grain size**, Manotosh Chakravorty and A. K. Raychaudhuri, *J. Appl. Phys.*, **117**, 034301 (2015).
4. **Bose Einstein condensation of Magnons in nanostructured films of Gd at low temperature and its manifestations in electrical resistivity and magnetoresistance**, Manotosh Chakravorty, A. K. Raychaudhuri, Tapati Sarkar and Mikael Svante Andersson, *J. Phys.: Condens. Matter* **29**, 255701 (2017).
5. **Domain wall motion as a tool to find out the value of anisotropy energy in magnetic thin film with micro/nano constriction**, Manotosh Chakravorty and A. K. Raychaudhuri (submitted to *Applied Phys. Let.*).
6. **Size induced change of compensation temperature in Gd_xCo_{1-x} (x = 0.4) alloy nanowire (diameter ~ 100 nm)**, Manotosh Chakravorty and A. K. Raychaudhuri. (ready for submission).

Contents

Chapter 1: Introduction	1-26
1.1. Motivation	2
1.2. Unique properties of Gd	2
1.2.1. Electronic structure	2
1.2.2. Room temperature T_C	3
1.2.3. Anisotropy energy (E_A)	3
1.2.4. Spin structure	4
1.2.5. Spin reorientation transition temperature T_{SR}	4
1.2.6. Domain wall thickness δ	5
1.3. Magnetoresistance (MR) study of Gd	6
1.4. Bose Einstein condensation (BEC) of quasi-particle magnon	8
1.4.1. Condition for BEC of quasi particle	8
1.4.2. Magnon BEC in different systems	8
1.4.3. Magnon BEC in nanostructures	10
1.4.4. Magnon BEC of Gd nanocrystals	11
1.5. Current driven domain wall motion	13
1.5.1. Theoretical work	13
1.5.2. Experimental evidences	14
1.5.3. Experimental evidence from the resistance change	16
1.6. Magnetism in binary alloy GdCo	17
1.6.1. Importance of GdCo	18
1.6.2. Magnetization compensation temperature T_{cm}	20
1.6.3. Tuning of T_{cm}	21
Chapter 2: Sample preparation and Experimental techniques	27-46
2.1. Sample preparation	28
2.1.1. Thermal evaporation	28
2.1.2. Electron beam evaporation	29
2.1.3. Integrated lithography technique	29
2.1.4. Electrical contact pad preparation	30
2.1.5. Arc furnace	32
2.1.6. Electrodeposition	33
2.2. Characterization	35
2.3. Physical measurements	38
2.3.1. Magnetization measurement	38
2.3.2. Electrical resistance measurement	40
2.3.3. Magnetoresistance (MR) measurement	41
Chapter 3: Magnetoresistance of polycrystalline Gadolinium with varying grain size	47-61
3.1. Introduction	48
3.2. Sample preparation	48
3.3. Characterization and measurement technique	49
3.3.1. Grain size analysis by AFM and SEM	49
3.3.2. Crystal structure analysis by XRD	50

3.3.3. Electrical measurements	52
3.4. Resistance measurement and analysis	52
3.5. Magnetization measurement and analysis	53
3.6. Magnetoresistance measurement and analysis	55
3.6.1. Temperature dependence	55
3.6.2. Field dependence	56
3.7. Discussion	58
3.8. Conclusion	60
Chapter 4: Low field magnetoresistance of Gadolinium nanowire	62-70
4.1. Introduction	63
4.2. Sample preparation and characterization	63
4.3. Electrical resistance and MR measurement techniques	64
4.4. Resistance measurement and analysis	64
4.5. Magnetoresistance measurement and analysis	65
4.6. Discussion	67
4.7. Conclusion	69
Chapter 5: Proposed Bose Einstein condensation of Magnons in nanostructured films of Gd at low temperature and its manifestations in electrical resistivity and magnetoresistance	71-81
5.1. Introduction	72
5.2. Experimental	73
5.3. Magnetization	73
5.4. Softening of spin wave stiffness constant D	74
5.5. Resistivity	75
5.6. Magnetoresistance	77
5.7. AC-susceptibility	79
5.8. Conclusion	80
Chapter 6: Current driven magnetic domain wall motion in a nanoconstriction on a Gd microstrip and its application to find out the value of anisotropy energy	82-90
6.1. Introduction	83
6.2. Experimental	84
6.3. Current driven resistance change	85
6.4. Domain wall resistance R_W	86
6.5. Calculation of domain wall thickness δ	87
6.6. Anisotropy energy E_A calculation	88
6.7. Conclusion	89
Chapter 7: Size induced change of compensation temperature in Gd_xCo_{1-x} ($x = 0.4$) alloy nanowire (diameter ~100 nm)	91-102
7.1. Introduction	92
7.2. Experimental	92
7.3. Magnetization	94
7.3.1. Temperature dependence of magnetization: $M(T)$ vs. T	94
7.3.2. Magnetic field dependence of M	95

7.3.3. Saturation M_S and Coercive field H_C	96
7.3.4. Angular dependence of $M-H$ curve in nanowires	96
7.4. Anisotropy energy E_A calculation	98
7.5. Discussion	99
7.6. Conclusion	101
Chapter 8: Summary and conclusion	103-104
Appendix-1: Resistivity of Platinum (Pt) nanowire (NW) grown by FIB	105
Appendix-2: Curie temperature (T_C) finding by Arrott plot	108
Appendix-3: Magnon number density calculation	110
Appendix-4: Domain wall resistance of constricted nonuniform structure	111

List of Figures:

Chapter 1

- FIG. 1.1.** Magnetocrystalline anisotropy constant of Gd. Reprinted with permission 3
- FIG. 1.2.** (a) Schematic diagram of magnetization direction. θ is the angle between c-axis and saturation magnetization M_S . The applied field H makes an angle φ with M_S . Easy cone and basal plane is marked in the figure. (b) Plot of the easy angle (θ_0) between c-axis and magnetization of Gd as a function of temperature. Reprinted with permission 4
- FIG. 1.3.** (a) Specific heat and (b) temperature derivative of basal plane resistance of Gd in magnetic field parallel to c-axis. Reprinted with permission from 5
- FIG. 1.4.** Temperature dependence of (a) DW energy γ_w and (b) DW thickness δ of single crystalline Gd. Reprinted with permission 6
- FIG. 1.5.** Magnetoresistance effects of Gd single crystal as a function of temperature (a) for the a-axis sample. (b) c-axis sample and (c) for 45° to c-axis sample. Dotted curves are k_1, k_2, k_3 and k_4 . Broken curve is the calculated ones for $H//c$. (d) Magnetoresistance of Gd polycrystalline sample. Dotted curves are the experimental and the calculated ones for the difference between the longitudinal and the transverse effect. Reprinted with permission 7
- FIG. 1.6.** The temperature dependence of the magnetoresistance coefficient of Gd. Reprinted with permission 7
- FIG. 1.7.** The low-temperature magnetizations of (a) TlCuCl_3 and (b) KCuCl_3 measured at various external fields for $H \parallel b$. (a) and (b) are reprinted with permission 9
- FIG. 1.8.** (a) Magnetic torque measurement of $\text{Ba}_3\text{Cr}_2\text{O}_8$ at 600 mK. The second derivative of torque/field, shown in the inset, shows two prominent extrema, indicative of the two transitions. (b) Force magnetometry measurement at 600 mK. These data are qualitatively similar to the torque measurement. (c) The phase diagram of $\text{Ba}_3\text{Cr}_2\text{O}_8$ for the $H \parallel c$ orientation. Figures are reprinted with the permission 10
- FIG. 1.9.** Division of the temperature vs particle length plane into three regions. Reprinted with the permission 11
- FIG. 1.10.** (a) Comparison between the observed (symbols) and theoretical [continuous curves, yielded by Eqn. 1.9] temperature variations of magnetization at fixed fields in the range 2.2 – 90 kOe in nanocrystalline Gd with an average grain size of 12 nm. The inset illustrates that, unlike the BEC formalism, the conventional spin-wave theory fails to describe $M(T)$ over an extended temperature range. (b) The total specific heat $C_H(T)$ at a few representative fields for $d = 12$ nm. Note that the $C_{H=20 \text{ kOe}}(T)$ and $C_{H=0}(T)$ data are shifted up by 2.5 and 5.0 J/molK, respectively, with respect to that taken at $H = 40$ kOe. The continuous theoretical curves are obtained by adding the (Sommerfeld) electronic, (Debye) lattice and (BEC) magnon C_{mag} contributions to $C_H(T)$. The bottom inset shows $C_{mag}(T)$, the slope change at T_C , predicted by the BEC theory, and the increase in, and progressive smearing of, T_C with H . The top inset displays the magnetic entropy change $-\Delta S_{mag}$ for a few representative ΔH values (open symbols), obtained from $M_H(T)$, plotted against $[T/T_{BE}(H=0)]^{3/2}$ for $d = 12$ nm. The straight lines serve to highlight the characteristic BEC $T^{3/2}$ variation of entropy for $T \ll$

T_C . $-\Delta S_{mag}$ at $\Delta H = 20$ kOe (solid circles), calculated from $C_H(T)$, agrees quite well with that calculated from $M_H(T)$ (open squares). Reprinted with the permission 12

FIG. 1.11. Scaling of the magnon BE condensate fraction with $(T/T_{BE})^{3/2}$ at different fields for $d = 12$ nm. The inset highlights the scaling of $T_C(H)$ with $[\langle n_0(T = 1.8K, H) \rangle / V(H)]^{2/3}$. (b) The BEC transition temperature T_C obtained from $M_H(T)$ and $C_{mag}(T, H)$ plotted against $H^{2/3}$ for $d = 12$ and 18 nm. The bottom inset depicts the temperature variations of the normalized chemical potential $\mu/k_B T$ at various fixed field values. Reprinted with the permission 12

FIG. 1.12. Transverse magnetoresistance, $\Delta\rho_{\perp}(T)$, calculated from the ‘in-field’ and ‘zero-field’ resistivity at various fixed fields, as a function of temperature for the nanocrystalline Gd sample with average grain size (a) $d = 12$ nm and (b) $d = 18$ nm. Reprinted with the permission 13

FIG. 1.13. (a) A conduction electron of spin \vec{s} crosses a 180° domain wall. (b) Analogy with a linearly polarized microwave propagating along a twisted waveguide. Reprinted with the permission 14

FIG. 1.14. Measured values of the critical current density j_C of $N_{81}Fe_{19}$ films vs. film thickness w . The best-fitted straight line has a slope -2.1 and gives $j_C = 1.18 \times 10^{10} \text{ A/m}^2$ for $w = 263$ nm. Reprinted with the permission 15

FIG. 1.15. (a) Polar Kerr hysteresis loop of our F1/Cu/F2 spin valves with PMA measured in a continuous film. (b) Schematic diagram of a top view of the device. (c) EHE minor hysteresis loop corresponding to the reversal of the free layer in a $200 \times 200 \text{ nm}^2$ Hall cross. A small EHE jump corresponding to DW motion over 10 nm is indicated. The EHE values (1) to (4) refer to the positions indicated in Fig. 1(d). (d) Bubble like behaviour of an ideal 1D Bloch DW in a magnetic Hall cross. The electron flow direction is indicated by the horizontal arrows. EHE as a function of the applied dc current for fields (e) $H_{fre} = -10$ Oe, (f) $H_{fre} = -40$ Oe, and (g) $H_{fre} = -60$ Oe. Measurements have been done by increasing the current from $I = 0$ to $I = \pm 3$ mA and then reducing it to $I = 0$, with a DW initially pinned at position (2). The negative (closed symbols) and positive (open symbols) current measurements have been realized independently. The states (1) to (4) refer to the positions in FIG. 1.15(d). The small Joule heating contribution has been subtracted. Reprinted with the permission 16

FIG. 1.16. $I - V$ measurements for (a) necked NiFe wires and (b) necked Ni wires with constriction widths of (i) 50 nm, (ii) 100 nm, (iii) 150 nm, (iv) 200 nm, and (v) 250 nm. In the insets of (a) and (b) the average critical current density is plotted as a function of constriction width for NiFe and Ni, respectively. Micromagnetic simulations for necked NiFe wires with constriction widths of (c) 50 nm, (d) 100 nm, (e) 250 nm, and (f) 300 nm. Reprinted with the permission 17

FIG. 1.17. Temperature dependence of isothermal magnetic entropy change for different magnetic field change of Gd_4Co_3 alloy. Reprinted from the permission 18

FIG. 1.18. (a) Dependence of magnetization at room temperature for GdCo alloy and (b) GMR ratio of the spin-valves Fe(2 nm)/Cu(3 nm)/GdCo(3.2 nm) on the Co content of GdCo alloys. Measurements were performed at room temperature. (c) Dependence of GMR ratio at room temperature on the GdCo layer thickness for various compositions of GdCo. The lines serve as a guide to the eye. Reprinted with the permission 19

FIG. 1.19. (a) Saturation Hall resistivity as a function of the temperature. (b), (c) and (d) is the observed hysteresis loop. B_E is the external magnetic field. Reprinted with the permission 20

FIG. 1.20. (a) Temperature dependence of the saturation magnetization for GdCo alloys. The solid and dashed lines were calculated from the mean-field theory. (b) Compositional variation of the

saturation magnetization for GdFe and GdCo alloys at $T = 4.2$ K. (c) The temperature dependence of the coercivity for films of GdCo with compositions 33.7 % and 36.4 % of Gd. Reprinted with the permission 21

FIG. 1.21. Temperature dependence of the absolute value of the total magnetization per spin, for several values of D' and $J'_2 = 1.0$. Reprinted with the permission 22

FIG. 1.22. (a) Resistance–area product of the tunnel contact at the reverse bias of +0.2 V versus the thickness of the Al_2O_3 tunnel barrier. The red (orange) data is for the Si/ Al_2O_3 /Co ($\text{Ni}_{80}\text{Fe}_{20}$) (15nm) contacts; the blue data is for the Si/ Al_2O_3 /Gd (15 nm) contacts. (b) Resistance–area product of the Si/ Al_2O_3 (0.5 nm)/Gd/ $\text{Ni}_{80}\text{Fe}_{20}$ (10 nm) contacts at a reverse bias of +0.2 V versus the thickness of the Gd interlayer. The solid lines are a guide to the eyes. The inset shows the Schottky barrier height (Φ_B) of the contact versus the thickness of the Gd interlayer. The error bars denote the accuracy of the determination of the Gd thickness. Reprinted with the permission 23

Chapter 2

FIG. 2.1. Schematic representation of thermal evaporation with substrate heating. 28

FIG. 2.2. Schematic representation of electron beam evaporation with substrate heating. 29

FIG. 2.3. (a) Flow-chart of the integrated lithography root of NW and NC preparation. SEM image of the Gd (b) NW and (c) NC is prepared by this process. 30

FIG. 2.4. SEM image of the Ag pad on quartz substrate prepared by direct evaporation through Si hard mask. 31

FIG. 2.5. Schematic diagram of electron beam lithography process. 31

FIG. 2.6. Schematic diagram of (a) electron beam lithography metal deposition and (b) Ion beam deposited Pt deposition on a substrate with abrupt height differences on the surface. (c) SEM image of FIB deposited Pt voltage leads which are connected on Gd nanoconstriction sample. 32

FIG. 2.7. Schematic diagram of an arc furnace. 33

FIG. 2.8. (a) SEM image of the top view of an AAO. (b) Schematic diagram of metal coating on a template. (c) Schematic diagram of nanowire preparation by three electrode system electrodeposition method. 34

FIG. 2.9. (a) Cyclic Voltammetry curve (b) DC current vs. time curve and (c) Pulse current vs. time curve of GdCo alloy nanowire preparation. (d) SEM image of $\text{Gd}_{0.4}\text{Co}_{0.6}$ 100 nm diameter nanowires hanging from the Ag later. 35

FIG. 2.10. (a) Schematic representation of XRD system. (b) Normalized XRD (I/I_{max}) of bulk Gd and GdCo alloy. I_{max} is the maximum intensity. 36

FIG. 2.11. (a) Schematic representation of AFM. (b) AFM image of the surface of Gd film. (c) Gd film thickness determination by AFM. 36

FIG. 2.12. (a) Schematic diagram of the mechanism of SEM. (b) Schematic diagram of SE and X-ray generation by PE from an atom. (c) EDX spectrum of GdCo alloy nanowire. (d) Cross sectional SEM image to find out the thickness of Gd film. (e) SEM image GdCo nanowire. 37

FIG. 2.13. (a) Schematic diagram of the mechanism of TEM. (b) TEM image of GdCo nanowire. (c) Selected Area Diffraction (SAD) of GdCo nanowire. 38

FIG. 2.14. (a) Schematic diagram of the VSM. (b) $M - H$ loop of Gd samples at 80 K. The magnetization is normalized by M_S (M at 1.6 T). The samples are bulk ingot (Bulk) and two films of grain size 105 nm (Film-A), 35 nm (Film-B). 39

FIG. 2.15. FC and ZFC curve of Gd samples at a field 0.01 T. The samples are bulk ingot (Bulk) and two films of grain size 105 nm (Film-A), 35 nm (Film-B). 40

FIG. 2.16. Schematic diagram of low temperature AC resistance measurement technique. LIA = Lock-in amplifier, PA = Transformer Preamplifier. 41

FIG. 2.17. (a) Flux meter and air core solenoidal magnet. (b) V_{ind} vs. t plot for a current 0.4 A. (c) I dependent B curve. 42

FIG. 2.18. (a) Setup for measuring the low field MR. (b) Screenshot of the MR measurement program in LabVIEW during the measurement of the MR of Gd bulk sample at 235 K. 43

FIG. 2.19. (a) Setup for measuring the high field MR by a superconducting magnet. (b) Field dependent MR of bulk Gd sample. 44

Chapter 3

FIG. 3.1. Cross sectional SEM images of the films. 49

FIG. 3.2. (a) SEM image of crystallites of the Bulk sample. (b) AFM images of the films. The scale of AFM images is 1.5 μm . (c) Particle size distributions of Film-A and Film-B. In Film-A, the length and width of a crystallographic grain are denoted by (d_L) and (d_w) , where $d(+)$ and $d(-)$ indicate the limits of distribution as obtained from histogram. 50

FIG. 3.3. (a) XRD data of three different samples. fcc phase is indicated by arrows. (b) Grain size (d) dependent fcc phase volume% of the samples. 50

FIG. 3.4. Williamson Hall plot of the Film samples. 51

FIG. 3.5. Temperature dependence of the normalized derivative $\frac{1}{\rho_0} \frac{d\rho}{dT}$ in the vicinity of T_C for the three samples studied. 52

FIG. 3.6. The magnetization data of the three samples. (a) The left panel shows the $M - H$ data at different temperatures. (b) The right panel shows the $M - T$ data taken at a field of 0.01 T. Zero Field Cooled (ZFC) and Field Cooled (FC) data are shown, Due to uncertainty in film mass the magnetization data for the films have been shown in emu only. 54

FIG. 3.7. The variation of the coercive field H_C as a function of T as obtained from the $M - H$ curves. (Note: The data for H_C are in log scale.) 55

FIG. 3.8. Comparison of the resistivity change $-\Delta\rho$ (as a function of T) of three samples Bulk, Film-A and Film-B. Results are shown for both $H \parallel j$ and $H \perp j$ conditions with magnetic field $\mu_0 H = 0.15$ T. Transition temperatures (T_{SR} and T^*) are marked by arrows. 56

FIG. 3.9. Comparison of the resistivity change $\Delta\rho$ (as a function of H) of three samples Bulk, Film-A and Film-B. Results are shown for four different temperatures. 57

FIG. 3.10. Contour plot of $\frac{d(\Delta\rho)}{d(\mu_0H)}$ as a function of μ_0H and T for all three samples (Bulk, Film-A and Film-B). Columns (a) and (b) show $\frac{d(\Delta\rho)}{d(\mu_0H)}$ for the conditions $H \parallel j$ and $H \perp j$ 59

FIG. 3.11. Observed T dependence of the field H_{max} (where the field derivative $\frac{d(\Delta\rho)}{d(\mu_0H)}$ shows a maximum). 60

Chapter 4

FIG. 4.1. (a) Image (top view) of the nanowire of width ~ 275 nm made by FIB (sample S-2). (b) Cross-sectional SEM image of the nanowire on the Quartz substrate. (c) SEM images of the top surface of the film showing grain structure (before the nanowire was fabricated). 63

FIG. 4.2. Circuit diagram of four probe AC resistance measurement technique of Gd nanowire. 64

FIG. 4.3. Resistivity ρ vs. T for the two samples with inset showing the derivative to cleanly identify the T_C , marked by line. 65

FIG. 4.4. Colour Plot of $\Delta\rho$ as a function of μ_0H and T 65

FIG. 4.5. $\Delta\rho$ as a function of T for $\mu_0H = 0.17$ T, plotted for both samples in same graph. $\Delta\rho_{S-1}$ and $\Delta\rho_{S-2}$ correspond to the resistivity change of S-1 and S-2. 66

FIG. 4.6. $\Delta\rho_a/\rho_0$ ($\Delta\rho_a = \rho - \rho_0$) as a function of T for $\mu_0H = 0.17$ T, plotted for both samples in same graph. ρ_0 is the value of ρ at $\mu_0H = 0$ T. 67

FIG. 4.7. MR% ($\Delta\rho/\rho_0\%$) as a function of μ_0H , plotted for both samples in same graph. Applied field is along the current direction ($H \parallel j$). The field H_S is indicated by arrow. $H_S(+)$ corresponds to the red curve, whereas $H_S(-)$ for the green. Note: Negative MR has been plotted to highlight the magnitude in log-scale. 68

FIG. 4.8. Plot of μ_0H_S as a function of temperature. 68

Chapter 5

FIG. 5.1. Field (H) dependent magnetization (M) at 20 K. Inset shows the T dependent coercive field (H_C) of all samples at low temperature. 73

FIG. 5.2. M vs. T curve (FC and ZFC) for the film and bulk samples. The applied field is 0.01 T. The line through the FC data are fits to the Eqn. 5.1 74

FIG. 5.3. D vs. T as obtained from the $M - T$ curve. 75

FIG. 5.4. ρ vs. T curve of all three samples. Inset shows the $\rho - \rho_0$ vs. T^2 plot. Transition temperatures are indicated by the arrows. 76

FIG. 5.5. $d\rho_M/dT$ vs. T curve of the film samples. Calculated value of $d\rho_M/dT$ is mentioned as ‘‘Cal’’. 77

FIG. 5.6. (a) Field (H) dependent MR% at 20 K for film samples. Data is fitted by Eqn. 5.6. (b) Temperature (T) dependent $-\text{MR}\%$ ($\mu_0H = 9$ T). To show the absolute value negative MR has been plotted. 78

FIG. 5.7. (a) Temperature dependence of the real part of AC-susceptibility (χ') for two films samples at three different frequencies (17 Hz, 170 Hz and 1202 Hz). Amplitude of AC-magnetic field ($\mu_0 H_{ac}$) and dc bias field ($\mu_0 H_{dc}$) is 0.4 mT and 0 T. (b) Same for the imaginary part of AC-susceptibility (χ''). (c) The T dependence of the normalized susceptibility (χ'/χ'_0), where $\chi'_0 = \chi'(T = 5 \text{ K})$, at frequency 17 Hz of three different samples for DC bias field 0 T, 0.01 T and 0.1 T. Arrows indicate the shifting of T_{BE} with DC field intensity. 79

Chapter 6

FIG. 6.1. A 0.3 μm constriction was made on a 5 $\mu\text{m} \times 30 \mu\text{m}$ microstrip of a 40 nm Gd film by Ga ion Focused Ion Beam milling. The constriction is shown by a red box. The schematic measurement scheme is shown that allows measurement of resistance using an AC modulation current and phase sensitive detection that is mixed with the stressing DC-current I_{dc} . The two current sources are protected by Inductor L and capacitor C 84

FIG. 6.2. (a) Magnetization (M) vs. Field ($\mu_0 H$) of the Gd film taken at 80 K. (b) Shows the susceptibility $\chi = M/H$ 0 beyond the technical saturation field of 0.2 T. 85

FIG. 6.3. (a) Change in the resistance ΔR of the NC as a function of the DC stressing current I_{dc} . The sharp fall in resistance of the NC takes place when the DW is driven out of the constriction and it does not form again at the constriction when the current is cycled back. (b) The resistance R vs. I_{dc} at different temperatures. The domain wall resistance R_W is marked by arrow. As $T \rightarrow T_C$, $R_W \rightarrow 0$ 86

FIG. 6.4. (a) DW resistance R_W and the critical current density J_C as a function of T . The T_C is marked by an arrow. (b) Anisotropic magnetoresistance AMR as measured as a function of T . (c) The anisotropy parameter α as calculated from AMR as a function of temperatures. 87

FIG. 6.5. The DW thickness δ as a function of T as measured from the experiment. The graph shows the temperature variation of the anisotropy energy E_A as obtained from the measured value of δ . The inset shows the E_A of Gd as a function of T as obtained from magnetocrystalline anisotropy for a polycrystalline sample (A) (using the relation $E_A = k_1/2 + 3k_2/8$ and obtaining the value of k_1 and k_2 from previous report) and that measured from switching fields (B) ($H_S = E_A/M_S$) seen previously along with E_A measured in the present study (C). 88

FIG. 6.6. The DW thickness δ as a function of T which is measured in this work for a NC of Gd (A). DW thickness δ of a single crystal Gd sample (B). Spin reorientation temperature T_{SR} is indicated by arrow. 89

Chapter 7

FIG. 7.1. (a) Cyclic voltammetry curve of GdCo NW deposition. (b) XRD of both the samples. (b) Pulse current vs. time for NW preparation. 93

FIG. 7.2. (a) SEM image for the surface of Bulk sample and TEM image of a single nanowire. Co and Gd elemental mapping of the samples using EDX. (b) XRD of both the samples. 93

FIG. 7.3. (a) Temperature (T) dependence of the normalized magnetization $m(=M/M_{80})$ for bulk and nanowire samples. The applied field is $\mu_0 H = 10 \text{ mT}$ and for NW it is applied parallel to the wire axis. T dependence of dm/dT for (b) Bulk and (c) NW. Two phase transition temperatures (T_{m1} , T_{m2}) and the spin reorientation temperatures ($T^*_{1(-)}$, $T^*_{1(+)}$, $T^*_{2(-)}$ and $T^*_{2(+)}$) are indicated by arrows. 94

FIG. 7.4. (a) Field (μ_0H) dependence of M for Bulk, NW_{\parallel} and NW_{\perp} . Field applied parallel and perpendicular to the nanowire axis are indicated by \parallel and \perp sign. (b) M vs. $1/\mu_0H$ plot for different temperatures. Solid lines are the linear fit of the data to find the value of saturation magnetization (M_S). 95

FIG. 7.5. T dependence of (a) saturation magnetization (M_S) and (b) coercive Field (μ_0H_C). 96

FIG. 7.6. (a) Schematic diagram of field direction and nanowire axis or c-axis. (b) Field (μ_0H) dependence of M of NW for different field angle φ (angle between H direction and c-axis) from 0° to 90° at 843 K (near T_{m1} of NW). (c) M vs. φ for field 1.5 T. (b) Temperature variation of the retativity (m_r) of NW for both \parallel and \perp conditions. 97

FIG. 7.7. Schematic diagram of magnetic field direction in (a) Bulk and (b) NW sample. In nanowire the field is applied in the \parallel condition or along the z-axis. L and R are the length and radius of the cylindrical nanowire. 98

FIG. 7.8. Temperature (T) dependence of E_A for bulk and nanowire. NW_{\parallel} and NW_{\perp} indicate the field direction along \parallel and \perp to the nanowire axis. 99

Appendix

FIG. A1.1. (a) Four probe connection on FIB deposited nanowire of length 20 μm . (b) Cross section of FIB deposited C-Pt on SiO_2 coated Si wafer substrate. Pt islands are distributed in a carbon matrix. 105

FIG. A1.2. (a) Resistivity vs. temperature of four NWs (b) Resistivity (ρ) vs. metallic concentration (C) for different temperatures. 106

FIG. A2.1. Arrott plot of Bulk, Film-A and Film-B. 109

FIG. A4.1. Schematic diagram of DW at the constriction. The coordinate at the centre of the constriction is (0,0). 111

List of Tables:

Table 3.1. Comparison of the d of film samples finding from different methods.	51
Table 3.2. Comparison of T_C of the samples studied with previous works.	53
Table 6.1: A_{ex} of different magnetic materials.	83
Table 6.2: Full data of the experiment.	86
Table 7.1: E_A and dE_A/dT of Bulk and NW at T_{cm}	100
Table A1.1: Volume concentration of conducting and non-conducting elements with FIB energy at 28 pA beam current ($\pm 0.1\%$) of four different NW samples.	106
Table A2.1: Results of the Arrott plot experiment.	109
Table A4.1: The value of k at different temperatures.	112

CHAPTER 1

Introduction

In recent years, investigation of magnetism in Gadolinium (Gd), in particular, polycrystalline, and nanostructured Gd has attracted renewed attention. This renewal of interest is due to a number of reasons that range from basic physics issues related to the magnetism in the 4f metal and also its application potentials. Also the alloys of Gd with transition metals are expected to have applications in field like Spintronics. Electric, magnetic and magneto-electric properties are greatly affected in nanostructures. In this chapter we give a brief review of the status of the relevant issues and the necessary background needed for development of the thesis. A short review on the newly emerging magnetic properties is discussed here. In this chapter we discuss the motivation of this thesis and discuss the importance of nanostructured Gd and its alloys. The outline of the thesis is stated at the end of this chapter.

1.1.Motivation:

Magnetism in Gd is fast re-emerging as an actively researched area [1-6]. The main motivation appears to be the fact that Gd is a new nanomagnetic system where the ferromagnetic (FM) state arises from Gd ions with well-localized spin only moment in contrast to the magnetism in more itinerant conventional 3d ferromagnetic materials like Fe, Ni and Co. Strongly localized magnetic moment of Gd ions without orbital contribution, rather low and temperature dependent magnetocrystalline anisotropy energy (E_A), makes Gd a special ferromagnetic metal. In recent years, there is renewal of interest in magnetism of Gd, particularly nanocrystalline Gd. This renewal of interest is due to a number of reasons that range from basic physics issues related to the magnetism in the 4f metal and also its application potentials.

The main binding thread of the thesis is the anisotropy energy (E_A) and its modification as Gd becomes nanostructured. We also show how a low field MR in Gd nanostructured films and nanowires and current induced domain wall motion in a nanoconstriction can lead to a quantitative evaluation of anisotropy energy (E_A). A very interesting manifestation of the E_A and its temperature derivative $\frac{dE_A}{dT}$ was found in nanowires of a Gd-Co alloy where the compensation temperature (T_{cm}) the Gd-Co alloy shifts by few hundreds of Kelvin in nanowires of the same composition due to softening of $\frac{dE_A}{dT}$, that occurs due to predominant contribution of nearly temperature independent shape and size anisotropy energy to E_A in contrast to the temperature dependent magnetocrystalline anisotropy that dominates the E_A in the bulk sample.

In this thesis work we also studied on the newly emerging magnetic properties like Bose Einstein Condensation (BEC) of quasi-particle magnon that occurs due to softening of spin wave stiffness constant in nanostructured Gd.

1.2.Unique properties of Gd:

Gd is a 4f rare-earth ferromagnetic metal and it has some unique properties that makes it distinct from other ferromagnets.

1.2.1. Electronic structure:

There are 64 electrons in a single atom of Gd. The electronic structure of Gd is $[\text{Xe}]4f^75d^16s^2$. According to the Hund's rule half filled orbital is more stable. The binding energy of 4f is nearly same as that of the 5d orbital. Due to this fact one electron goes to the 5d orbital and makes 4f as a more energetically stable half field orbital with seven electrons. This 4f orbital is responsible for the magnetic moment of a single Gd atom. For Gd, the spin and orbital angular momentum quantum number is $S = 7/2$ and $L = 0$ and the total quantum number $J = L + S = 7/2$ and Landé g-factor, $g = 1 + \frac{J(J+1)+S(S+1)-L(L+1)}{2J(J+1)} = 2$. Therefore, the 4f orbital is spherical (since $L = 0$) and it is shielded by the outer most shells 5d and 6s. This shielding stabilizes the magnetic moment. Due to the presence of seven unpaired electrons the magnetic moment of Gd is very large. It is a classical ferromagnet or a simple Heisenberg ferromagnet where the spin only moments are localized. The localized moments are indirectly coupled via the Ruderman-Kittel-Kasuya-Yosida (RKKY) interaction [7]. This is in sharp contrast to conventional 3d transition metals like Fe, Co, Ni where the ferromagnetism is due to itinerant character and is not due to a localized moment. Due to this sharp contrast Gd is so much distinct from the conventional 3d ferromagnets.

1.2.2. Room temperature T_C :

The ferromagnetic to paramagnetic transition temperature which is called the Curie temperature (T_C) of Gd is around room temperature or ~ 293.2 K [8]. This is a second order phase transition. It is well known that the magnetocaloric effect of a magnetic material is the largest at T_C . This occurs due to the balancing of two opposite forces at T_C . One is the ordering of moments due to the exchange interaction and another one is the disorder due to the lattice thermal vibration. Therefore at T_C for small application of magnetic field magnetization is increased sharply. Spins are ordered greatly and entropy change becomes maximum. Since Gd has a room temperature T_C , for thermo magnetic application it is an important candidate [9, 10].

1.2.3. Anisotropy energy (E_A):

The temperature dependent anisotropy energy (E_A) of Gd is unique. The magnetocrystalline anisotropy energy of Gd is uniaxial and it is represented by

$$E_A = k_1 \sin^2 \theta + k_2 \sin^4 \theta \quad (1.1)$$

, where k_1 and k_2 are the anisotropy constants.

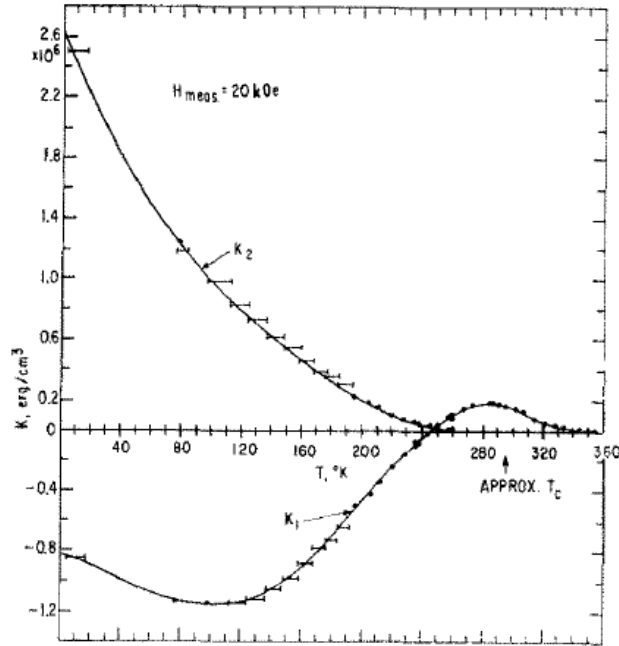


FIG. 1.1. Magnetocrystalline anisotropy constant of Gd. Reprinted with permission from [11].

At 1963, Graham et. al. [11] first experimentally found out the value of magnetocrystalline anisotropy constants (k_1 and k_2) of a single crystal Gd disk sample. The measurements had been done by the torque magnetometer with a field of 20 kOe. At T_C the first anisotropy constant k_1 has a finite value where k_2 becomes zero above 235 K. Below this temperature k_2 rises sharply with a positive value and k_1 changes its sign from positive to negative. The temperature 235 K is represented as spin reorientation temperature (T_{SR}) where k_1 and k_2 both simultaneously becomes zero (i.e. $E_A \sim 0$). This unique feature is only observed in Gd. Since the orbital magnetic moment $L = 0$ for Gd, the value of E_A of Gd is smaller than the other rare earth materials Tb, Ho etc. (though it is larger than the transition metals Fe, Co, Ni).

1.2.4. Spin structure:

Gd has a hexagonal closed-packed (*hcp*) crystal structure with the lattice constants $a = b = 3.63 \text{ \AA}$ and $c = 5.76 \text{ \AA}$. For a hexagonal system with uniaxial anisotropy depending on the values of anisotropy constants (k_1 and k_2) four different cases are observed.

- (a) When $k_1 = k_2 = 0$, the ferromagnet is isotropic.
- (b) When $k_1 > 0$ and $k_2 \geq 0$, the c -axis (along the c lattice constant) is an easy axis.
- (c) When $k_1 < 0$ and $k_2 \leq 0$, the basal plane is an easy plane.
- (d) When k_1 and k_2 have different signs, the ferromagnet has an easy cone.

The easy angle θ_0 between c -axis and saturation magnetization (M_S) is defined from the energy minima conditions, $\left(\frac{\partial E_A}{\partial \theta}\right)_{\theta_0} = 0$ and $\left(\frac{\partial^2 E_A}{\partial \theta^2}\right)_{\theta_0} > 0$.

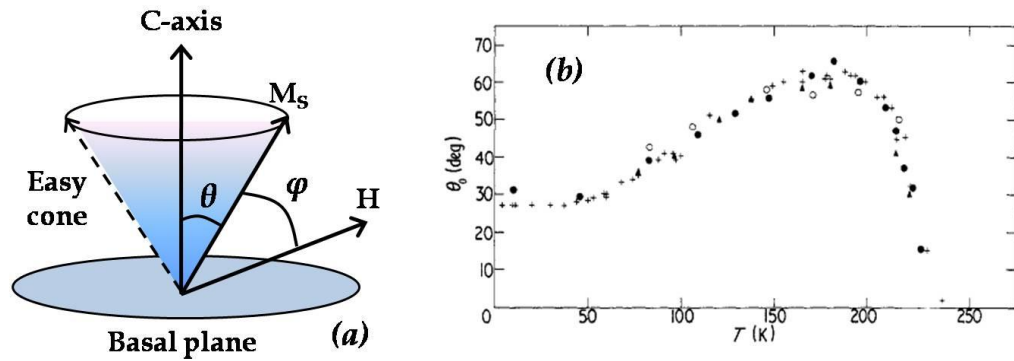


FIG. 1.2. (a) Schematic diagram of magnetization direction. θ is the angle between c -axis and saturation magnetization M_S . The applied field H makes an angle φ with M_S . Easy cone and basal plane is marked in the figure. (b) Plot of the easy angle (θ_0) between c -axis and magnetization of Gd as a function of temperature. Reprinted with permission from [12].

When k_1 and k_2 are both positive, the energy E_A is minimum for $\theta = 0^\circ$ and c -axis is an axis of easy magnetization. FIG. 1 clearly shows that this condition for single crystal Gd only occurs at $T > T_{SR}$ and in this temperature region $\theta_0 = 0^\circ$ (FIG. 2). If k_1 and k_2 are both negative, the minimum value of E_A occurs at $\theta = 90^\circ$. This does not occur in Gd and any basal plane magnetization is not observed here. If k_1 is negative and k_2 is positive, the limit of easy plane behaviour is $k_2 < -k_1/2$. For the value of k_2 from $-k_1/2$ to ∞ the easy direction of M_S with c -axis is an angle θ which lies between 0° to 90° . The value of easy angle θ_0 which is the half angle of the easy cone is represented as,

$$\theta_0 = \sin^{-1} \left(\sqrt{\frac{|k_1|}{2k_2}} \right) \quad (1.2)$$

For Gd below T_{SR} the value of θ_0 sharply rises and it becomes maximum ($\sim 60^\circ$) at $T^* \sim 190 \text{ K}$. Due to the further decrease of temperature θ_0 also decreases and below 50 K the value becomes stable at 30° . Therefore in Gd for $T_{SR} < T < T_C$ the easy direction of magnetization is along c -axis and for $T < T_{SR}$ the magnetization lies along an easy cone of angle θ_0 with c -axis. Except T_C there exist another two transition temperatures T_{SR} (where $E_A \sim 0$) and T^* (where the canted angle θ_0 becomes maximum).

1.2.5. Spin reorientation transition temperature T_{SR} :

In Gd at $T_{SR} \sim 235 \text{ K}$ spins are isotropic in nature and it is called the secondary phase transition. Specific heat (C_p) and electric resistance are affected at this temperature.

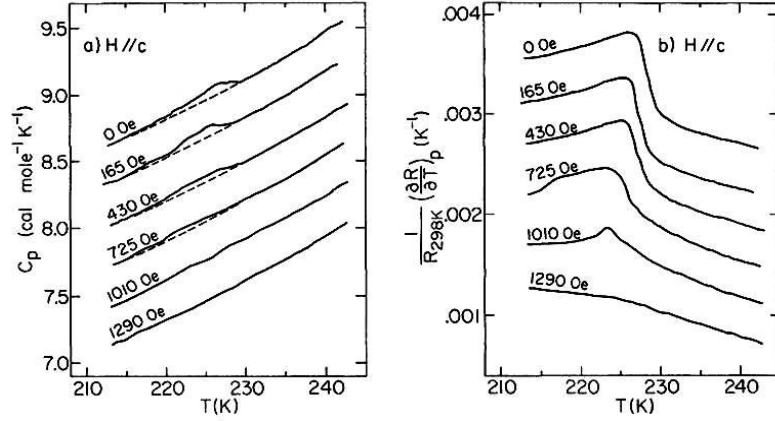


FIG. 1.3. (a) Specific heat and (b) temperature derivative of basal plane resistance of Gd in magnetic field parallel to c -axis. Reprinted with permission from [13].

The work of Salamon et. al. [13] shows that for zero field, C_p has a small hump at T_{SR} . The change $\Delta C_p = 0.09 \pm 0.01$ cal/mole K decreases with the increase of magnetic field and disappears between 0.7 and 1.0 kOe. Temperature derivative of resistance shows more prominent result of this phenomenon. In zero field data a sharp peak was observed at T_{SR} and it was completely suppressed for a magnetic field around 1.0 to 1.3 kOe. As the field increases the peak position was shifted towards the lower temperature. External magnetic field plays an important role against the anisotropy energy and rotates the spins in the field direction. By molecular field model the step change in specific heat can be calculated as $\Delta C_p = -T_{SR} \left(\frac{\partial^2 E_A}{\partial T^2} \right)_{T_{SR}} = 0.06 \pm 0.01$ cal/mole K where E_A is the anisotropy energy and it has a good agreement with experimental results. The critical field (H_{cr}) for which the transition was completely suppressed can be defined as $H_{cr} \propto \frac{8k_1^{max}}{M(0)}$. Where $k_1^{max} = 2.5 \pm 0.5 \times 10^5$ erg/cm³ is the maximum (positive) value of k_1 and $M(0) = 7.55 \mu_B/\text{atom}$.

1.2.6. Domain wall thickness δ :

Domain wall (DW) energy (γ_w) and DW thickness (δ) has a strong dependence on E_A . The unique temperature dependency of E_A clearly reflects on γ_w and δ . The value of γ_w which is associated with the rotation of magnetization from one easy direction to another can be expressed as [14]

$$\gamma_w = A_{ex} \sin \varphi \int_{\theta_1}^{\theta_2} \frac{d\theta}{\sqrt{E_A}} \quad (1.3)$$

, where φ is the angle between magnetization and the normal of the DW. Exchange stiffness constant is $A_{ex} = \frac{JS^2}{a}$ where J is the coefficient of exchange energy, S is the spin quantum number and a is the lattice constant. If the rate of change of magnetization direction is constant with the same rate of change at the middle of the DW, the minimum value of δ can be evaluated from the relation

$$\delta = (\theta_2 - \theta_1) \sin \varphi \sqrt{\frac{2A_{ex}}{(\theta_2 - \theta_1)E_A}} \quad (1.4)$$

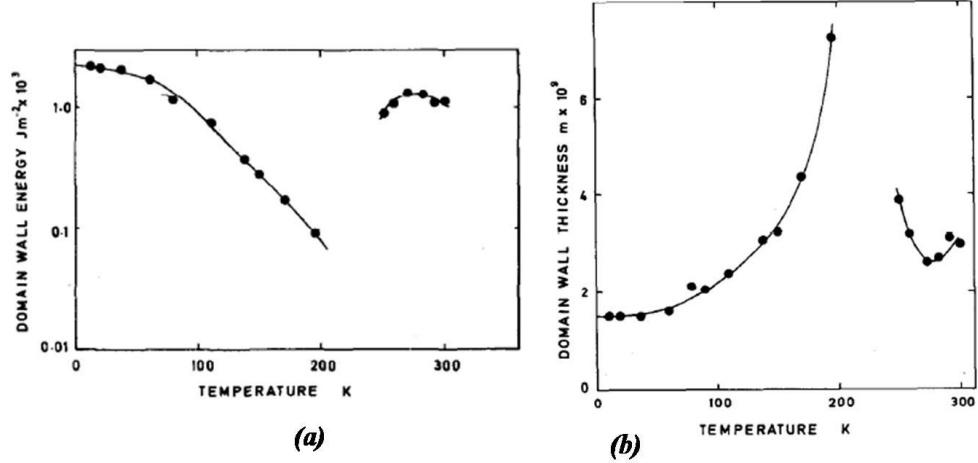


FIG. 1.4. Temperature dependence of (a) DW energy γ_w and (b) DW thickness δ of single crystalline Gd. Reprinted with permission from [14].

From low temperature γ_w decreases with the increase of temperature and at T_{SR} it becomes minima. After that for increasing temperature it increases again and shows a small hump at the Ferro-para phase transition temperature $T_C \sim 293.2$ K (see FIG. 1.4(a)). Since $\delta \sim 1/(E_A)^{1/2}$, at T_{SR} (where $E_A \sim 0$) δ diverges and the domain structure disappears (see FIG.1.4(b)). From our best knowledge Gd is the only material which shows this behaviour where in the ferromagnetic region at a particular temperature magnetic spins are isotropic in nature.

1.3. Magnetoresistance (MR) study of Gd:

Gd is a heavy rare earth ferromagnet with localized spin structure. Atomic moment of Gd is very high and also its temperature dependency of E_A is unique. Due to these properties from the middle of the last century people were studying the magnetoresistance (MR) of Gd and were trying to implement it in giant magnetoresistance (GMR) devices or spin valves (SV)[15]. The MR of the 3d transition metals and alloys has been well studied. In comparison, except few classic reports [16, 17] investigation of MR of 4f-ferromagnet Gd has not been done very well. Also these investigations have been done at a time when the interesting features of Gd like spin reorientation transition and temperature dependent spin structure have not been understood very well.

The MR of Gd single crystal and polycrystalline sample was first experimentally observed by Hirakoa et. al. [18]. The magnetic anisotropy constants k_1 to k_4 can be related with the differences of MR ($\Delta\rho/\rho$) at different directions. For the a -axis sample,

$$\begin{aligned} k_1 &= (\Delta\rho/\rho)_{H\parallel a} - (\Delta\rho/\rho)_{H\parallel c} \\ k_2 &= (\Delta\rho/\rho)_{H\parallel b} - (\Delta\rho/\rho)_{H\parallel c} \end{aligned}$$

for the c -axis sample,

$$k_2 = (\Delta\rho/\rho)_{H\parallel b} - (\Delta\rho/\rho)_{H\parallel c} \quad (1.5)$$

Similarly k_4 can be found using the 45° to c -axis sample. γ denotes both perpendicular to b -axis and current direction.

$$-\frac{1}{2}k_1 + \frac{1}{2}k_2 + k_4 = (\Delta\rho/\rho)_{H\parallel b} - (\Delta\rho/\rho)_{H\parallel \gamma} \quad (1.6)$$

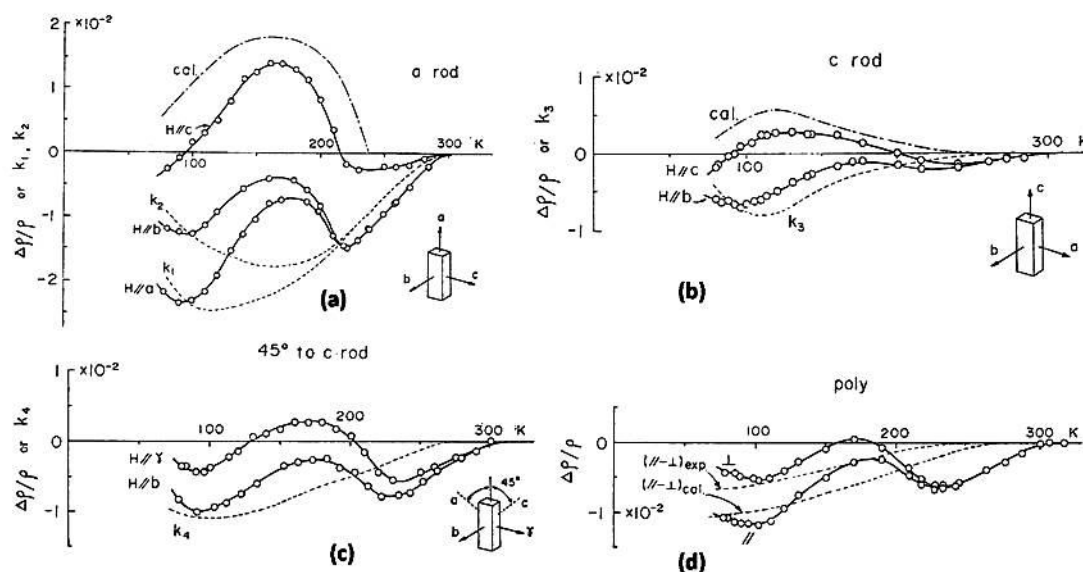


FIG. 1.5. Magnetoresistance effects of Gd single crystal as a function of temperature (a) for the a-axis sample. (b) c-axis sample and (c) for 45° to c-axis sample. Dotted curves are k_1 , k_2 , k_3 and k_4 . Broken curve is the calculated ones for $H//c$. (d) Magnetoresistance of Gd polycrystalline sample. Dotted curves are the experimental and the calculated ones for the difference between the longitudinal and the transverse effect. Reprinted with permission from [18].

The anisotropy constants k_1 to k_4 which were calculated in this method becomes negative throughout the temperature region. There is a single minimum observed at 110 K, 160 K for k_1 and k_2 . The MR of all the samples (single crystal and polycrystal) with all the conditions shows a sharp maximum with negative value around 240 K.

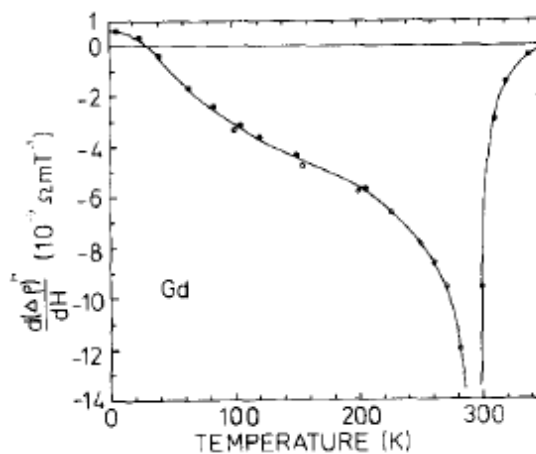


FIG. 1.6. The temperature dependence of the magnetoresistance coefficient of Gd. Reprinted with permission from [17].

The coefficient of MR or the forced magnetoresistance $d(\Delta\rho)/dH$ within 120–260 K follows the temperature dependence as, $d(\Delta\rho)/dH \propto [1 - (T/T_C)]^{-1/2}$ [17]. As the temperature approaches T_C the spin fluctuation becomes very large and consideration of their interactions is necessary. Because of that above 260 K the forced MR is deviated from the above relation.

Therefore through the anisotropy energy Gd has a strong temperature dependency. All these work had been done on bulk sample. In nanodimension anisotropy energy changes and has a different temperature dependency from bulk and therefore MR must be different in nanostructured sample than its bulk counterpart.

1.4. Bose Einstein Condensation (BEC) of quasi-particle magnon:

The occupation of a single quantum state (ground state) by a large number of bosons at low temperature is called Bose Einstein Condensation (BEC). The particles which follow Bose statistics are called boson. Dilute atom gas, photon, phonon, magnon etc. are bosons with integral spin.

1.4.1. Condition for BEC of quasi-particles:

Quasi-particle is a physical concept which describes the elementary excitons in solid. The quasi-particles or excitons have integral spins and therefore they are boson. According to Blatt [19] there are mainly two conditions for BEC of quasi-particles.

- (a) The chemical potential μ of these particles must be a valid thermodynamic variable.
- (b) The number density (n) of a quasi particle becomes larger than a critical value n_{cr} .

The chemical potential is the slope of the free energy of the system with respect to the particle number at its present state. The number of particle in a quasi-particle system is not fixed but at thermal equilibrium the free energy is minimum and μ becomes zero. BEC is a quantum phenomenon and it occurs when the de Broglie wavelength λ_d is comparable with the inter-particle distance. Using this condition the critical value of particle density is found as,

$$n_{cr}^{-1/3} \sim \lambda_d \simeq \hbar(m_{eff} k_B T_{cr})^{-1/2} \quad (1.7)$$

, where m_{eff} is the effective mass and T_{cr} is the critical temperature. The condition for BEC of quasi-particle occurs when the life time of the quasi-particle becomes much larger than their scattering time.

1.4.2. Magnon BEC in different systems:

In a lattice system the elementary excitations of spins are called magnon. It is a quasi-particle and it follows BE statistics. Few time scales which determine the condition of BEC are mentioned below [20]:

- (a) magnon-magnon ($2m$) interaction time (τ_{2m}) which restore equilibrium and conserve magnon number.
- (b) multi-magnon (mm) interaction time (τ_{mm}) which do not conserve magnon number.
- (c) Long wave length magnon dispersion time (τ_C) to cross a grain of the system.
- (d) The time (τ_B) over which BE condensation forms.
- (e) The time (τ_ϕ) over which phase coherence occurs.

If the condition $\tau_B, \tau_\phi < \tau_C < \tau_{2m} < \tau_{mm}$ is satisfied, BEC occurs for a magnon of life time greater than τ_{mm} .

From the end of the last century BEC of magnon have been reported in different systems. The experimental evidence of the BEC of magnon was first observed in spin-dimer compound TiCuCl_3 [21]. Later there have been done few more works on this

system [22, 23]. TlCuCl_3 is composed of a chemical double chain Cu_2Cl_6 and in the absence of a magnetic field the compound has an excitation gap $\Delta/k_B \approx 7.5$ K above the singlet ground state. The origin of the gap may be caused by the antiferromagnetic dimer coupling in the double chain. The gap collapses for the field $H_g = \Delta/(g\mu_B)$. There is a phase transition occur for $H = H_C > H_g$ and $[H_C(T) - H_g] \propto T^{3/2}$. Similar result was observed in the spin-dimer compound KCuCl_3 [24] and NH_4CuCl_3 [25].

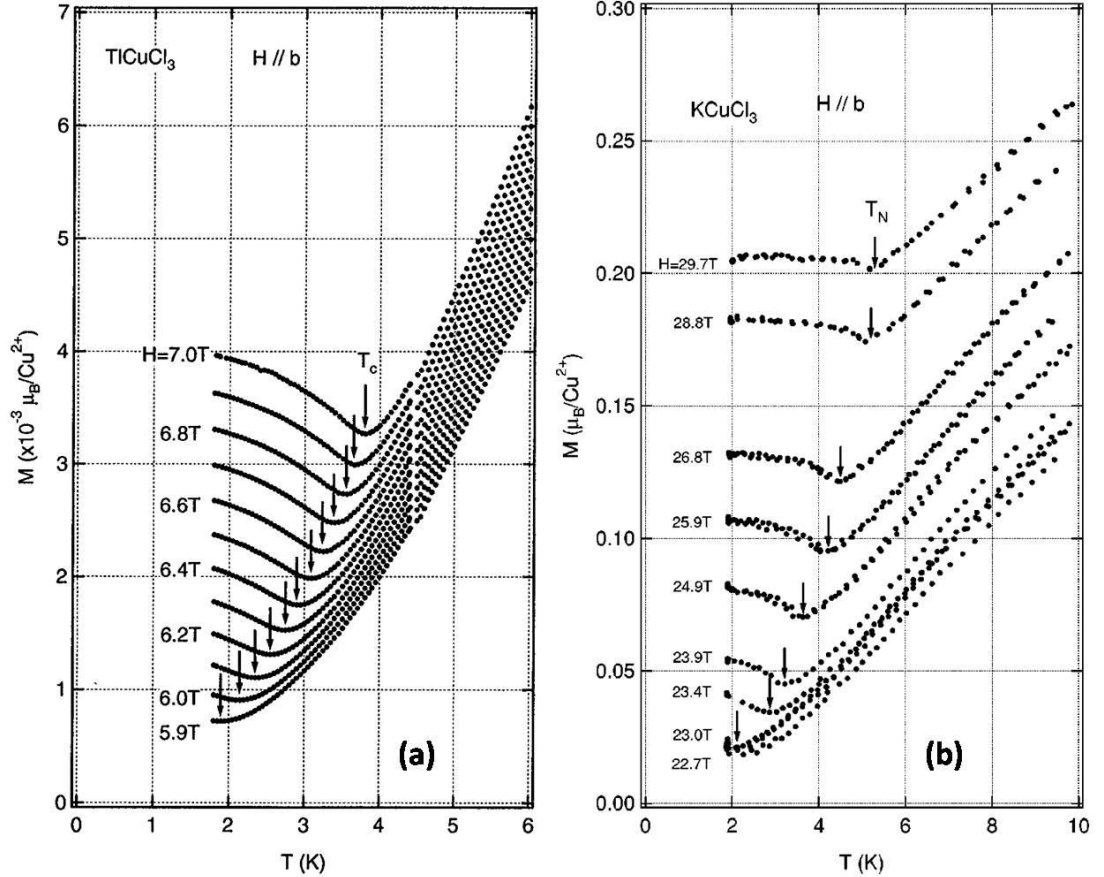


FIG. 1.7. The low-temperature magnetizations of (a) TlCuCl_3 and (b) KCuCl_3 measured at various external fields for $H \parallel b$. (a) and (b) are reprinted with permission from [22] and [24].

BEC was also observed in few more spin-dimer compounds $\text{Pb}_2\text{V}_3\text{O}_9$, $\text{Sr}_3\text{Cr}_2\text{O}_8$, $\text{Ba}_3\text{Cr}_2\text{O}_8$ and $\text{BaCuSi}_2\text{O}_6$ [26-30]. It was observed in quantum spin-1/2 antiferromagnet Cs_2CuCl_4 [31] and organic spin gap compound $\text{NiCl}_2\cdot 4\text{SC}(\text{NH}_2)_2$ [32] also. FIG. 1.8 shows the field dependence of the magnetic torque and magnetization of $\text{Ba}_3\text{Cr}_2\text{O}_8$. Only within the range of two critical fields $H_{C1} = 12.7$ T and $H_{C2} = 23.37$ T, torque/field and magnetization has a linear field dependence. At these two critical fields the second derivative of torque/field shows extrema (inset of FIG 1.8(a)). The lower transition can be described by the BEC triplon theory. Also the magnetic hysteresis is only observed at the upper transition H_{C2} . Therefore the lower transition is second order type where the upper transition is more likely the first order type. At H_{C2} lattice coupling may play a crucial role. From the phase diagram the maximum transition temperature to the magnetically ordered state was found to correspond to ~ 2.7 K at $H \sim 18$ T (FIG 1.8(c)).

The phase diagram was determined through a combination of magnetic torque, magnetic force, MCE, and heat-capacity measurements.

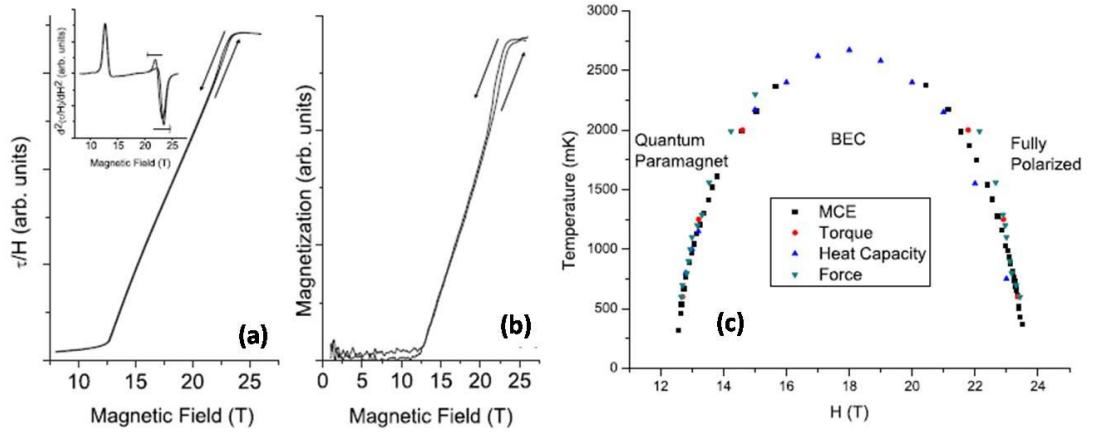


FIG. 1.8. (a) Magnetic torque measurement of $\text{Ba}_3\text{Cr}_2\text{O}_8$ at 600 mK. The second derivative of torque/field, shown in the inset, shows two prominent extrema, indicative of the two transitions. (b) Force magnetometry measurement at 600 mK. These data are qualitatively similar to the torque measurement. (c) The phase diagram of $\text{Ba}_3\text{Cr}_2\text{O}_8$ for the $H \parallel \hat{c}$ orientation. Figures are reprinted with the permission from [30].

Also BEC of magnons has been observed at room temperature [33] in a cubic ferromagnetic insulator Yttrium-iron-garnet (YIG: $\text{Y}_3\text{Fe}_2(\text{FeO}_4)_3$) film by application of microwave pumping that creates a large enhancement of magnon density which in turn leads to BEC.

1.4.3. Magnon BEC in nanostructures:

The long wave length magnon dispersion time τ_C could be related with the system size as [34], $\tau_C \propto l^\beta$, where $l = L/a$ is the system size in units of the lattice constant a . As a crude sense τ_C could be taken as the time scale for a magnon near the gap to cross the system. Therefore $\tau_C \sim L/v_m \sim \hbar l^2/\pi J$ in agreement with the $\beta = 2$ prediction. For a system of grain size 10 nm ($l \sim 10^2$), 1 mm ($l \sim 10^7$) and 30 cm ($l \sim 10^9$) τ_C is 10^{-10} s, 1 s and 5.5 h. If the system size increases, it is very difficult to maintain the inequality condition $\tau_C < \tau_{mm}$. Therefore in low dimension (nanostructure system) the probability of occurrence of magnon BEC enhances.

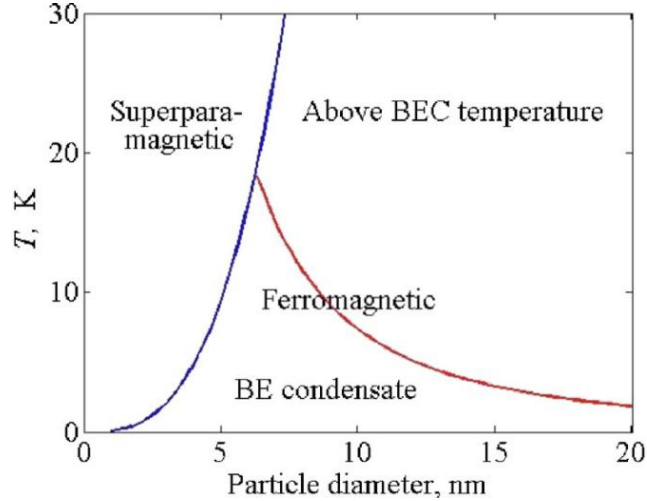


FIG. 1.9. Division of the temperature vs particle length plane into three regions. Reprinted with the permission from [35].

The gap temperature T_{gap} corresponding to the gap energy, $E_{gap} = Ja^2(k_l^2 - k_0^2)$, is the lower bound for the BEC temperature. The maximum value of magnon wave length satisfy the condition $\lambda = 2d$. Where d is the particle diameter and $k_0 = \pi/d$, $k_l = 2\pi/d$. Therefore $T_{gap} = 3J\pi^2 a^2 / k_B d^2$.

The blocking temperature T_{BL} which is related with the superparamagnetism must be greater than T_{BEC} . The energy barrier for magnetic reversal is $CV/2$, where C is the specific heat and V is the volume. $C = (D_b - D_a)M^2$, where M is the magnetization and D 's are the shape demagnetizing factor. Again for a crystalline anisotropy $C = 2k_l$, where k_l is the anisotropy constant. The relaxation time for uniaxial anisotropy is $\tau = 10^{-9} e^{CV/k_B T}$. For a $\tau = 100$ s, T_{BL} can be expressed as $T_{BL} = CV/50k_B$.

For Fe $J = 2.16 \times 10^{-21}$ J and $a = 0.4$ nm. Again for a spherical particle $C = 10^5$ J/m³ and $V = \pi d^3/6$. FIG. 1.9 shows that there are three distinct phases: the ferromagnetic phase ($T > T_{BEC}$), the superparamagnetic phase ($T > T_{BL}$) and BEC phase ($T < T_{BEC}, T_{BL}$). This result clearly shows that the BEC is favourable in nanostructured system. This type of temperature driven BEC have been reported in Co/Pt multilayer nanopillars [36] and more recently in Gd nanocrystal [20, 37-38].

1.4.4. Magnon BEC of Gd nanocrystals:

The detailed study on the BEC of magnon in nanocrystalline Gd of grain size 12 nm and 18 nm has been reported [37]. In the presence of magnetic field H the momentum distribution of magnon in uncondensed phase is

$$n = \frac{1}{(2\pi)^3} \int_0^\infty \frac{d^3 k}{e^{\beta(\varepsilon_k + \Delta - \mu)} - 1} \quad (1.8)$$

, where $\varepsilon_k \equiv \hbar^2 k^2 / 2m^*$ with the effective mass $m^* = \hbar^2 / 2D$ and D is the spin wave stiffness constant. $\Delta = \Delta_0 + g\mu_B H$, where Δ_0 is the gap in the spin wave spectrum by magnetocrystalline anisotropy energy. μ is the chemical potential. The magnon contribution in magnetization is given by

$$M(T, H) = M(0, H) - g\mu_B n \quad (1.9)$$

The specific heat per unit volume C_{mag} can also be expressed as,

$$C_{mag}(T, H) = \frac{3k_B}{2} \left(\frac{k_B T}{4\pi D} \right)^{3/2} \left\{ \left[\frac{5}{2} + \frac{3D_2 T^2}{1 - D_2 T^2} \right] \times \sum_{l=1}^{\infty} \frac{(Z_{eff})^l}{l^{5/2}} - \ln Z_{eff} \sum_{l=1}^{\infty} \frac{(Z_{eff})^l}{l^{3/2}} \right\} \quad (1.10)$$

, where $Z_{eff} = e^{-\beta(\Delta - \mu)}$ and $D = D_0 [1 - D_2 T^2 - D_{5/2} T^{5/2}]$.

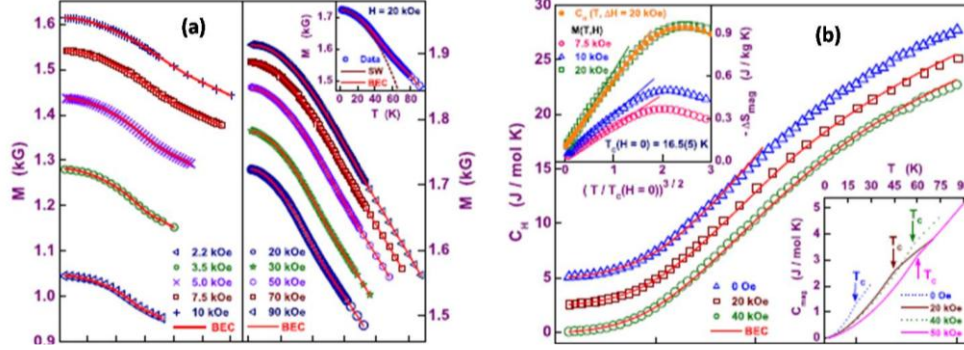


FIG. 1.10. (a) Comparison between the observed (symbols) and theoretical [continuous curves, yielded by equation (1.9)] temperature variations of magnetization at fixed fields in the range 2.2 – 90 kOe in nanocrystalline Gd with an average grain size of 12 nm. The inset illustrates that, unlike the BEC formalism, the conventional spin-wave theory fails to describe $M(T)$ over an extended temperature range. (b) The total specific heat $C_H(T)$ at a few representative fields for $d = 12$ nm. Note that the $C_{H=20 \text{ kOe}}(T)$ and $C_{H=0}(T)$ data are shifted up by 2.5 and 5.0 J/molK, respectively, with respect to that taken at $H = 40$ kOe. The continuous theoretical curves are obtained by adding the (Sommerfeld) electronic, (Debye) lattice and (BEC) magnon C_{mag} contributions to $C_H(T)$. The bottom inset shows $C_{mag}(T)$, the slope change at T_C , predicted by the BEC theory, and the increase in, and progressive smearing of, T_C with H . The top inset displays the magnetic entropy change $-\Delta S_{mag}$ for a few representative ΔH values (open symbols), obtained from $M_H(T)$, plotted against $[T/T_{BE}(H=0)]^{3/2}$ for $d = 12$ nm. The straight lines serve to highlight the characteristic BEC $T^{3/2}$ variation of entropy for $T \ll T_C$. $-\Delta S_{mag}$ at $\Delta H = 20$ kOe (solid circles), calculated from $C_H(T)$, agrees quite well with that calculated from $M_H(T)$ (open squares). Reprinted from the permission of [37].

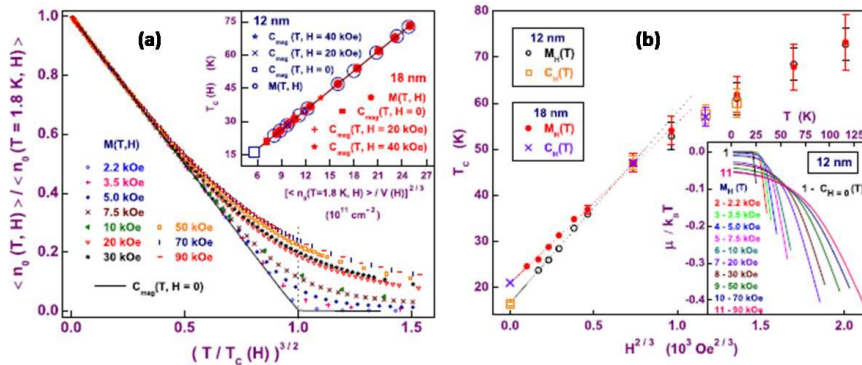


FIG. 1.11. Scaling of the magnon BE condensate fraction with $(T/T_{BE})^{3/2}$ at different fields for $d = 12$ nm. The inset highlights the scaling of $T_C(H)$ with $[(n_0(T = 1.8\text{K}, H))/V(H)]^{2/3}$. (b) The BEC transition temperature T_C obtained from $M_H(T)$ and $C_{mag}(T, H)$ plotted against $H^{2/3}$ for $d = 12$ and 18 nm. The bottom inset depicts the temperature variations of the normalized chemical potential $\mu/k_B T$ at various fixed field values. Reprinted from the permission of [37].

From the self-consistent fitting of Eqn. 1.9 and 1.10 to magnetization and specific heat n , D and μ was determined. The observations showed that (a) the critical temperature $T_C \propto H^{2/3}$, (b) at $H = 0$, up to $T = T_C$ the condensate fraction scales with $[T/T_C]^{3/2}$ and becomes zero for $T \geq T_{BE}$, (c) $T_C(H) \propto (\text{field-dependent condensate density})^{2/3}$, (d) for $T \leq T_{BE}$, $\mu \rightarrow 0$ as $H \rightarrow 0$ and sharply reaches to a large negative value for $T > T_{BE}$ and (e) at low temperature the magnon entropy follows the $T^{3/2}$ power law.

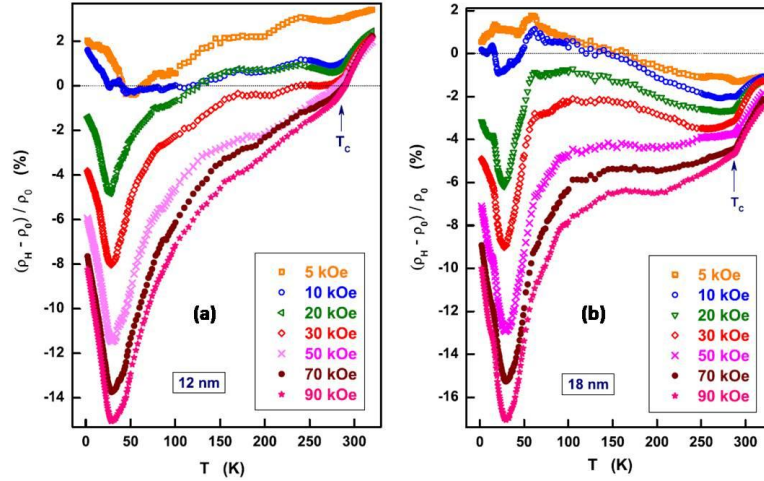


FIG. 1.12. Transverse magnetoresistance, $\Delta\rho_{\perp}(T)$, calculated from the ‘in-field’ and ‘zero-field’ resistivity at various fixed fields, as a function of temperature for the nanocrystalline Gd sample with average grain size (a) $d = 12$ nm and (b) $d = 18$ nm. Reprinted from the permission of [20].

The temperature dependence transverse magnetoresistance $MR = [\rho(H_{\perp}) - \rho_0]/\rho_0$ shows a sharp minima at T_{BE} and the amplitude of that minimum value increases with the increment of field H . Due to an anomalous softening of spin-wave modes magnetic field of increasing strength progressively destroys the BE condensate phase coherence and suppresses the magnons. Therefore electron-magnon scattering contribution also decreases sharply.

In the nanostructured materials, the observations of magnon BEC have been made mainly through magnetic measurements like magnetization (M) but in this nanostructure sample similar behaviour may also be observed from the superparamagnetism. In this thesis we strengthen the proposal of magnon BEC theory using electrical transport property including MR along with magnetic measurements and choosing large grained samples where the chance of occurrence of superparamagnetism is severely minimized.

1.5. Current driven domain wall motion:

1.5.1. Theoretical work:

When high density DC-current passes perpendicular to a domain wall (DW), the electrons crossing the wall apply a torque to it [39]. This electron flow tends to cant the wall spins in the current direction. Since, the wall thickness $\delta \sim 10$ nm is much larger than the electron wave length $\lambda \sim 0.5$ nm, a very smooth and gradual disturbance must be observed throughout the wall. The electron spin \vec{s} follows closely the direction of the intratomic (Hund) exchange field, which is parallel to the local magnetization \vec{M}_s . An analogy exists with the propagation of microwaves along a twisted rectangular waveguide where the twisting happens gradually over the distance δ . Therefore the

polarization vector of wavelength λ follows the local orientation and turned around. To reverse the direction of \vec{s} , \vec{M}_S must apply an exchange torque on \vec{s} . Inversely, \vec{s} creates a reaction torque on the wall, equivalent to an exchange field applied to M and having a component H_x^{ex} in the x directions normal to the wall:

$$H_x^{ex} \simeq j \left(\frac{\hbar}{M_S \delta} \right) \left(\frac{P \hbar}{e^*} \right) \quad (1.11)$$

, where j is the current density across the wall, well defined charge $e^* = \pm 1.6 \times 10^{-19} C$ and well defined spin polarization $P = \pm 1$. Also $\hbar = \pm 1$ is the wall "helicity" indicating whether \vec{M}_S turns clockwise or anticlockwise as the wall is crossed. For cobalt with $j = 10^9 A/m^2$ Eqn. 1.11 gives $|H_x^{ex}| = 35 A/m$.

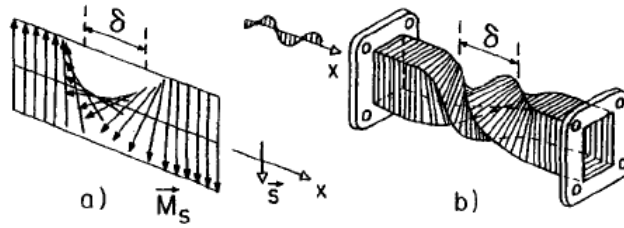


FIG. 1.13. a) A conduction electron of spin \vec{s} crosses a 180° domain wall. b) Analogy with a linearly polarized microwave propagating along a twisted waveguide. Reprinted from the permission of [39].

Due to the electrostatic interaction this exchange field tries to rotate the \vec{M}_S in x -direction. For uniform helicity the sample exhibits a non-zero average magnetization per unit volume:

$$\overline{M_x} \approx \mu_0 H_x^{ex} \frac{1 + \chi_d}{1 + D \chi_d} \left(\frac{\delta}{a} \right) \quad (1.12)$$

, where a is the spacing between walls, D is the demagnetizing coefficient of the sample and χ_d is the domain susceptibility in the x -direction normal to the wall.

The exchange field exerts a magnetic field $F_x = -g \mu_B \vec{s} \cdot (dH_x^{ex}/dx)$ on the magnetic moment $-g \mu_B \vec{s}$ of the conduction electron [40].

1.5.2. Experimental evidences:

Till date current driven domain wall motion has only been shown in conventional 3d metals and alloys and that too in Ni and Permalloy. The first experimental observation of domain wall displacement had been done by Berger et. al. [41]. A Bloch domain wall in $Ni_{80}Fe_{20}$ film was displaced by current pulse and it was observed by Kerr-contrast microscopy.

At the critical current density j_c a sequence of ~ 600 pulses was produced a detectable total wall displacement. The smallest detectable displacement was about 20 nm/pulse. The j_c vs film thickness w data was consistent with $j_c \propto w^{-2.1}$. The zero field DW displacement Δx_w values reach $\simeq 14 \mu m/pulse$ at a current of density 30 % above j_c , in a sample of thickness 263 nm.

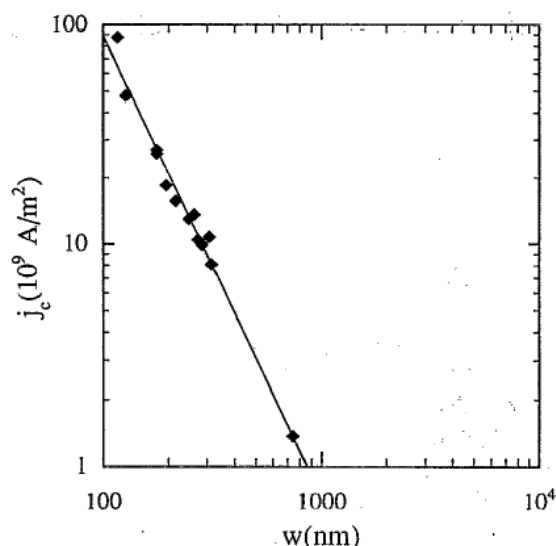


FIG. 1.14. Measured values of the critical current density j_c of $N_{81}Fe_{19}$ films vs film thickness w . The best-fitted straight line has a slope -2.1 and gives $j_c = 1.18 \times 10^{10}$ A/m 2 for $w = 263$ nm. Reprinted from the permission of [41].

Another work studied on the deepening of DW under the influence of a spin current [42]. The sample was F1/Cu/F2 multilayer spin valve where F1 and F2 both were exhibiting perpendicular magnetic anisotropy (PMA). The spin valve consist of $[Co(0.5)/Pt(1)]_4/Co(0.5)/Cu(6)/Co(0.5)/Pt(3)$ multilayer have been grown on $Si/Si_3N_4/Pt(1)/Au(20)/Pt(5)$ buffer layer. F1 and F2 were acted as reference layer where F1 had higher PMA value than F2. A 200 nm wide and 100 μ m long nanowire of this multilayer film was prepared by electron beam lithography and ion milling.

The extraordinary Hall effect (EHE) which is proportional to the perpendicular magnetization was used to detect DW motion inside the magnetic Hall cross (contacts E-F of FIG. 1.15(b)). At the end of the nanowire a large reservoir was made to inject a single DW. The EHE was measured using a Whetstone bridge with the magnetic field H_a perpendicular to the film. The EHE vs. DC current loop was offset for a field of $H_d = -140$ Oe which was consistent with the calculation of the dipolar stray field from the reference layer whose magnetization was pointing down here. The net perpendicular field in the free layer was thus $H_{fre} = H_a + H_d$. Effect of DC current is shown in FIG. 1.15(e)-(g) for net fields $H_{fre} = -10, -40$ and -60 Oe. For a positive current above a critical value $I_{c+}(H_{fre})$, the DW abruptly moves from position (2) to position (4) (exit of the Hall cross), which corresponds to a distance of ~ 90 nm. When the field is increased, I_{c+} is reduced.

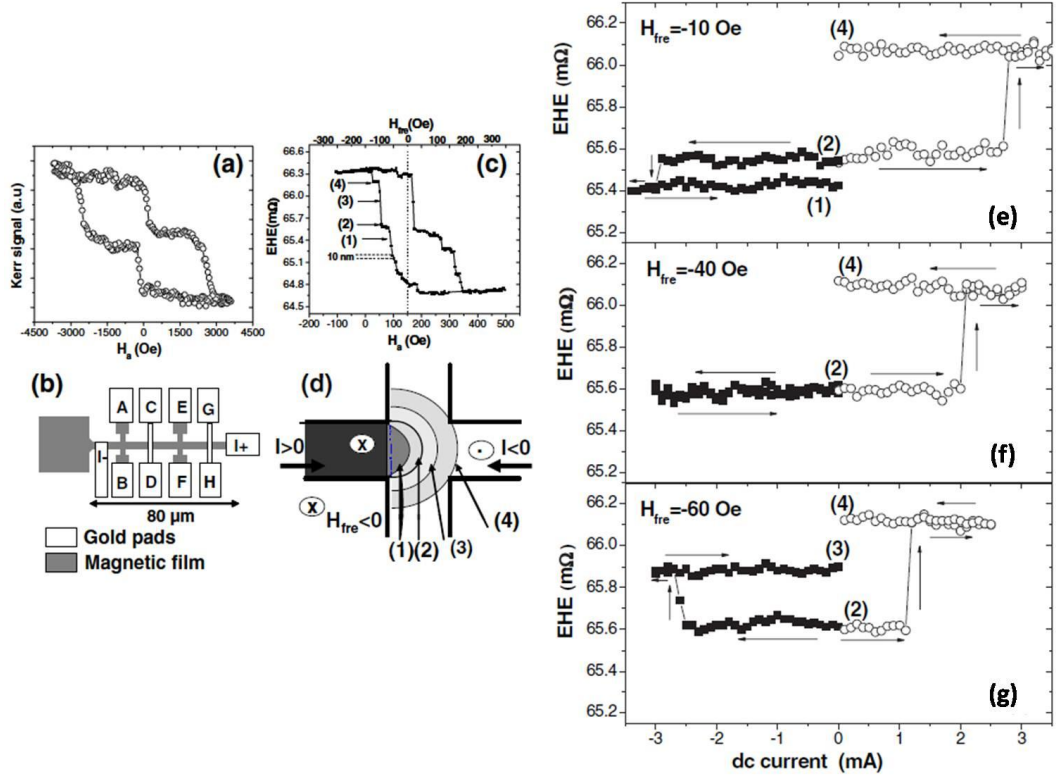


FIG. 1.15. (a) Polar Kerr hysteresis loop of our F1/Cu/F2 spin valves with PMA measured in a continuous film. (b) Schematic diagram of a top view of the device. (c) EHE minor hysteresis loop corresponding to the reversal of the free layer in a $200 \times 200 \text{ nm}^2$ Hall cross. A small EHE jump corresponding to DW motion over 10 nm is indicated. The EHE values (1) to (4) refer to the positions indicated in Fig. 1(d). (d) Bubble like behaviour of an ideal 1D Bloch DW in a magnetic Hall cross. The electron flow direction is indicated by the horizontal arrows. EHE as a function of the applied dc current for fields (e) $H_{fre} = -10$ Oe, (f) $H_{fre} = -40$ Oe, and (g) $H_{fre} = -60$ Oe. Measurements have been done by increasing the current from $I = 0$ to $I = \pm 3$ mA and then reducing it to $I = 0$, with a DW initially pinned at position (2). The negative (closed symbols) and positive (open symbols) current measurements have been realized independently. The states (1) to (4) refer to the positions in FIG. 1.15(d). The small Joule heating contribution has been subtracted. Reprinted from the permission of [42].

1.5.3. Experimental evidence from the resistance change:

Domain wall (DW) contributes a positive resistance. Levy and Zang [43] showed that the resistivity of a DW for current perpendicular to the wall can be expressed as,

$$\rho_{CPW} = \rho_0 \left[1 + \frac{\xi^2 (\rho_0^\uparrow - \rho_0^\downarrow)^2}{5 \rho_0^\uparrow \rho_0^\downarrow} \left(3 + \frac{10 \sqrt{\rho_0^\uparrow \rho_0^\downarrow}}{\rho_0^\uparrow + \rho_0^\downarrow} \right) \right] \quad (1.13)$$

, where ρ_0 is the resistivity without DW and $\rho_0^{-1} = 1/\rho_0^\uparrow + 1/\rho_0^\downarrow$. Resistivity due to up and down spin is represented here as ρ_0^\uparrow and ρ_0^\downarrow . Again $\xi = \pi \hbar^2 k_F / 4m\delta J$, where k_F is the Fermi wave vector, δ is the domain wall thickness and J is the exchange energy constant. Mass of the electron is m .

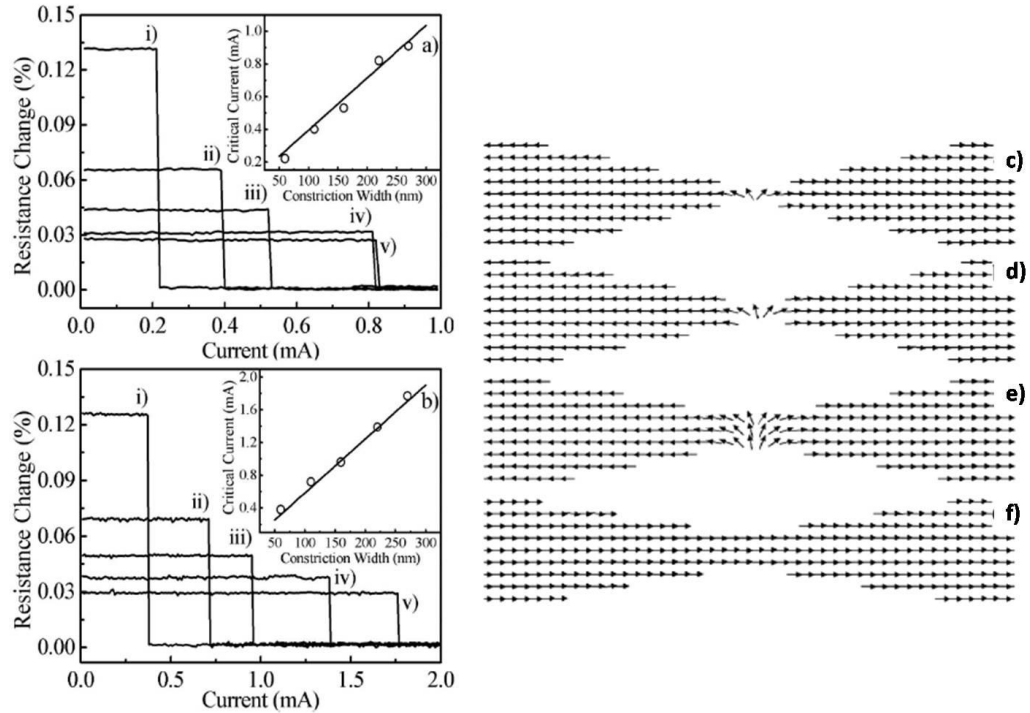


FIG. 1.16. $I - V$ measurements for (a) necked NiFe wires and (b) necked Ni wires with constriction widths of (i) 50 nm, (ii) 100 nm, (iii) 150 nm, (iv) 200 nm, and (v) 250 nm. In the insets of (a) and (b) the average critical current density is plotted as a function of constriction width for NiFe and Ni, respectively. Micromagnetic simulations for necked NiFe wires with constriction widths of (c) 50 nm, (d) 100 nm, (e) 250 nm, and (f) 300 nm. Reprinted from the permission of [44].

A set of Ni and Ni₈₀Fe₂₀ necked nanowire was made by Lepadatu et. al. [44] and confined a DW at the constricted region. The width of the necked region was varied from 50 nm to 350 nm. Above a critical DC current I_c the DW was extracted from the neck and the resistance of the sample was sharply dropped down. As the constriction width increases the value of I_c also increases but the resistance change decreases. The critical current density becomes of the order of 10^7 A/cm². The micromagnetic simulation confirmed the existence of an 180° Néel DW for a constriction of width < 300 nm. The ratio of the change of resistivity has a relation with the area of cross section S as $\Delta\rho/\rho \propto 1/S^\alpha$. The experimental result shows that the value of α for NiFe and Ni is respectively 0.42 and 0.3.

From the above discussions it is clearly conclude that the DW can be moved by the application of a DC current and this motion can be detected by the Kerr signal, EHE signal and resistance change of the sample.

1.6. Magnetism in binary alloy GdCo:

The Rare-earth (RE) and transition metal (TM) makes a ferrimagnetic alloy. The single atom spin moment of RE is larger than the TM atom moment. If the compositions are Gadolinium (Gd) and Cobalt (Co), RE-TM coupling becomes strong enough and it is anti-ferromagnetically coupled. In this case the occurrence of compensation temperature (T_{cm}) (total magnetization becomes minimum) is obvious.

1.6.1. Importance of GdCo:

Alloying of Gd, a local spin based ferromagnetic material with a conventional 3d metal that has itinerant ferromagnet will give rise to exotic spin order like Ferrimagnetism. Thus from the view point of basic magnetism as well as from potential applications binary Gd-Co alloys and intermetallics are interesting.

Previous works reported [45] that the Gd rich alloys and compounds of GdCo show very high magneto caloric effect (MCE). The magnetic entropy change ΔS is the measure of MCE.

$$\Delta S(T, H) = \frac{1}{\Delta T} \left[\int_0^H M(T + \Delta T, H) dH - \int_0^H M(T, H) dH \right] \quad (1.14)$$

From the isothermal magnetization curve ΔS was measured.

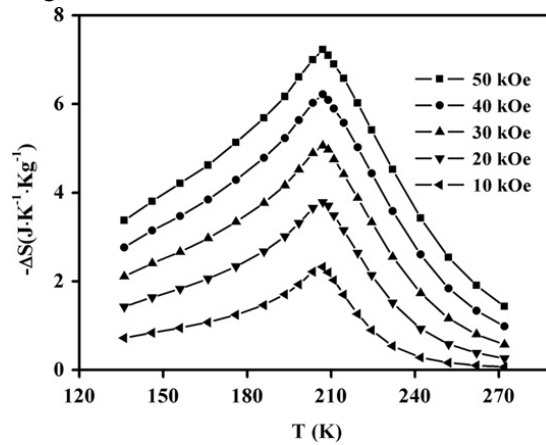


FIG. 1.17. Temperature dependence of isothermal magnetic entropy change for different magnetic field change of Gd_4Co_3 alloy. Reprinted from the permission of [45].

The magnetic entropy change of few Gd compositions like Gd_4Co_3 , Gd_3Co is very high. For Gd_4Co_3 it becomes $-7.2 \text{ Jkg}^{-1}\text{K}^{-1}$ at 50 kOe (see FIG. 1.17).

In the multilayer spin valve system Fe/Cu/GdCo the giant magnetoresistance (GMR) value depends on the GdCo composition as well as the thickness of the layer. At room temperature below 50 % concentration of Co the magnetization of GdCo composition is almost zero (FIG. 1.18(a)). The compensation composition x_C is around 80 at. % of Co. Below and above x_C the net magnetization is parallel and/or antiparallel with the magnetization of Gd and Co atom.

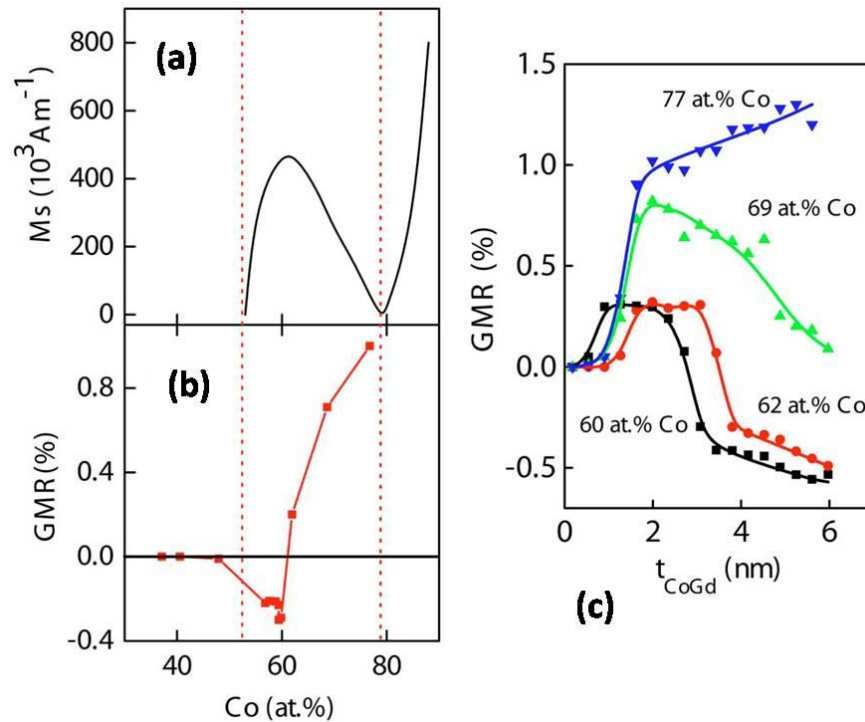


FIG. 1.18. (a) Dependence of magnetization at room temperature for GdCo alloy and (b) GMR ratio of the spin-valves Fe(2 nm)/Cu(3 nm)/GdCo(3.2 nm) on the Co content of GdCo alloys. Measurements were performed at room temperature. (c) Dependence of GMR ratio at room temperature on the GdCo layer thickness for various compositions of GdCo. The lines serve as a guide to the eye. Reprinted from the permission of [46].

For the GdCo thickness of 3.2 nm the GMR ratio is zero for Co content less than 50%. As the Co concentration is increased, GMR ratio becomes negative. The sign of GMR changes to positive for high Co concentration. Therefore for a fixed thickness GMR ratio strongly depends on the GdCo composition. FIG. 1.18 shows the GdCo thickness dependence of GMR for a fixed concentration. During the GdCo layer variation a crossover from positive to negative value of GMR is observed for low Co contents.

The Hall-effect measurement has been done on the Co rich amorphous alloy GdCo_3 [47]. From close to 0 K to room temperature the Hall resistivity ρ_H is independent of temperature and at the compensation temperature (T_{cm}) it changes sign. Above T_{cm} the magnetization shows that the Co moment is almost constant in this temperature region where Gd moment varies with temperature. This result confirmed that above T_{cm} , Hall effect is associated with Co moment and the magnetization of Co becomes parallel with the applied field. The form of the hysteresis loop also changes below and above T_{cm} .

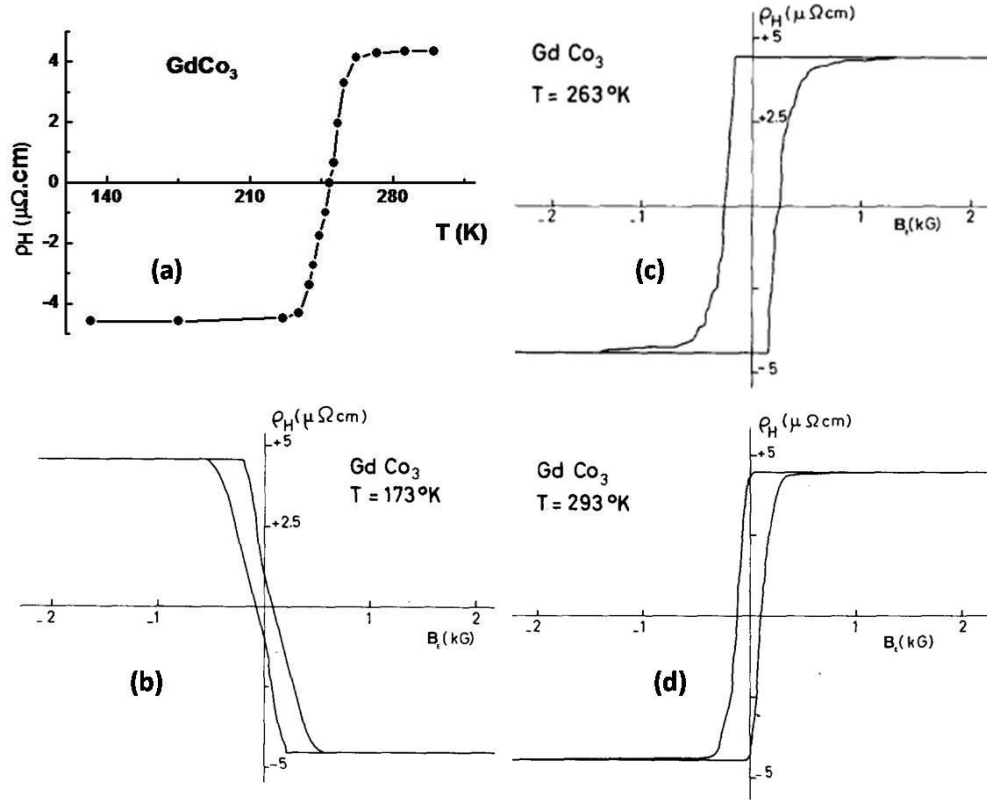


FIG. 1.19. (a) Saturation Hall resistivity as a function of the temperature. (b), (c) and (d) is the observed hysteresis loop. B_E is the external magnetic field. Reprinted from the permission of [47].

1.6.2. Magnetization compensation temperature T_{cm} :

In a binary Gd-Co where the magnetic nature of the two constituents is different it is likely that the Gd and Co will form sublattices. In a binary alloy of GdCo the total magnetization becomes the resultant vector of the magnetization of the sublattice atoms (Gd and Co). It can be expressed as,

$$\vec{M}_T = \lambda \vec{M}_{Gd} + \mu \vec{M}_{Co} \quad (1.15)$$

, where $\lambda + \mu = 1$ and M_{Gd} and M_{Co} are the sublattice magnetizations. The Gd and Co moments are antiferromagnetically coupled. Therefore M_T strongly depends on the temperature and the composition. At the compensation temperature (T_M), M_T becomes minimum or $M_T \rightarrow 0$, as $\lambda M_{Gd} = -\mu M_{Co}$.

In GdCo composition collinear structures are expected and therefore for a wide range of composition ferrimagnetic order exist. In the Gd rich composition there has not any T_{cm} . Only the Curie temperature (T_C) is observed. As the Co concentration increases, T_{cm} appears. But for very high Co concentration T_{cm} again disappears (see FIG. 1.20 (a)). At 4.2 K the compositional compensation concentration of $\text{Gd}_{1-x}\text{Co}_x$ alloy is $x_M \sim 0.8$.

The saturation magnetization M_S and the coercive field H_C is related as $H_C \propto 1/M_S$. Since at T_{cm} , M_S becomes minimum or zero H_C diverges (see FIG. 1.20 (c)). This could also be a measure of T_{cm} .

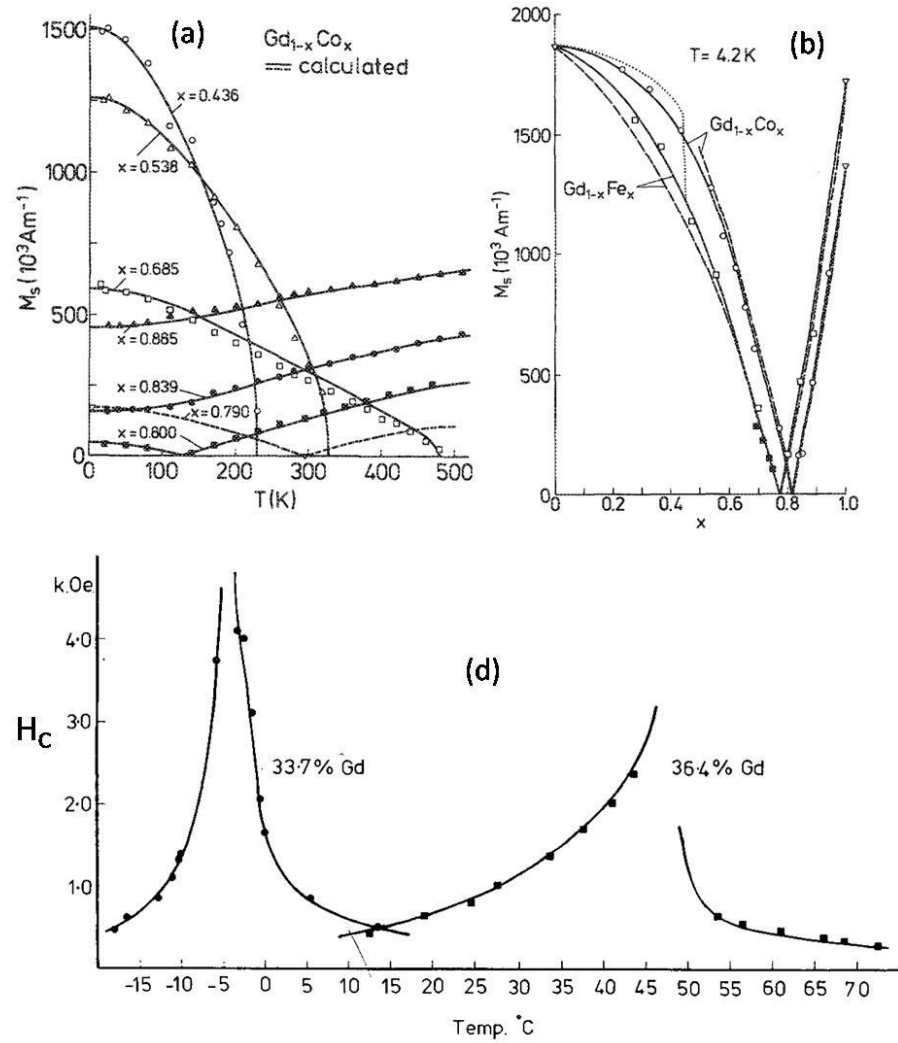


FIG. 1.20. (a) Temperature dependence of the saturation magnetization for GdCo alloys. The solid and dashed lines were calculated from the mean-field theory. (b) Compositional variation of the saturation magnetization for GdFe and GdCo alloys at $T = 4.2 \text{ K}$. Reprinted from the permission of [48]. (c) The temperature dependence of the coercivity for films of GdCo with compositions 33.7 % and 36.4 % of Gd. Reprinted from the permission of [49].

1.6.3. Tuning of T_{cm} :

Recent numerical analysis [50] on the magnetization of the binary alloy system reported the key point of tuning the value of T_{cm} . They considered a system of two spin S and σ which were located on alternating sites of a square lattice. The Hamiltonian of the system is,

$$H = -J_1 \sum_{\langle nn \rangle} S_i^A \sigma_j^B - J_2 \sum_{\langle nmn \rangle} S_i^A S_k^A - D \sum_i (S_i^A)^2 - D \sum_j (\sigma_j^B)^2 \quad (1.16)$$

, where S^A and σ^B are the spins of sublattices A and B . The nearest neighbour and next-nearest neighbour exchange constant are J_1 and J_2 . The crystal field or the single atom anisotropy energy coefficient is D . Again the sublattice magnetization M_A and M_B can be represented as,

$$M_A = \frac{2}{L^2} \langle \sum_i S_i^A \rangle, M_B = \frac{2}{L^2} \langle \sum_j \sigma_j^B \rangle$$

$$M_T = \frac{1}{2} (M_A + M_B) \quad (1.17)$$

, where L is the system size and M_T is the total magnetization.

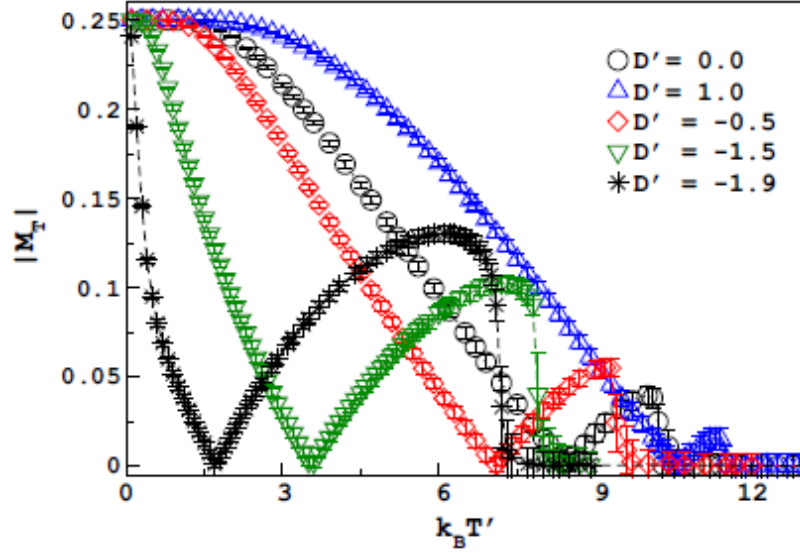


FIG. 1.21. Temperature dependence of the absolute value of the total magnetization per spin, for several values of D' and $J_2' = 1.0$. Reprinted from the permission of [50].

Using Monte Carlo simulation the value of M_T was calculated from Eqn. 1.17. In FIG. 1.21 the parameters are normalized by J_1 as, $D' = D/|J_1|$, $J_2' = J_2/|J_1|$ and $T' = T/|J_1|$. For $D' = 0$ a compensation temperature still exist in the M_T vs T' curve. This phenomenon indicates the importance of the interaction term J_2' for the existence of the compensation. The value of D' confirms the location of the compensation temperature. Therefore by changing the value of D' one can easily tune the position of T_{cm} .

This alloy has a potential application in spintronic devices. There has a certain range of the RA product (resistance \times contact area) of Ferromagnet (FM)/Insulator (I)/Si contact for which magnetoresistance (MR) can be visible in spintronic devices. If the ferromagnets are Co and $\text{Ni}_{80}\text{Fe}_{20}$, the RA product becomes eight to ten orders larger than the desired value. Therefore the observation of MR in Si spintronic device is not possible. Here the insulator is Al_2O_3 . By adjusting the tunnel barrier thickness (insulator thickness) one can adjust the RA product. But in this case the reverse bias Schottky barrier dominates over the resistance of the contacts rather than the tunnel barrier. Therefore for the low doped Si the RA product varies very little as the thickness of the tunnel barrier changes.

Using a material of low work function that is a ferromagnet the Schottky barrier height (Φ_B) can be reduced. Gd is the only material with work function ($\Phi_m = 3.1$ V) which is lower than the work function of Co, Ni, Fe and $\text{Ni}_{80}\text{Fe}_{20}$ and it has a large tunnel spin polarization (TSP). Therefore the FM/I/Si tunnel contact consisting of Si/ Al_2O_3 (0.5 nm)/Gd(0-5 nm)/ $\text{Ni}_{80}\text{Fe}_{20}$ (10 nm)/Au(10 nm) has eight orders smaller RA product value. The value is $\sim 10^{-7} \Omega\text{m}^2$. The T_C value of Gd is 293.2 K [8] and therefore the effect of Gd cannot be utilized above room temperature. The Φ_m value of GdCo alloy can be tuned

by tuning the composition. If we use this alloy in place of Gd, the TSP increases at high temperature [51] and the device could be used above room temperature.

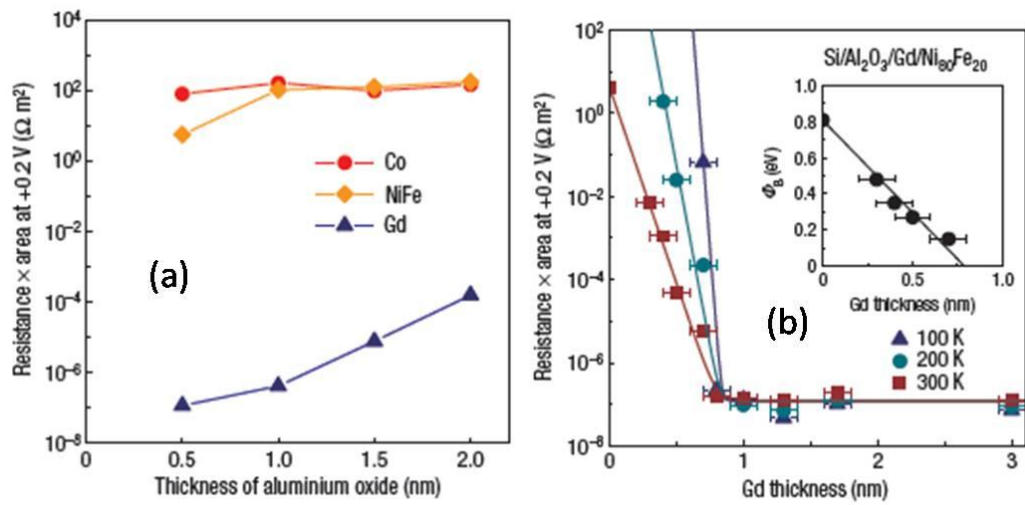


FIG 1.22. (a) Resistance–area product of the tunnel contact at the reverse bias of +0.2 V versus the thickness of the Al₂O₃ tunnel barrier. The red (orange) data is for the Si/Al₂O₃/Co (Ni₈₀Fe₂₀) (15nm) contacts; the blue data is for the Si/Al₂O₃/Gd (15 nm) contacts. (b) Resistance–area product of the Si/Al₂O₃ (0.5 nm)/Gd/Ni₈₀Fe₂₀ (10 nm) contacts at a reverse bias of +0.2 V versus the thickness of the Gd interlayer. The solid lines are a guide to the eyes. The inset shows the Schottky barrier height (Φ_B) of the contact versus the thickness of the Gd interlayer. The error bars denote the accuracy of the determination of the Gd thickness. Reprinted from the permission of [51].

In this thesis we investigate the size induced tuning of T_{cm} in NWs of Gd-Co alloy.

The thesis is organized in the following chapters:

Chapter 2: Sample preparation and Experimental techniques for characterization and physical measurements are described in details.

Chapter 3: Detailed study of the low field MR of polycrystalline Gadolinium with varying grain size to investigate the effect of size reduction on anisotropy energy and the Spin Reorientation transition temperature.

Chapter 4: Low field MR of single Gadolinium nanowire has been studied and compared the results with the value of bulk sample. The motivations are similar to those in Chapter 3.

Chapter 5: Bose Einstein condensation (BEC) of Magnons in nanostructured films of Gd at low temperature has been studied and it was established that BEC has a clear signature in electrical resistivity as well as magnetoresistance. The main effect is the softening of the Spin wave stiffness constant that can be quantitatively evaluated from temperature dependent magnetization data. The resulting softening as evaluated can quantitatively explain the resistance anomaly and MR field dependence.

Chapter 6: This chapter describes the current induced Domain wall motion in a nanoconstriction in a micro strip of Gd and the resulting effect was used to determine the anisotropy energy in magnetic thin film with micro/nano constriction.

Chapter 7: Magnetization compensation temperature T_{cm} of Gd_xCo_{1-x} ($x = 0.4$) alloy nanowire (diameter ~ 100 nm) has been studied and understand the discrepancy in result from its bulk value.

Chapter 8: Conclusion.

References:

1. F. Döbrich, J. Kohlbrecher, M. Sharp, H. Eckerlebe, R. Birringer and A. Michels, *Phys. Rev. B*, **85**, 094411 (2012).
2. D. H. Ryan, A. Michels, F. Döbrich, R. Birringer, Z. Yamani and J. M. Cadogan, *Phys. Rev. B*, **87**, 064408 (2013).
3. S. P. Mathew and S. N. Kaul, *J. Phys.: Condens. Matter*, **24**, 256008 (2012).
4. G. L. F. Fraga, P. Pureur and L. P. Cardoso, *J. Appl. Phys.*, **107**, 053909 (2010).
5. P. M. Shand, J. G. Bohnet, J. Goertzen, J. E. Shield, D. Schmitter, G. Shelburne and D. L. Leslie-Pelecky, *Phys. Rev. B*, **77**, 184415 (2008).
6. D. Michels, C. E. Krill III and R. Birringer, *J. Magnetism and Magnetic Material*, **250**, 203 (2002).
7. M. A. Ruderman and C. Kittel, *Phys. Rev.*, **96**, 99 (1954).
8. H. E. Nigh, S. Legvold and F. H. Spedding, *Phys. Rev.*, **132**, 1092 (1963).
9. C. Ward, G. Scheunert, W. R. Hendren, R. Hardeman and M. A. Gubbins, *Appl. Phys. Lett.*, **102**, 092403 (2013).
10. S. Yu. Dan'kov, A. M. Tishin, V. K. Pecharsky and K. A. Gschneidner, Jr., *Phys. Rev. B*, **57**, 3478 (1998).
11. C. D. Graham, Jr., *J. Appl. Phys.*, **34**, 1341 (1963).
12. W. D. Corner and B. K. Tanner, *J. Phys. C: Solid State Phys.*, **9**, 627 (1976).
13. M. B. Salamon and D. S. Simons, *Phys. Rev. B*, **7**, 229 (1973).
14. R. L. Smith, W. D. Corner and B. K. Tanner, *J. Magn. Magn. Mater.*, **20**, 265 (1980).
15. M. Romera, M. Muñoz, P. Sánchez, C. Aroca and J. L. Prieto, *J. Appl. Phys.*, **106**, 023922 (2009).
16. K. Maezawa, T. Mizushima, K. Mori, K. Sato, Y. Saito and S. Wakabayashi, *J. Phys. Soc. Jpn.*, **47**, 585 (1979).
17. K. A. Mcewen, G. D. Webber and L. W. Roeland, *Physica B*, **86**, 533 (1977).
18. T. Hiraoka and M. Suzuki, *J. Phys. Soc. Jpn.*, **31**, 1361 (1971).
19. J. M. Blatt, K. W. Böer and W. Brandt, *Phys. Rev.*, **126**, 1691 (1962).
20. S. P. Mathew and S. N. Kaul, *J. Phys.: Condens. Matter*, **27**, 056003 (2015).
21. A. Oosawa, M. Ishii and H. Tanaka, *J. Phys.: Condens. Matter*, **11**, 265 (1999).
22. T. Nikuni, M. Oshikawa, A. Oosawa and H. Tanaka, *Phys. Rev. Lett.*, **84**, 5868 (2000).
23. V. N. Glazkov and A. I. Smirnov, *Phys. Rev. B*, **69**, 184410 (2004).
24. A. Oosawa, T. Takamasu, K. Tatani, H. Abe, N. Tsujii, O. Suzuki, H. Tanaka, G. Kido and K. Kindo, *Phys. Rev. B*, **66**, 104405 (2002).
25. Ch. Rüegg, M. Oettli, J. Schefer, O. Zaharko, A. Furrer, H. Tanaka, K.W. Krämer, H.-U. Güdel, P. Vorderwisch, K. Habicht, T. Polinski and M. Meissner, *Phys. Rev. Lett.*, **93**, 037207 (2004).
26. B. S. Conner, H. D. Zhou, Y. J. Jo, L. Balicas, C. R. Wiebe, J. P. Carlo, Y. J. Uemura, A. A. Aczel, T. J. Williams and G. M. Luke, *Phys. Rev. B*, **81**, 132401 (2010).
27. A. A. Aczel, Y. Kohama, C. Marcenat, F. Weickert, M. Jaime, O. E. Ayala-Valenzuela, R. D. McDonald, S. D. Selesnic, H. A. Dabkowska and G. M. Luke, *Phys. Rev. Lett.*, **103**, 207203 (2009).
28. M. Kofu, H. Ueda, H. Nojiri, Y. Oshima, T. Zenmoto, K. C. Rule, S. Gerischer, B. Lake, C. D. Batista, Y. Ueda and S.-H. Lee, *Phys. Rev. Lett.*, **102**, 177204 (2009).
29. A. A. Aczel, Y. Kohama, M. Jaime, K. Ninios, H. B. Chan, L. Balicas, H. A. Dabkowska and G. M. Luke, *Phys. Rev. B (Rapid Com.)*, **79**, 100409(R) (2009).

-
30. M. Jaime, V. F. Correa, N. Harrison, C. D. Batista, N. Kawashima, Y. Kazuma, G. A. Jorge, R. Stern, I. Heinmaa, S. A. Zvyagin, Y. Sasago and K. Uchinokura, *Phys. Rev. Let.*, **93**, 087203 (2004).
 31. T. Radu, H. Wilhelm, V. Yushankhai, D. Kovrizhin, R. Coldea, Z. Tylczynski, T. Lühmann and F. Steglich, *Phys. Rev. Let.*, **95**, 127202 (2005).
 32. L. Yin, J. S. Xia, V. S. Zapf, N. S. Sullivan and A. Paduan-Filho, *Phys. Rev. Let.*, **101**, 187205 (2008).
 33. S. O. Demokritov, V. E. Demidov, O. Dzyapko, G. A. Melkov and A. N. Slavin. *New J. Phys.*, **10**, 045029 (2008).
 34. P. R. Johnson, E. Della Torre, L. H. Bennett and R. E. Watson, *J. Appl. Phys.*, **105**, 07E115 (2009).
 35. L. H. Bennett, E. Della Torre, P. R. Johnson and R. E. Watson, *J. Appl. Phys.*, **101**, 09G103 (2007).
 36. E. D. Torre, L. H. Bennett and R. E. Watson, *Phys. Rev. Let.*, **94**, 147210 (2005).
 37. S. N. Kaul and S. P. Mathew. *Phys. Rev. Let.*, **106**, 247204(2011).
 38. S. P. Mathew and S. N. Kaul, *J. Phys.: Condens. Matter*, **23**, 266003 (2011).
 39. L. Berger, *J. Appl. Phys.*, **49**, 2156 (1978).
 40. L. Berger, *J. Appl. Phys.*, **55**, 1954 (1984).
 41. E. Salhi and L. Berger, *J. Appl. Phys.*, **76**, 4787 (1994).
 42. D. Ravelosona, D. Lacour, J. A. Katine, B. D. Terris and C. Chappert, *Phys. Rev. Let.*, **95**, 117203 (2005).
 43. Peter M. Levy and Shufeng Zhang, *Phys. Rev. Let.*, **25**, 5110 (1997).
 44. S. Lepadatu and Y. B. Xu, *Phys. Rev. Let.*, **98**, 127201 (2004).
 45. Ji Liang Zhang, Zhi Gang Zheng, Wen Huan Cao and Chan Hung Shek, *J. Magnetism and Magnetic Material*, **326**, 157 (2013).
 46. D. Z. Yang, B. You, X. X. Zhang, T. R. Gao, S. M. Zhou and J. Du, *Phys. Rev. B*, **74**, 024411 (2006).
 47. R. Asomoza, I. A. Campbell, H. Jouve and R. Meyer, *J. Appl. Phys.*, **48**, 3829 (1977).
 48. P. Hansen, C. Clausen, G. Much, M. Rosenkranz and K. Witter, *J. Appl. Phys.*, **66**, 756 (1989).
 49. R. Carey, D. M. Newman and B.W.J. Thomas, *J. Phys. Colloques*, **46**, C6-19(1985).
 50. N. De La Espriella, C. A. Mercado and G. M. Buendía, *J. Magnetism and Magnetic Material*, **417**, 30 (2016).
 51. Byoung-chul Min, Kazunari Motohashi, Cock Lodder and Ron Jansen, *Nature Mater.*, **5**, 817 (2006).

CHAPTER 2

Sample preparation and Experimental techniques

In this chapter we present the sample preparation techniques as well as characterization and measurement techniques that have been used in the thesis. The sample preparation used techniques such as thermal evaporation, electron beam evaporation, integrated lithographic techniques, arc furnace and electrodeposition. The characterization of the samples were done with instruments like X-ray diffraction (XRD), Scanning electron microscope (SEM), Tunnelling electron microscope (TEM) and Atomic force microscopy (AFM). Magnetic measurements used Vibrating sample magnetometer (VSM) and Superconducting quantum interference device (SQUID) and mutual inductance based ac susceptibility set-up. Electrical resistance measurements were done using a 4 probe technique and the magnetoresistance at low field were measured with an air core solenoid and at higher field with a superconducting magnet.

2.1. Sample preparation

All the samples used in the work were made during the thesis work. The samples which were used in this thesis are all polycrystalline Gd samples of different dimensions and morphologies. The list of the samples which we used is given below:

- (a) Bulk polycrystalline ingot of Gd used as bulk after proper annealing treatment
- (b) Thick films of Gd with different grain sizes.
- (c) Gd nanowire made by Focused Ion Beam milling.
- (d) Microstrip of Gd with lithographically patterned nanoconstriction
- (e) GdCo alloy ingot and nanowire.

For all the Gd samples that starting material is same as that in the ingot and thus has the same purity.

2.1.1. Thermal evaporation

It is a very well known technique to prepare film samples and electrical contact pads. We used a vacuum chamber of air pressure $< 10^{-6}$ mbar. Inside the chamber a heater is connected through tungsten or molybdenum boat at which the ingot of the film sample material is placed. The substrate where the film will grow is placed at a distance just above the boat. The substrate or the film with substrate sometimes heated before or after deposition by substrate heater. Large amount of electric current is passed through the high resistance boat and by Joule heating the boat is heated in such a way that the sample material is melted and evaporated to the upward direction. With the contact of respectively cold surface of the substrate evaporation material is deposited onto it and makes a film.

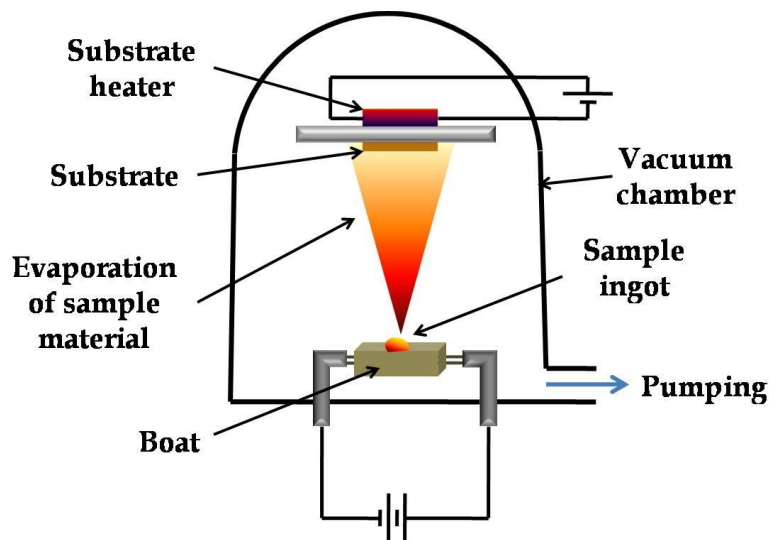


FIG. 2.1. Schematic representation of thermal evaporation with substrate heating.

In this thesis by this evaporator we prepared thick films (Film-A: 1.9 μm thick, Film-B: 250 nm thick) of Gd. The evaporation has been done on quartz substrate at 10^{-7} mbar at temperature 450°C . After that Film-A and Film-B was annealed at 500°C for 9 hours and 4 hours at 1 mbar of continuous Ar flow. Due to different annealing time average grain size of the samples were also different with the value 105 nm (Film-A) and 35 nm

(Film-B). The Ag and Au/Cr electrical contact pads were also prepared by thermal evaporation.

2.1.2. Electron beam evaporation

For this kind of evaporation a very high vacuum chamber is needed. High melting point sample can also be prepared by this method. The ingot of the sample is placed in a crucible of Al_2O_3 or Graphite and using a magnetic field an electron beam is focused on the ingot. Due to the high energy electron beam the material is melted and evaporated. This evaporated material then deposited on a substrate which is placed at a distance just above the crucible. The crucible is placed on a water cooled holder. The high vacuum and ultra high vacuum is created by Turbo molecular pump (TMP) and Ion Gauge pump (IGP) at a pressure level $\lesssim 10^{-8}$ mbar.

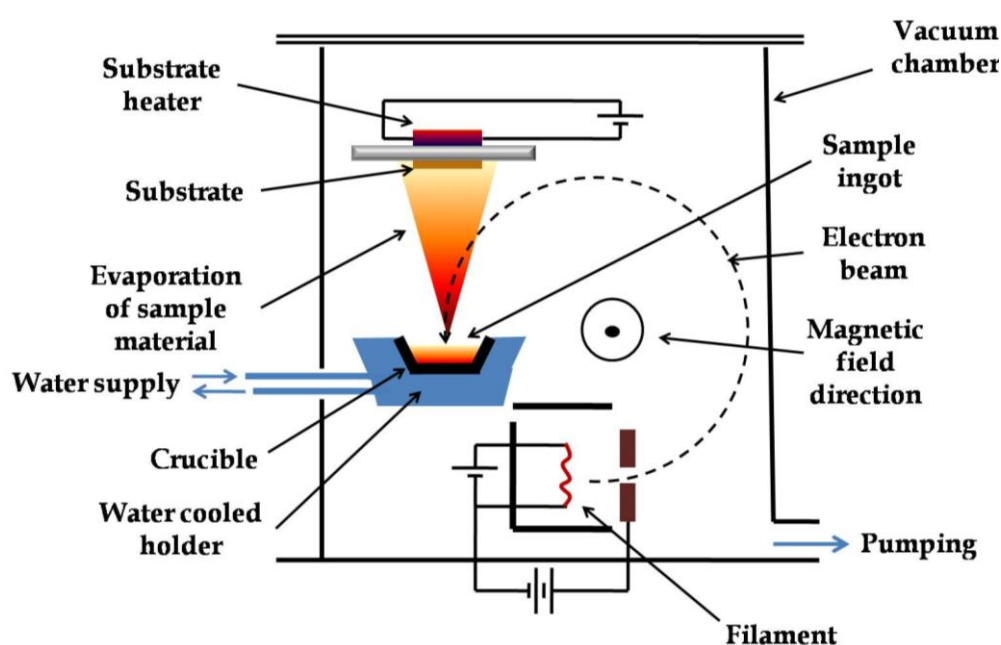


FIG. 2.2. Schematic representation of electron beam evaporation with substrate heating.

In this thesis thin film (thickness ~ 40 nm) of Gd was prepared on quartz substrate by electron beam evaporator at a base temperature 350°C . The evaporation rate was 0.05 nm/s. After that a 3 nm Au film was evaporated on the Gd film to protect it from the oxidation. The base pressure of the chamber was $\sim 5 \times 10^{-8}$ mbar.

2.1.3. Integrated lithography technique

On quartz substrate preparation of good quality Gd film is possible at a temperature $> 200^\circ\text{C}$ [1, 2]. Since electron beam lithography (EBL) resist PMMA is burned above 150°C , by EBL making of nanowire (NW) and nanoconstriction (NC) of Gd is impossible. To make Gd NW and NC we avoided the conventional photo or electron beam lithography and followed an integrated lithography technique.

In this process we first by thermal or electron beam evaporation prepared Gd film on quartz substrate. Then the film was covered by photo resist SU8. After that we did photo lithography in such a way that only a rectangular strip on the film was covered by

SU8. Then the total sample was immersed into 5 % HCl solution. The bare open surface of the metal Gd was etched out by acid. Only the rectangular strip area was protected by SU8 from the acid. Thereafter by photo resist remover SU8 was removed from the rectangular surface and a rectangular strip of Gd was prepared on the quartz substrate. Then by Focused Ion Beam (FIB) milling process NW and NC was prepared on the rectangular strip of Gd.

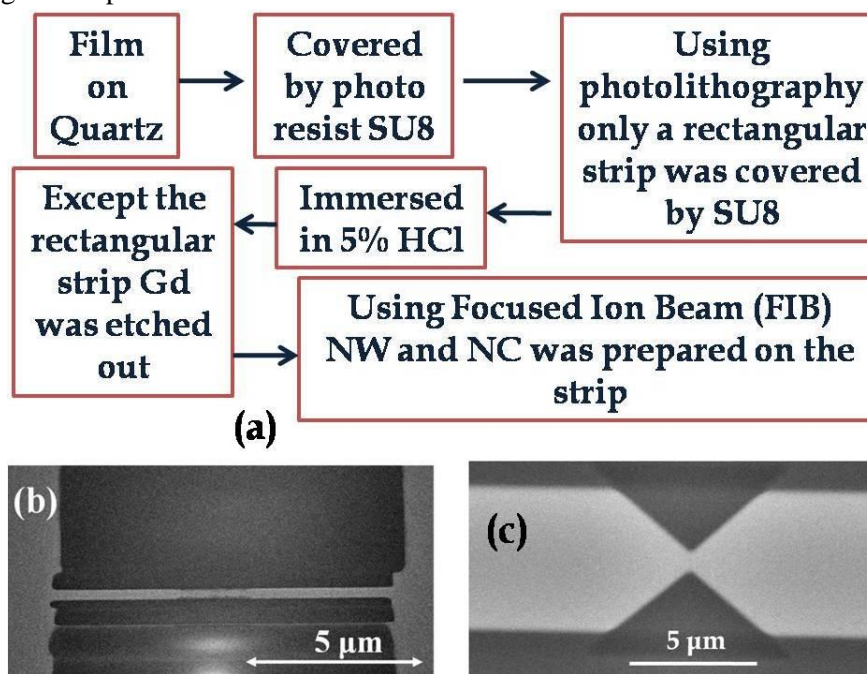


FIG. 2.3. (a) Flow-chart of the integrated lithography route of NW and NC preparation. SEM image of the Gd (b) NW and (c) NC is prepared by this process.

Dual beam FIB is a compound system by which one can do multiple works like imaging by electron or ion source, milling by ion source, contact pad preparation by Pt deposition, nanostructure transplantation from one place to another place by Omni probe and TEM sample preparation. In FIB Ga ion is used as an ion source.

2.1.4. Electrical contact pad preparation

On the NW and NC samples the electrical contact pads were made by electron and Ion beam lithography techniques. The bigger contact pads were prepared by direct evaporation of metal through a Si mask. This mask was made by etching of Si wafer by the Reactive Ion etching using SF_6 gas and a litho mask. In this process we achieved a precision distance of 50 μm between two pads. At first a pattern was prepared on the Si wafer by photolithography. Here SU8 resist was used. Then the open portion was plasma etched completely through the wafer using an STS 100 inductively coupled plasma etcher with a gas mixture of SF_6/O_2 . Si was etched out by SF_6 and a multi-padded hard mask of Si wafer was prepared in this way. Direct evaporation of Ag or Au/Cr has been done for making contact pads. In case of Au/Cr evaporation first Cr of thickness 3-5 nm was evaporated and then 50 nm Au was evaporated. Only Au does not stick very well on quartz or Si substrate.

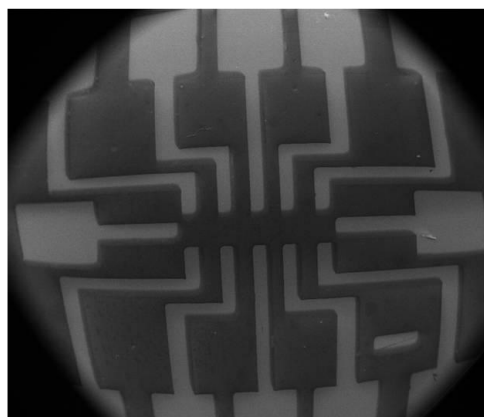


FIG. 2.4. SEM image of the Ag pad on quartz substrate prepared by direct evaporation through Si hard mask.

The next step was electron beam lithography. In this process the substrate with sample and bigger contact pads was covered with electron beam resist Polymethyl Methacrylate (PMMA). The resist coating has been done by a spin coater. First PMMA-350k was spin coated at 2900 rpm for 40 s. Then it was baked at 180 °C for 1.5 min. After that the sample was spin coated again by PMMA-950k at 6000 rpm for 40 s. Then it was baked again at 120 °C for 90 min. Double resist coating is needed for undercutting by which the success rate of the process increases (see FIG. 2.5). After preparing the resist coated substrate with sample was put inside a Scanning Electron Microscope (SEM) and a patterned was written by electron beam on the resist. This written portion was washed out by 3:1 Methyl Iso-butyl Ketone (MIBK): Iso-profile Alcohol (IPA) solution. Then metal evaporation has been done and the pattern was developed by Acetone.

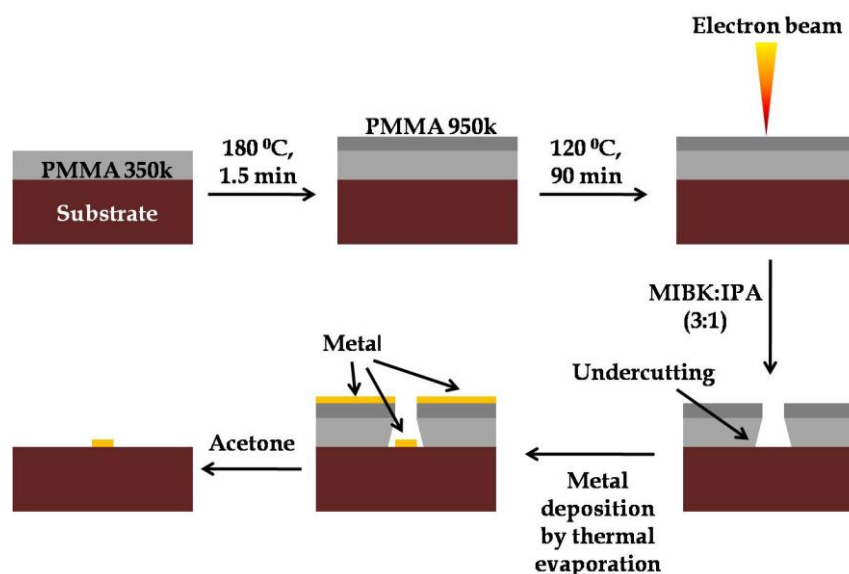


FIG. 2.5. Schematic diagram of electron beam lithography process.

Ion beam lithography is a special case. When the abrupt height differences in the upper plane of the substrate are present (present in ion beam prepared sample), simple electron beam lithography makes discontinuous contact pads. In ion beam deposition metal does not deposited directly. Here high energy ions are bombarded on the substrate/sample and secondary electrons are generated. During this process the precursor gas of methylcyclopentadienyl platinum trimethyl $(\text{CH}_3)_3(\text{CH}_3\text{C}_5\text{H}_4)\text{Pt}$ which is focused at the

desired position is broken by this high energy Ga^+ ions and metal is isotropically deposited with amorphous C. Since in this case the metal ions are deposited isotropically, the problem in electron beam deposition is solved here (see FIG. 2.6). Also the metal which is deposited by ion beam has high resistance. Therefore it is very effective in voltage lead preparation.

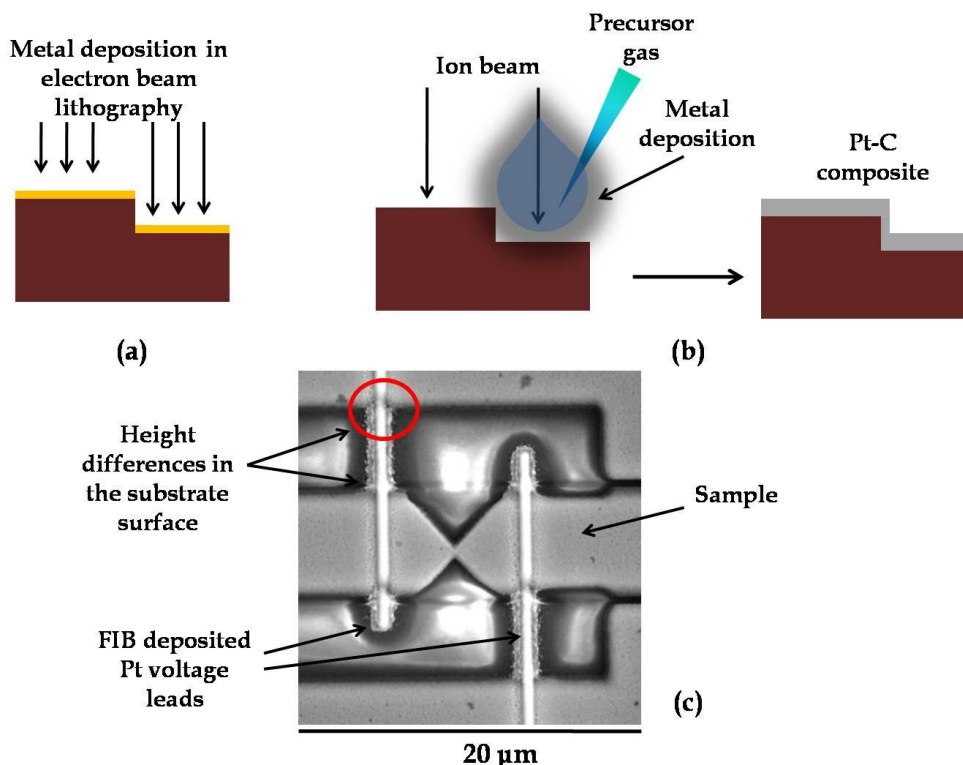


FIG. 2.6. Schematic diagram of (a) electron beam lithography metal deposition and (b) Ion beam deposited Pt deposition on a substrate with abrupt height differences on the surface. (c) SEM image of FIB deposited Pt voltage leads which are connected on Gd nanoconstriction sample.

In FIB system we have deposited Pt to make electrical contact pads at 30 kV voltage and 28 pA current. In this condition the resistance of the FIB deposited Pt metal becomes minimum. The resistance of this metal highly depends on the deposition condition. It is basically a composite of Pt and C. Details of this Pt-C composite nano leads is discussed in Appendix-A.

2.1.5. Arc furnace

Arc furnace that has been used consists of a chamber where in presence of inert gas (Ar) electric arc is created to melt the metals and thus prepare alloys from metal ingots. At first the chamber is pumped down to a pressure $< 10^{-5}$ mbar. Then the inert gas, generally Ar, is introduced into the chamber. Two Tungsten tip rods are present inside the chamber and the rods are connected with a high voltage power supply. These rods are electrodes. Metal ingots are placed above a Cu plate which is the crucible. A water supply is present to cool the crucible. When power is applied and the tips of the rods are brought very close to each other, due to the presence of Ar, an arc is created between the sharp tips of the rods. This arc is used to melt the metal ingots. By the mixing of melted metals the alloy is formed. The homogeneity of the alloy is increased by repeating the processes.

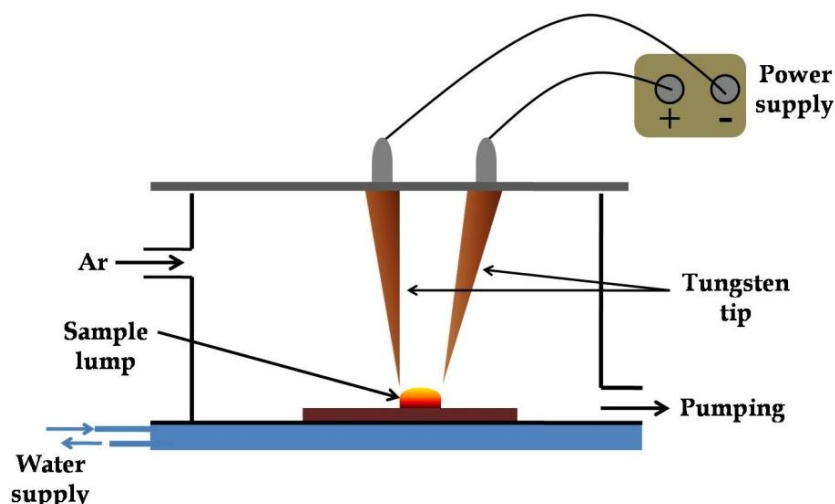


FIG. 2.7. Schematic diagram of an arc furnace.

2.1.6. Electrodeposition

Electrodeposition which is widely used is a very well established simple low cost technique by which long parallel metal and alloy nanowire can be prepared very easily using a template [3]. In a simple process two conducting plate is poured inside an electrolyte solution and the plates are connected with a battery of different polarity. Metal ions (M^{+ne}) are deposited on the cathode plate (negative polarity) and neutralized by taking electrons. In case of mixed salt electrolyte different kind of metal ions are presents (M_1^{+ne} , M_2^{+me} , M_3^{+pe} etc.) and they are simultaneously deposited for a particular potential difference between the plates. Michel Faraday by his Faraday's law of electrodeposition first quantified the amount of depositing material m .

$$m = \frac{E}{F} Q \quad (2.1)$$

, where E is the equivalent weight, F is the Faraday number 96485 and Q is the total deposited charge.

Two kinds of deposition techniques are present. One is Galvanostatic and another one is Potentiostatic. In Galvanostatic electrodeposition a constant current is passing between the electrodes inside the electrolyte. The deposition occurs at an optimum current.

In Potentiostatic electrodeposition an additional electrode which is called the reference electrode is used in the electrolytic cell [4]. This is called three electrode system where the electrodes are counter electrode (CE), working electrode (WE) and reference electrode (RE). In two electrode system simultaneously current measurement with maintaining constant potential is extremely difficult. To solve this problem, the role of supplying electrons and referencing potential has been divided between two separate electrodes. The RE is a half cell with a known reduction potential. Its only role is to act as reference in measuring and controlling the working electrodes potential and any current does not pass through it. The CE passes all the current needed to balance the current observed at the working electrode. The deposition occurs at a constant potential of the working electrode with respect to the reference electrode. Potentiostatic deposition is widely used in nanowire preparation.

Commercially available Anodic Aluminium Oxide (AAO) templates are used here. AAO templates have nano channels of length 50 μm . The template which was used here

has a pore diameter 100 nm and pores are uniformly distributed. One side of AAO has been coated with metal by thermal evaporation. This metal coated AAO was used as WE. Calomel electrode ($\text{Hg}/\text{Hg}_2\text{Cl}_2$) was used for RE and Platinum plate was for CE.

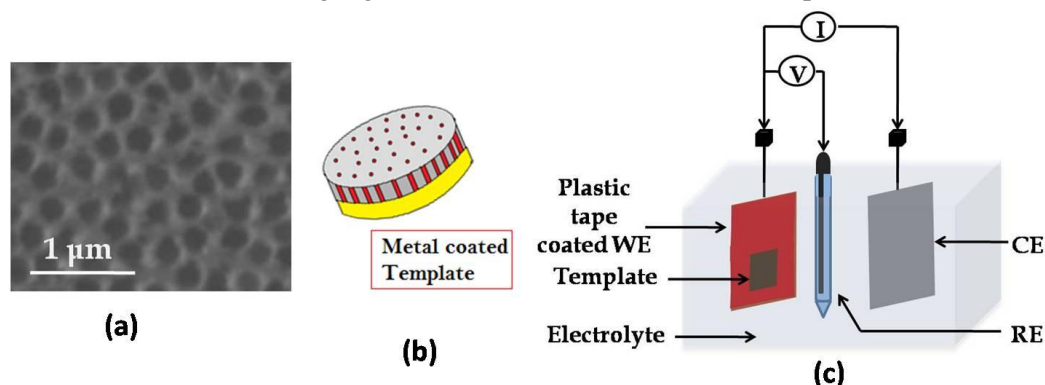


FIG. 2.8. (a) SEM image of the top view of an AAO. (b) Schematic diagram of metal coating on a template. (c) Schematic diagram of nanowire preparation by three electrode system electrodeposition method.

In case of $\text{Gd}_{0.4}\text{Co}_{0.6}$ alloy nanowire preparation one side Ag coated AAO template of 100 nm pore diameter was used as a working electrode. The electrolyte contained 0.2 M $\text{GdCl}_3 \cdot 7\text{H}_2\text{O}$; 0.2 M $\text{CoSO}_4 \cdot 5\text{H}_2\text{O}$ and 0.3 M H_3BO_3 .

After preparing the electrolyte cell cyclic voltammetry (CV) is the method by which one can find out the actual reduction potential. In cyclic voltammetry, the electrode potential ramps linearly versus time. This ramping is known as the experiment's scan rate (V/s). The potential is measured between the reference electrode and the working electrode and the current is measured between the working electrode and the counter electrode. This data is then plotted as current (i) vs. potential (E). The forward scan produces a current peak for any analytes that can be reduced (or oxidized depending on the initial scan direction) through the range of the potential scanned. The current will increase as the potential reaches the reduction potential of the analyte, but then falls off as the concentration of the analyte is depleted close to the electrode surface. If the redox couple is reversible, the applied potential is reversed and it will reach the potential that will reoxidize the product formed in the first reduction reaction. This produces a current of reverse polarity from the forward scan. The oxidation peak will usually have a similar shape to the reduction peak. From the CV data the oxidation potential of $\text{Gd}_{0.4}\text{Co}_{0.6}$ nanowire preparation was found out at -2.5 V.

After finding the oxidation potential nano wire could be prepared by DC electrolysis or Pulsed electrolysis.

DC electrolysis: In this case a constant potential is applied at the cathode. Generally oxidation potential is used as a constant potential here. At first when the potential is applied, the current at CE becomes very high due to the double layer at the surface of cathode (WE). The current decreases rapidly and after few times later again increases. This increase of current indicates to fill up the nano channels. When the channels are completely filled, the current becomes saturated. In our work for 100 nm GdCo NW preparation at -2.5 V DC bias overgrowths had been started after 90 s.

Pulsed electrolysis: Using DC electrolysis, preparation of nano wire with dimension below 100 nm is very difficult. Positive ion clouds are generated inside the nano channels. These clouds oppose the positive ions to reach the cathode. Ion clouds are not generated in case of pulsed electrolysis. Here a pulsed potential is applied at the cathode

(WE). Oxidation potential is used for the negative pulse height. Cloud generation depends on the pulse width. In between two negative pulses one can use a small positive pulse to create a good quality single crystalline wire. For very low mobility ions, the rate of deposition is very slow and the current pulse height is also small. But slow deposition increases the quality of the wires. A small positive potential can be applied to reduce some ions from the deposited material and to avoid the ion cloud generation.

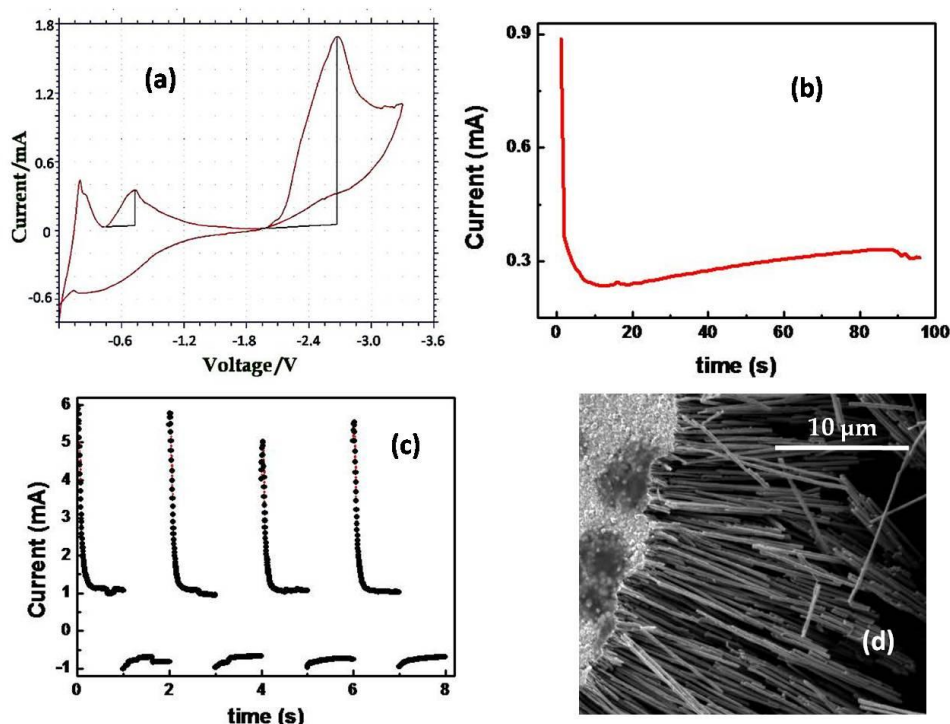


FIG. 2.9. (a) Cyclic Voltammometry curve (b) DC current vs. time curve and (c) Pulse current vs. time curve of GdCo alloy nanowire preparation. (d) SEM image of $Gd_{0.4}Co_{0.6}$ 100 nm diameter nanowires hanging from the Ag later.

2.2.Characterization

(a) X-ray diffractometer (XRD)

The crystal structure of the samples has been decided by XRD. X-ray is an electromagnetic wave and it is scattered by atoms sitting in parallel planes in the crystal. If X-ray of wavelength λ falls into a crystal, it reflects and detect by a detector. According to the Brag's law,

$$2d \sin \theta = n\lambda \quad (2.2)$$

, where d is the distance between two parallel atomic planes. θ is the angle between incident X-ray and the atomic planes. n is an integer number. We have used Cu $K\alpha$ radiation of wavelength $\lambda = 0.15418$ nm.

X-ray diffraction measurements have been done by X'Pert PRO diffractometer [5]. In this system the sample remains fixed. The X-ray tube and detector both are rotated with an angle θ . In this thesis work we basically measured XRD of bulk ingots, thin and thick films on quartz substrate and nanowires inside AAO template. Here is an example of the XRD pattern of bulk Gd and GdCo alloy (see FIG. 2.10). Gd has a hexagonal crystal structure. Our sample was polycrystalline where (0002) orientation

showed maximum intensity. Again bulk GdCo alloy has an amorphous structure and there has no XRD peak.

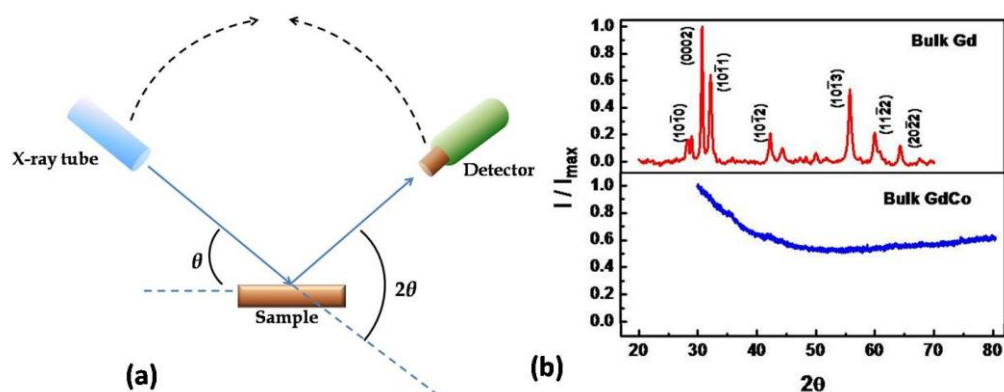


FIG. 2.10. (a) Schematic representation of XRD system. (b) Normalized XRD (I/I_{max}) of bulk Gd and GdCo alloy. I_{max} is the maximum intensity.

(b) Atomic Force Microscope (AFM)

In this thesis the surface morphology and the thickness of a film was determined by AFM [6]. In AFM a cantilever with a sharp tip or probe (nanometer order) moves on the surface of the film and according to the roughness of the film the cantilever tip gets up and down. A laser light is projected on the head of the tip. According to the roughness of the surface of a film the position of the reflected laser light is changed. This position change is detected by a detector which is connected with the cantilever through a feedback electronic circuit. The force between the probe and the surface of the sample is determined here. AFM is basically a scanning probe microscope which has two different imaging modes. One is contact mode and another one is non contact mode or tapping mode.

The grain size at the surface of our Gd film samples was determined by AFM. The thick Gd film (thickness $\sim 1.4 \mu\text{m}$) sample has elongated grains with average grain sizes $\sim 128 \text{ nm}$ (along length) and $\sim 80 \text{ nm}$ (along width) (see FIG. 2.11(b)). Using AFM we also measured the thickness of our Gd thin film sample which has been prepared by electron beam evaporator. The measured thickness was $\sim 40 \text{ nm}$.

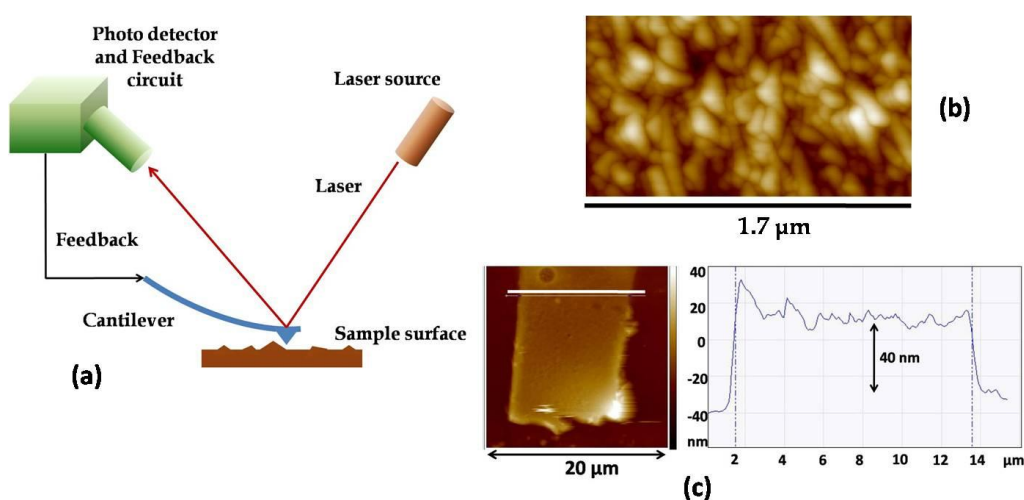


FIG. 2.11. (a) Schematic representation of AFM. (b) AFM image of the surface of Gd film. (c) Gd film thickness determination by AFM.

(c) **Electron microscope**

There are two kind of electron microscope which we used. One is Scanning Electron Microscope (SEM) and another one is Transmission Electron Microscope (TEM). Due to a high energy electron bombardment a sample produces Secondary electrons, Backscattered electrons, Auger electrons, Transmission electrons, characteristics X-ray, Continuum X-ray and Cathodoluminescence.

Scanning Electron Microscope (SEM): In SEM a high energy electron beam is thermionically emitted from an electron gun. The filament of the emitter is basically made by tungsten which has high melting point and low vapour pressure. The emitted electron beam has energy up to 30 keV and it is focused by one or two condenser lenses within a spot of range 0.5 nm to 5 nm diameter. In the sample the primary electrons (PE) due to random scattering lose energy and trapped within a teardrop shape volume. The volume depth could be 5 μm from the surface. For random inelastic collision of the PEs with the surface atoms of the sample from the k-shell of the atoms Secondary electrons (SE) are generated. These low energy (< 50 eV) SEs are collected by a detector for imaging. To prevent charging of non conducting specimen the sample is coated by Au or Pt.

In an atom to fill up the vacant k-shell from higher shells (L, M, N etc.) electrons are jumped into the k-shell and released energy by electromagnetic radiation which is basically X-ray. This is called characteristic X-ray which confirms the composition inside the sample. By determining this X-ray through a mode called Energy Dispersive X-ray (EDX) spectroscopy the compositional analysis also can be done in SEM. In all this process the sample is placed inside a high vacuum chamber (< 10^{-7} mbar).

In our thesis work we used SEM to image the nanowire samples, film thickness determination and compositional analysis by EDX spectroscopy. SEM also used to write pattern in electron beam lithography.

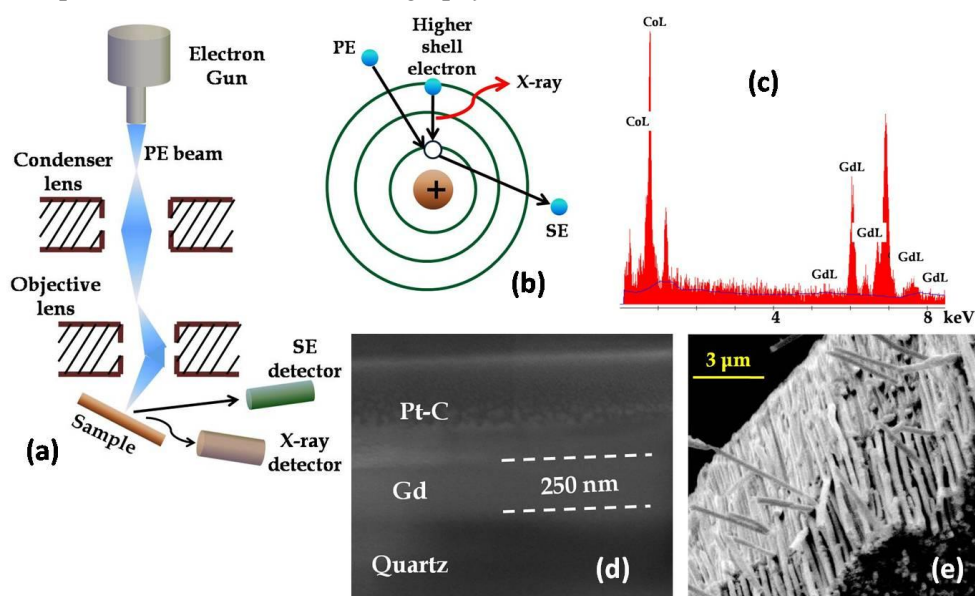


FIG. 2.12. (a) Schematic diagram of the mechanism of SEM. (b) Schematic diagram of SE and X-ray generation by PE from an atom. (c) EDX spectrum of GdCo alloy nanowire. (d) Cross sectional SEM image to find out the thickness of Gd film. (e) SEM image GdCo nanowire.

Transmission Electron Microscope (TEM):

In TEM the mechanism is nearly similar with SEM but the signal detection process and sample mounting has a difference. Here the PE beam has been generated by thermionic or field emission method and it has a maximum energy nearly or above 100 keV. The sample is prepared as a thin specimen or nanoparticle/nanowire which is placed on a thin carbon coated Cu grid. High energy electrons are transmitted through the sample and the transmission electrons (TE) are detected by a detector. In this system by adjusting the magnetic lenses from the electrons which have been done elastic scattering diffraction pattern can be generated. For thin single crystalline samples this produces a pattern of dots and rings for polycrystalline and amorphous samples. This result provides the information about the crystal structure of the sample. The EDX spectrum of the sample can also be generated in TEM.

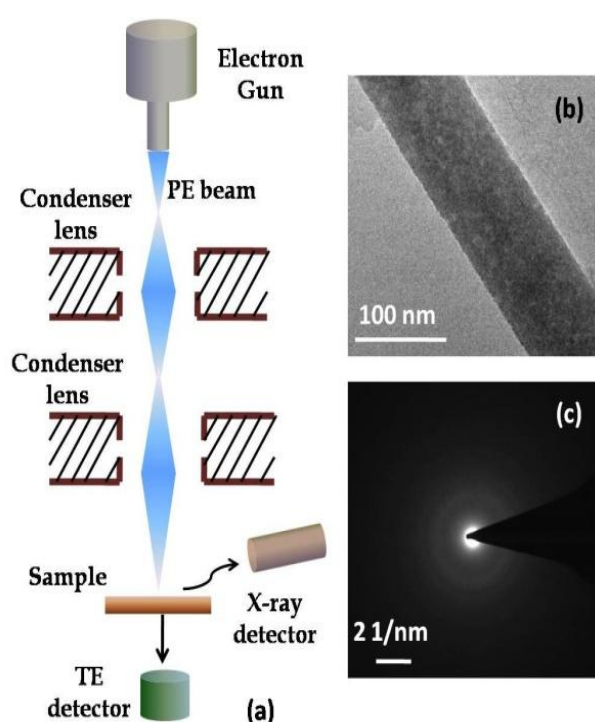


FIG. 2.13. (a) Schematic diagram of the mechanism of TEM. (b) TEM image of GdCo nanowire. (c) Selected Area Diffraction (SAD) of GdCo

In our thesis work we used TEM to image ~ 100 nm diameter GdCo nanowire. To understand the crystal structure we also determined the Selected Area Diffraction (SAD) pattern of that nanowire sample. Due to the wave like nature of electron when it passes through a crystalline sample, it behaves that it passes through a 3-dimensional grating and it is diffracted.

2.3. Physical measurements**2.3.1. Magnetization measurement****(a) Vibrating sample magnetometer (VSM)**

The magnetization (M) measurement with respect to the applied field (H) and temperature (T) can be measured very well by Vibrating sample magnetometer (VSM). The working principle of VSM is based on the Faraday law of induction. Here the sample is vibrated inside a fixed magnetic field using a

drive that moves the sample in a sinusoidal motion and an AC voltage is induced across the pickup coil. Induced voltage, $V_{ind} = -\partial\phi/\partial t$. The magnetic flux across the pickup coil is ϕ . This voltage is detected by a Lock in amplifier and from that voltage M is also calculated [7]. The uniform magnetic field around the sample is produced by a Helmholtz coil. The resolution of VSM is 10^{-6} emu.

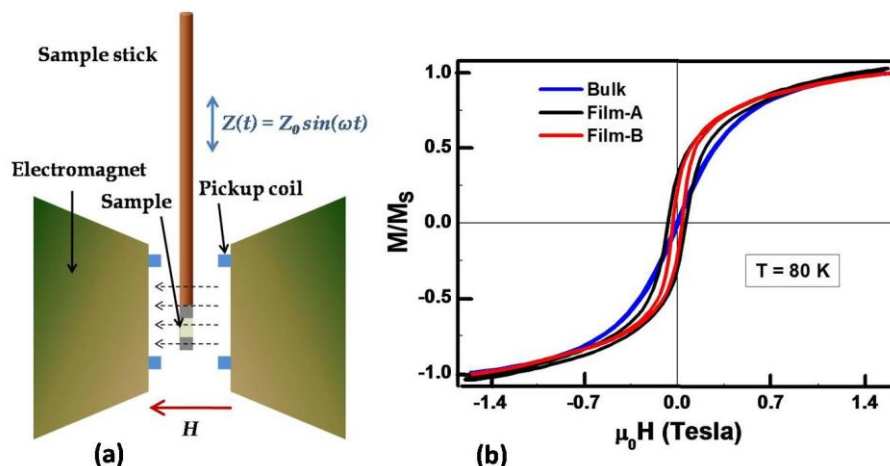


FIG. 2.14. (a) Schematic diagram of the VSM. (b) $M - H$ loop of Gd samples at 80 K. The magnetization is normalized by M_s (M at 1.6 T). The samples are bulk ingot (Bulk) and two films of grain size 105 nm (Film-A), 35 nm (Film-B).

Here we used a commercial VSM which has a temperature range from 80 K to 1250 K and field range up to 1.6 T. We measured H dependent magnetization curve or $M - H$ loop of our samples at different temperatures. In this thesis we also used VSM to measure the field cooled (FC) and zero field cooled (ZFC) temperature dependent magnetization of the samples. FIG. 2.14(b) shows that the coercive field H_c of the small grained Gd sample is larger than the bulk sample.

(b) SQUID magnetometer

Superconducting quantum interference device or SQUID is an ultra sensitive magnetometer with a resolution of 10^{-8} emu. The basic principal of SQUID is based on superconducting loops containing Josephson junctions. There are two kinds of SQUID which are DC and RF SQUID. DC SQUID is more sensitive than RF SQUID. Today it is used in various magnetic characterizations. AC susceptibility can also be performed in SQUID. Since here superconducting magnet is used, the range of maximum applied field is very high (> 5 T).

In this thesis by this magnetometer we measured $M - H$ loop of Gd samples at low temperatures (10–20 K). The FC and ZFC curve also measured within a temperature range 5–330 K at a magnetic field of 0.01 T. Result showed that the Gd samples are ferromagnetic with T_c around 300 K or room temperature. The samples (especially small grained film samples) also showed a low temperature transition around 20 K (FIG. 2.15).

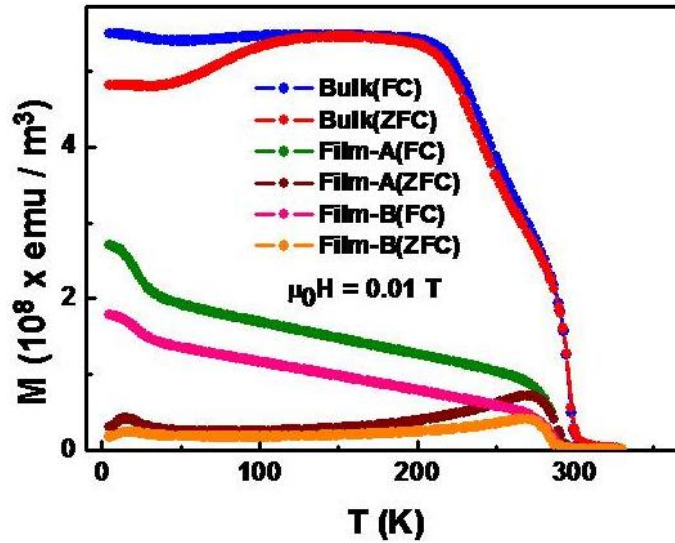


FIG. 2.15. FC and ZFC curve of Gd samples at a field 0.01 T. The samples are bulk ingot (Bulk) and two films of grain size 105 nm (Film-A), 35 nm (Film-B).

The AC susceptibility of that samples were measured using mutual inductance bridge in three different frequencies (17, 170 and 1202 Hz) of AC field (0.4 mT) and in the presence of three different DC bias fields (0, 0.01 and 0.1 T). The low temperature transition is clearly observed in AC susceptibility result (see FIG. 5.6).

2.3.2. Electrical resistance measurement

All electrical resistance measurements have been done using collinear four probe method. We used a high-precision resistance measurement using a low frequency AC technique with a Lock-in amplifier SR 830 (LIA) and a low noise transformer pre-amplifier (PA) with a gain of 100. Four electrical contact pads were collinearly connected with the samples. The outer side pads were for current leads (+I, -I) and the inner side pads were for voltage leads (+V, -V). An AC current I_{ac} was generated by LIA and was passed through a high resistance R_H (more than 100 times from the sample resistance) to maintain a constant AC current inside the circuit. Due to the passing of I_{ac} through the sample an AC voltage V_{ac} was developed across the voltage pads. This V_{ac} was then amplifies by a transformer preamplifier (PA) (only for small resistance sample) and detected again by the same LIA. To find the actual value of I_{ac} the voltage V_R across R_H was measured by another LIA or by a digital multimeter (DMM). Both the LIAs were synchronized with each other. The AC current was defined as $I_{ac} = V_R/R_H$. Where V_R was the amplitude of the AC voltage developed across R_H . The sample resistance R was defined as $R = V_{ac}/I_{ac}$. Here also V_{ac} was the amplitude of the AC voltage across the sample voltage leads +V and -V. For phase sensitive detection technique a frequency of 173 Hz was used.

From the measured resistance R , the resistivity of the sample was defined by $\rho = RA/L$. Where A was the cross sectional area of the sample. L was the distance between +V and -V pads on the sample.

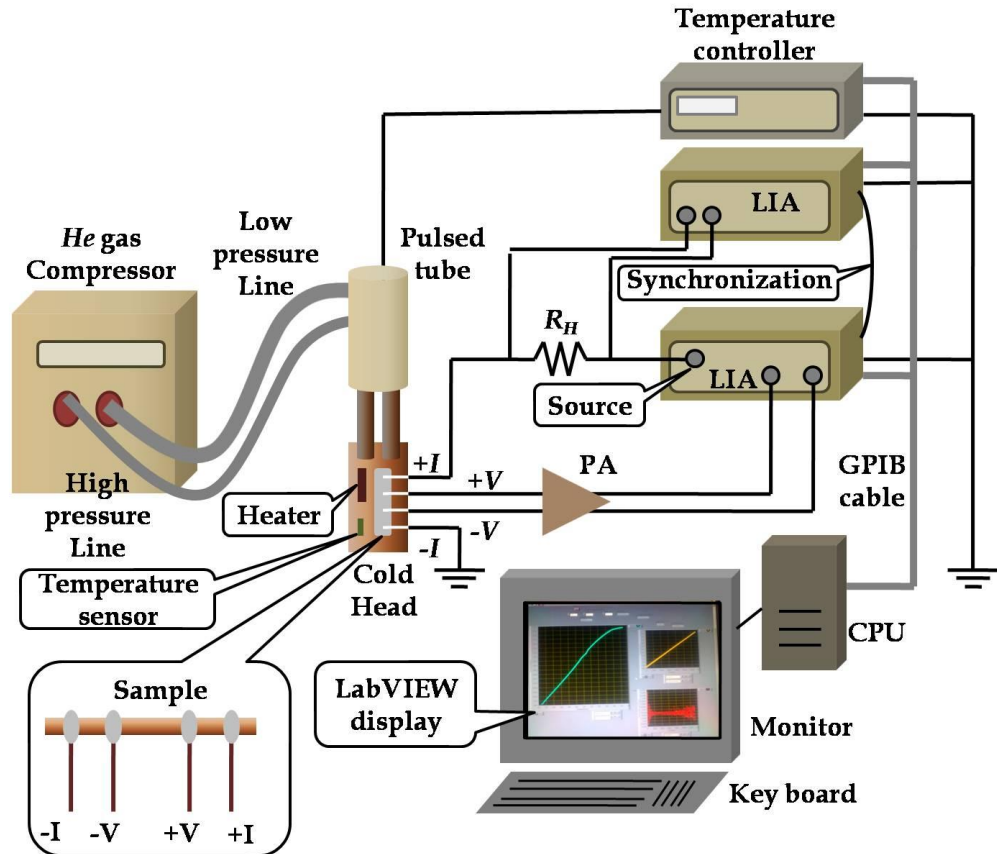


FIG. 2.16. Schematic diagram of low temperature AC resistance measurement technique. LIA = Lock-in amplifier, PA = Transformer Preamplifier.

A pulsed tube Helium cryostat [8, 9] was used for measurement in the temperature range of 4 K–330K. This type of cryostat does not have any moving part and therefore it has a noise free operation which helps us to measure very low resistance. The sample was mounted at the cold head where a heater and a Cernox thermometer were also attached. By sensing the temperature through the thermometer the heater was controlled by a temperature controller ITC 503. Cu wires were used for current and voltage measurements. The wires were connected with the contact pads of the sample by Silver paste. The experiment was automated by computer programming through the GPIB cables which were connected to the instruments. The computer programme has been written in LabVIEW software.

2.3.3. Magnetoresistance (MR) measurement

The change of electrical resistance of a sample due to the application of a magnetic field is called the magnetoresistance (MR). It can be defined as,

$$MR\% = \frac{R(H=0) - R(H)}{R(H=0)} \times 100 \quad (2.3)$$

, where $R(H=0)$ is the resistance at zero magnetic field $H=0$ and $R(H)$ is the resistance at a magnetic field H . The MR measurement can be done in two ways, one by temperature ramping and another one is isothermal MR measurement. Since the MR%

of our Gd samples is small enough ($\sim 1\%$ or less at a field 0.2 T) we used isothermal measurement technique.

(a) **Low field MR**

In case of the low field magnetoresistance (MR) measurement, a liquid nitrogen bath type cryostat with a copper wire air core solenoid was used. The measurement of MR was done up to a field of 0.2 T.

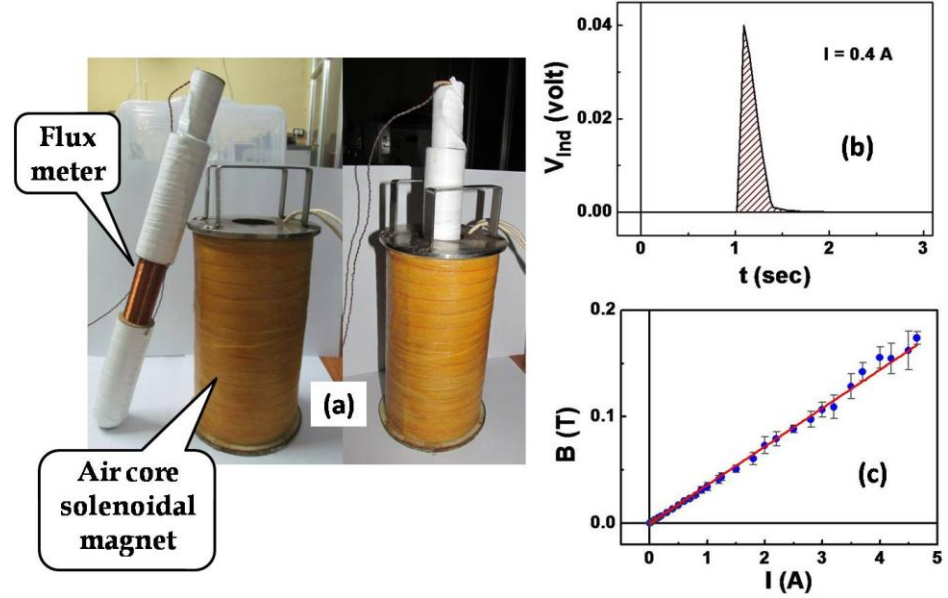


FIG. 2.17. (a) Flux meter and air core solenoidal magnet. (b) V_{ind} vs. t plot for a current 0.4 A. (c) I dependent B curve.

The magnet was calibrated by a flux meter. The flux meter was nothing just a solenoid which was connected with a digital multimeter (DMM). It was placed inside the air core solenoid magnet and the overall system was put inside a liquid nitrogen bath. The working principal of the flux meter follows Faraday Laws of induction.

$$V_{ind} = -\frac{\partial\phi}{\partial t} = -NA\frac{\partial B}{\partial t} \quad (2.4)$$

$$B = -\frac{1}{NA} \int_0^T V_{ind} dt \quad (2.5)$$

, where ϕ is the magnetic flux which is created due to the magnetic induction B of the magnet. N is the number of turns of the copper wire on the flux meter. V_{ind} is the induced voltage across the flux meter. When a DC current I was suddenly passed through the magnet a time dependent magnetic field $B(t)$ was generated and increases with time. Due to the change of magnetic field a voltage was induced across the flux meter. The experimental time was T . Therefore the area under the curve $V_{ind}-t$ shows the value of magnetic induction B for the current I . B was different for different values of I and from the $B-I$ curve the calibrated relation was established as $B = 0.036 \times I$.

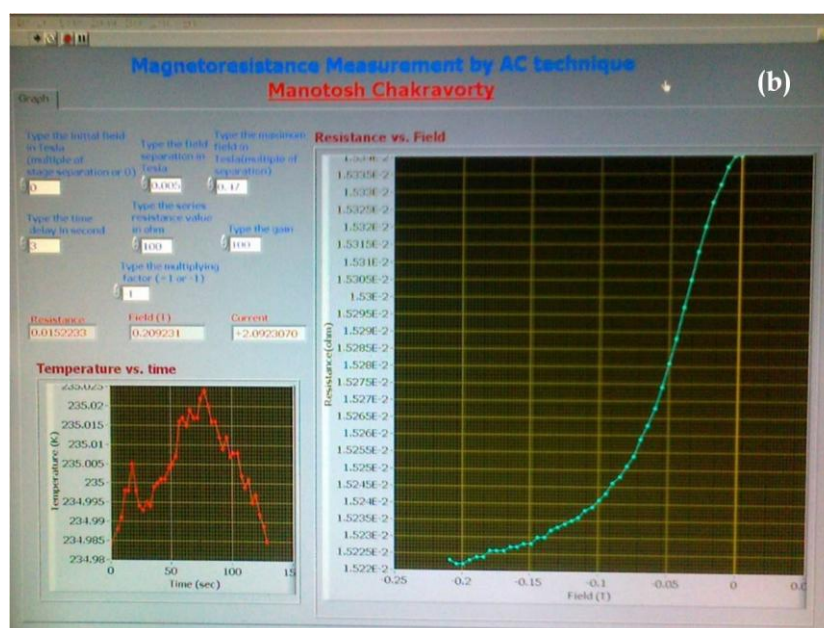
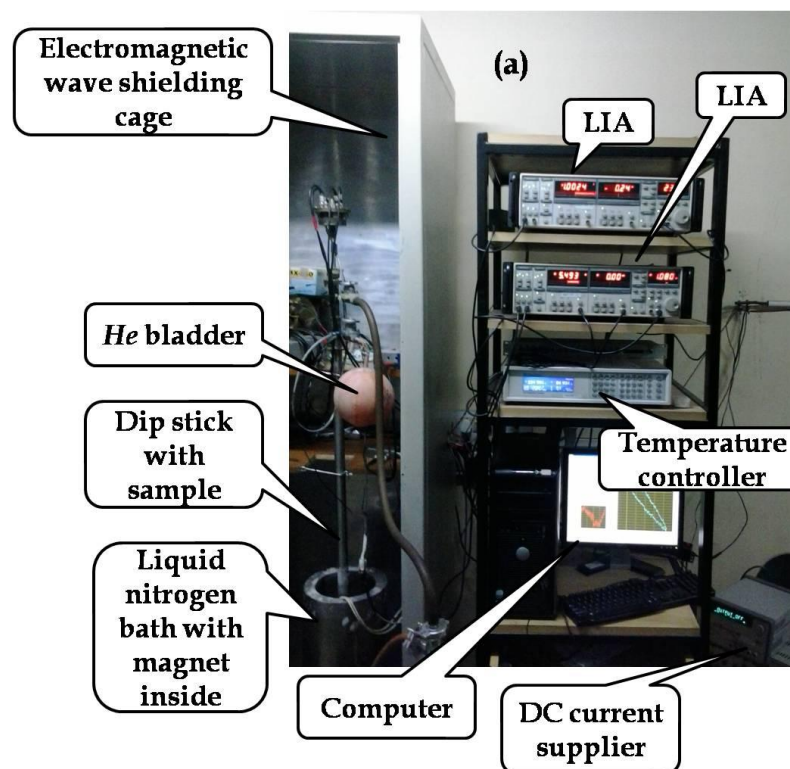


FIG. 2.18. (a) Setup for measuring the low field MR. (b) Screenshot of the MR measurement program in LabVIEW during the measurement of the MR of Gd bulk sample at 235 K.

The sample was mounted at the top end of a dip stick. Then the dip stick was poured inside a cylindrical vacuum chamber. The chamber with the stick was put inside an air core solenoidal magnet in such a way that the sample position was at the middle of the solenoid. Then the total system was put inside a liquid nitrogen bath. To protect the loss of liquid nitrogen the bath wall was made vacuum shielded.

To measure the resistance change of the sample, we used the AC low frequency resistance measurement technique which was rigorously discussed in the previous section. Here again we used two LIA, one PA and a high resistance which was connected in series with the circuit. The MR measurement has been done with a resolution of ± 1 ppm. To reduce the noise level the complete experiment has been done inside an electromagnetic wave shielded cage. DC power supply of Agilent was the source of a constant DC current which was passed through the magnet and create a constant magnetic field. A helium (He) bladder was attached with the chamber of dip stick. To reach the sample near liquid nitrogen temperature (< 90 K) He gas was passed inside the sample chamber to make good thermal contact. The desired temperature of the sample was controlled by a temperature controller of Lakeshore. The maximum temperature fluctuation during the experiment was ± 0.02 K. Pt100 was used as a temperature sensor. A heater was placed at the top end of the dip stick which was made by Nichrome wire. The instruments were connected with the computer by GPIB cables. All the experiments were controlled by computer programming which was written in LabVIEW software. This technique has been followed throughout the thesis work for all the samples to measure the low field MR.

(b) **High field MR**

The low temperature (below 80 K) and high field MR of the samples have been measured by a superconducting magnet up to a field of 9 T.

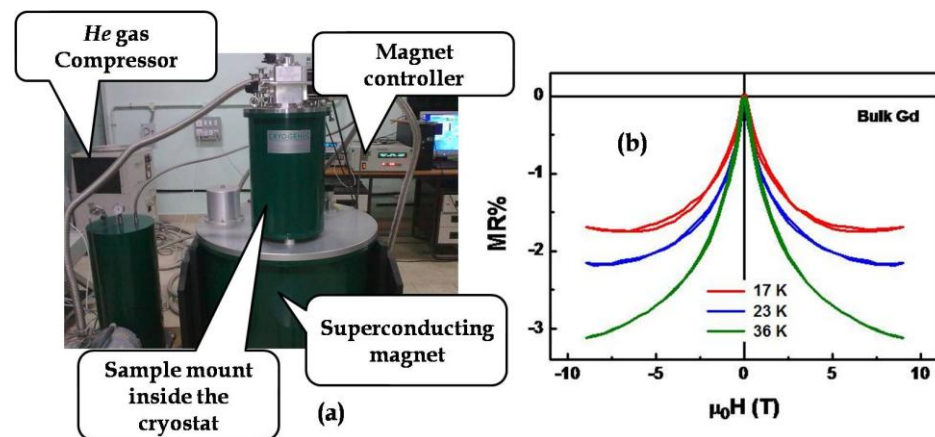


FIG. 2.19. (a) Setup for measuring the high field MR by a superconducting magnet. (b) Field dependent MR of bulk Gd sample.

The sample was mounted on the top of a sample stick which was then put inside a cryostat in such a way that the sample was at the middle of a solenoidal superconducting magnet. Here the wire of the solenoid was made by superconducting material. The sample temperature was cooled by a He gas compressor. By a heater and a temperature sensor which was put beside the sample a Lakeshore temperature controller controlled the temperature of the sample. The field range of the magnet was 0 – 10 T. The experiment has been done with a ramp rate of field 0.02 T/s. All the field dependent MR measurements have been isothermally done. The maximum temperature

fluctuation within a complete field ramp experiment was ± 0.07 K. The measurements have been done within a temperature range 15 – 40 K. The instruments were connected with the computer by GPIB cables and the data were automatically read by a C++ program.

References

1. Abdulabbas A. Hussain, *Journal of the Less Common Metals*, **72**, 71 (1980).
2. A. A. A. Hussain and T. S. Al-Bassam, *Thin Solid Films*, **59**, 77 (1979).
3. Thesis of M. Venkata Kamalakar, *Synthesis, Characterization and investigation of electrical transport in metal nanowires and nanotubes*, S. N. Bose National Centre for Basic Sciences, India (2009).
4. R. Kumar Pandey, S. N. Sahu, Suresh Chandra, *Handbook of Semiconductor Electrodeposition* (CRC Press, 1996).
5. PANanalytical B. V., Lelyweg 1, 7602 EA Almelo, Netherlands.
6. G. Binning, C. F. Quate and Ch. Gerber, *Phys. Rev. Let.*, **56**, 930 (1986).
7. K. H. J. Buschow and Frank R. Boer, *Physics of Magnetism and Magnetic Materials*, Springer (2003).
8. W. E. Gifford and R. C. Longworth, *Adv. Cryo. Eng.*, **3b**, 69 (1963).
9. 113 FALSE DRIVE, SYRACUSE, NEW YORK 13211 USA, <http://www.cryomech.com>

CHAPTER 3

Magnetoresistance of polycrystalline Gadolinium with varying grain size

In this chapter, we report a study of evolution of low field magnetoresistance (MR) of Gadolinium as the grain size in the sample is changed from few microns ($\sim 4 \mu\text{m}$) to the nanoscopic regime ($\sim 35 \text{ nm}$). The low field MR has a clear effect on varying grain size. In large grain sample (few μm), the magnetic domains are controlled by local anisotropy field determined mainly by the magnetocrystalline anisotropy. The low field MR clearly reflects the temperature dependence of the magnetocrystalline anisotropy. For decreasing gain size, the contribution of spin disorder at the grain boundary increases and enhances the local anisotropy field.

3.3.1. Introduction

In recent years, investigation of magnetism in Gadolinium (Gd), in particular, polycrystalline, and nanostructured Gd has attracted renewed attention [1-6]. The resurgence in the investigations on magnetic properties of Gd arises from the possibility of utilizing the rather high magnetic moment (and high saturation magnetization) in multilayer thin film applications [7] and also understanding basic physics in a metal with localized moments. Some of the recent magnetic studies focus on nanostructured samples with grain size in the domain of few tens of nm. The main motivation appears to be the fact that Gd is a new nanomagnetic system where the FM state arises from Gd ions with well-localized spin only moment in contrast to the magnetism in more itinerant conventional 3d ferromagnetic materials. Magnetoresistance (MR) of 3d ferromagnetic materials has been a well researched topic for many years and particularly in recent times; the application related issues have made it a very active field of research [8]. In comparison, however, investigation of the MR of 4f ferromagnetic metals like Gd has not attracted much attention. There are some classic reports of MR of Gd single crystals that show its essential differences with 3d metals (like Ni, Co, and Fe) [9,10]. These investigations, however, were done at a time when the spin structure of Gd was not well investigated and interesting features like spin reorientation (SR) transition were not discovered or well understood. The SR transition in Gd occurs at a well defined temperature $T_{SR} \sim 235\text{K}$ which is very unique because the magnetocrystalline anisotropy $\rightarrow 0$ at T_{SR} [11]. This feature is not seen in most (if not no other) ferromagnetic materials. Gd has a hexagonal closed pack (hcp) structure and ferromagnetic Currie temperature (T_C) = 292.77 K [12]. In Gd, the easy direction of magnetization makes an angle θ with the crystallographic c-axis. The angle θ changes with temperature in a complex manner because the magnetocrystalline anisotropy energy E_A (and the constants k 's) is strongly dependent on T [13]. A theory of the temperature dependence of the easy axis of magnetization in hcpGd has been proposed recently [14]. Gd, in addition to the para-ferro transition at T_C , has two other important temperatures related to the spin configurations, namely, the SR transition T_{SR} and the temperature T^* where θ becomes maximum. In samples with average grain size > 35 nm, the effect of magnetocrystalline anisotropy is expected to take predominance. Very recent neutron scattering studies [1] on nanocrystalline Gd powders found that while the angle θ in polycrystalline samples with large grains (size $(D) > \text{few } \mu\text{m}$) follows the temperature dependence as seen in single crystals, for samples with a characteristic grain size $(D_C) \leq 38$ nm, θ has a temperature independent value $\approx 50^\circ$. The similar result has been observed by the magnetization study of nanocrystalline Gd which clearly showed the roles of intra-grain and grain boundary (GB)/interfacial magnetic anisotropies [3].

The present investigation reports precision low field MR measurements in polycrystalline Gd with grain sizes varying from few microns down to few tens of nanometers. The MR experiments were carried out at low fields ($\mu_0 H \leq 0.2$ T), so that contributions to MR by the magnetic domains can be seen. The primary motivation is to study the effect of size reduction on such phenomena like spin reorientation transition and magnetic anisotropy as revealed through low field magnetotransport. Also, this work shows how the contribution to MR from domain wall and magnetic spins change with varying grain sizes.

3.2. Sample preparation

The measurements are done on polycrystalline samples of Gd with purity $\approx 99.9\%$. Three samples were studied in detail (see Table 3.1). One sample is a bulk polycrystalline sample ("Bulk"). The Bulk sample (length = 2.2 mm, width = 0.67 mm, and thickness = 0.25 mm)

was annealed at 850 °C for 24 h in 1 mbar of Ar and then cooled down to room temperature with a slow cooling rate ~ 1.5 K/min. Other two samples are films of thickness 1900 nm (Film-A) and 250 nm (Film-B) (see FIG. 3.1).

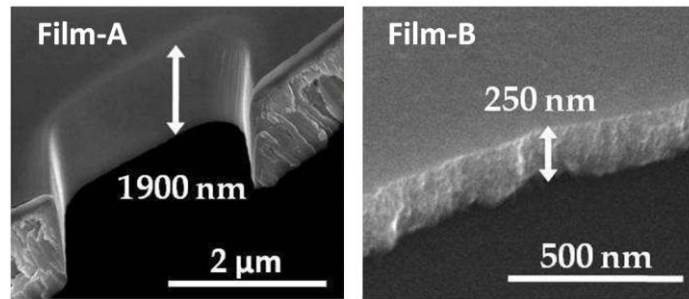


FIG. 3.1. Cross sectional SEM images of the films.

The films were made from the same starting ingot as the Bulk sample. They were made by evaporation in a turbo-pumped chamber at a base pressure of better than 10^{-7} mbar on Quartz substrates at temperature of 450 °C. The thickness of the film was controlled by varying the time of evaporation. After deposition, the films were annealed at temperature 500 °C in 1 mbar of continuous Ar flow. The Film-A annealed for 9 h, has larger grains compared to those of Film-B annealed for 4 h.

3.3. Characterization and measurement technique

3.3.1. Grain size analysis by AFM and SEM

The micro/nano-structures of the films were characterized by Atomic Force Microscope (AFM). Estimated grain morphologies and the grain sizes in the samples obtained from AFM are summarized in Table 3.1. For the bulk sample, grain sizes are calculated from the Scanning Electron Microscope (SEM) images and the average grain size is ≈ 4 μm (FIG. 3.2(a)).

Representative data for micro-structures of the two films are also shown in FIG. 3.2. There are clear differences in the grain morphologies as well as the average grain sizes. Film-B is a compact collection of nearly spherical grains with average size ≈ 35 nm. This can be seen in the AFM image for Film-B (see FIG. 3.2(b)). In Film-A, the average grain size is much larger with compact collection of long grains with average aspect ratio ~ 1.58 (see FIG. 3.2(b)). The AFM images taken on the surface show long grains where the average length and diameters are $d_L \approx 128$ nm and $d_w \approx 81$ nm. Now if we consider the grains are spherical, the mean grain size becomes $\sim (d_L + d_w)/2 \approx 105$ nm. The mean grain sizes were found by the fitting of Log-normal function with the grain size distribution (see FIG. 3.1(c)). Log-normal distribution is:

$$f(X) = A \exp \left[-\frac{(\ln X - \ln X_m)^2}{2\sigma^2} \right] \quad (3.1)$$

, where A is a constant, σ is the standard deviation and X_m is the mean value of X or grain size.

The three samples studied have distinctly different micro/nanostructures, grain morphologies with average grain sizes that differ by nearly one order in each of the samples. We will see later that these differences in micro/nanostructures have qualitative impacts on the low field MR.

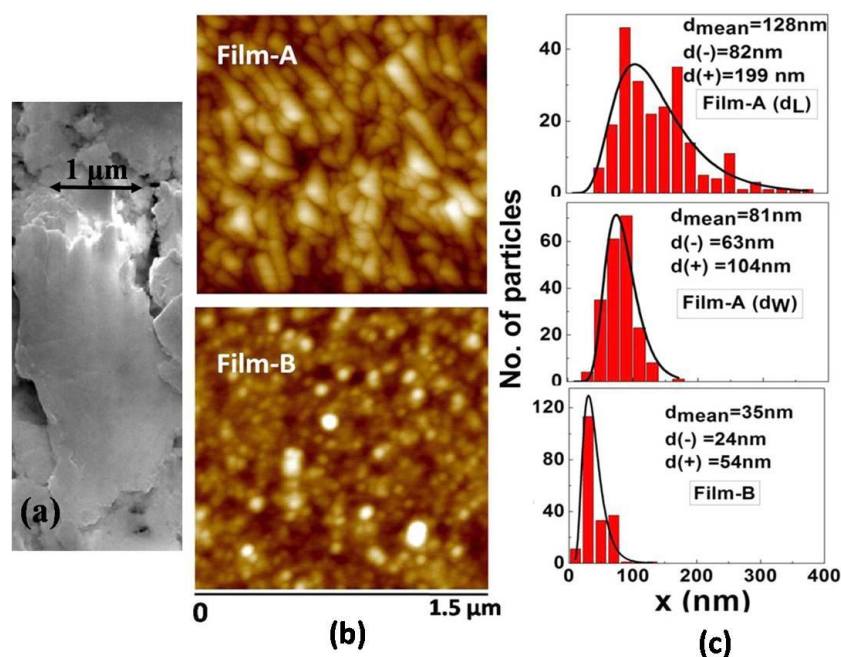


FIG. 3.2. (a) SEM image of crystallites of the Bulk sample. (b) AFM images of the films. The scale of AFM images is 1.5 μm. (c) Particle size distributions of Film-A and Film-B. In Film-A, the length and width of a crystallographic grain are denoted by (d_L) and (d_W), where $d(+)$ and $d(-)$ indicate the limits of distribution as obtained from histogram.

3.3.2. Crystal structure analysis by XRD

FIG. 3.3(a) shows the XRD pattern of the three samples. Data has been compared with the standard polycrystalline Gd powder pattern (ICDD data base, Ref. code: 00-002-0864).

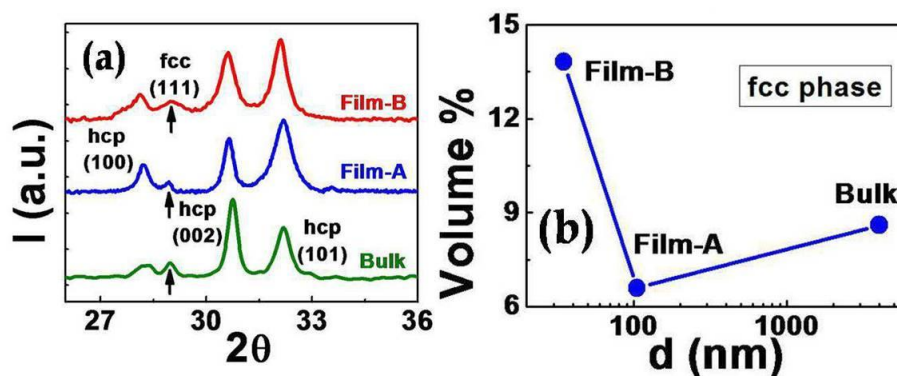


FIG. 3.3. (a) XRD data of three different samples. fcc phase is indicated by arrows. (b) Grain size (d) dependent fcc phase volume% of the samples.

Thin film growth generally favours the perpendicular direction and grains are columnar near the substrate surface [15] but due to the large thickness of the films (250 nm and 1900 nm), at the surface of the films grains are lying laterally. This may be the reason of maximum majority of the basal plane (101) hcp face which in contrast with the Bulk where the majority phase is c-axis (002) hcp face. All three samples have a finite (111) fcc phase. To find out the volume fraction of each phase the peaks were fitted by the Gaussian function and the area ($A(\text{face})$) under the curves were calculated for every

XRD peaks. Therefore the volume fraction can be expressed as $\text{Volume \%} = 100 \times [A(\text{face})/A(\text{total})]$, where $A(\text{total}) = A(100) + A(111) + A(002) + A(101)$. FIG. 3(b) shows the Volume % of fcc (111) phase for different samples (Film-B, Film-A and Bulk) of different grain sizes (35 nm, 105 nm and 4 μm). Previous reports [15,16] showed that the fcc phase only present in the seed layer of a thin film sample which has a finite thickness and this thickness decreases with the increase of film thickness. This is the reason of lower value of fcc Volume % in Film-A (thick film) (~ 6 %) than Film-B (~ 14 %). Though there is not any seed layer the amount of fcc phase is greater in Bulk (~ 8 %) than Film-A. This implies that the fcc phase which is present in the defect regions may increases due to the annealing at large temperature (~850 $^{\circ}\text{C}$). The fcc phase is paramagnetic or it has a small amount of constant magnetization throughout the hcp ferromagnetic region. Therefore our magnetic results are in-affected by this fcc phase. Determination of the fcc phase fraction was done using methods described in earlier publications [17].

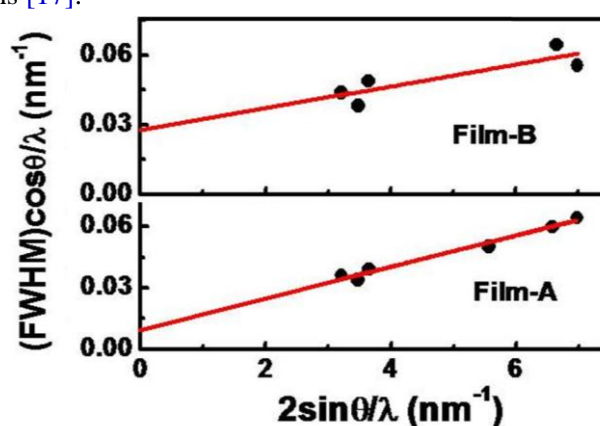


FIG. 3.4. Williamson Hall plot of the Film samples.

The particle size of the film samples was calculated from the XRD data. Here we used the method called Williamson Hall plot [18] that can use for the samples of grain size in the nanometer range ($\lesssim 100$ nm). The Full width half maximum (FWHM) of the XRD peaks are related with the particle size (d) and micro strain (ϵ) of the system as,

$$\frac{(FWHM)\cos\theta}{\lambda} = \frac{1}{d} + \epsilon \frac{2\sin\theta}{\lambda} \quad (3.2)$$

, where $\lambda = 0.1518$ nm is the wave length of Cu $K\alpha$ and θ is the XRD peak angle. By plotting $(FWHM)\cos\theta/\lambda$ vs. $2\sin\theta/\lambda$ and fitting Eqn. 3.2 from the intercept at y-axis we found the value of d for three different samples (see FIG. 3.4).

Table 3.1. Comparison of the d of film samples finding from different methods.

Sample	d (nm)	
	AFM imaging	Williamson Hall plot
Film-A	105	100
Film-B	35	37

Both the method shows nearly same value of particle size for the film samples (see Table 3.1).

3.3.3. Electrical measurements

All electrical measurements (including the MR measurements) have been done using collinear four probe method. Since the MR in these materials is $\sim 1\%$ or even less. We used a high-precision resistance measurement technique. The resistance and low field MR measurement techniques are described at the sections 2.3.2 and 2.3.3(a).

For MR measurements, the sample was cooled down from 330 K ($> T_C$) to a particular value of T where the data need to be taken. Then the magnetic field is applied from zero value and cycled following the sequence $0 \text{ T} \rightarrow 0.2 \text{ T} \rightarrow -0.2 \text{ T} \rightarrow 0 \text{ T}$. During the complete magnetic cycle, the temperature was fixed at the desired value to within 20 mK. After measuring a complete cycle, the sample was heated up again to 330 K (greater than T_C). It was then cooled again for a fresh field cycling data at another set of temperature. This ensures that the sample is demagnetized before start of MR measurement and there is no history of the previous magnetic field. Magnetic field was applied in plane of the measuring current. Data were taken with H parallel to current ($H \parallel j$) or H perpendicular to current ($H \perp j$).

3.4. Resistance measurement and analysis

The residual resistivity (ρ_0) of the Bulk sample has a value of $\rho_0 = 10.5 \mu\Omega\text{.cm}$. This is a factor of 2 (3) more than the reported b-axis (c-axis) ρ_0 for single crystals [19]. In the films, the ρ_0 are large and they increase as the grain size is reduced. In Film-A, $\rho_0 = 68.8 \mu\Omega\text{.cm}$ and in Film-B, $\rho_0 = 110.8 \mu\Omega\text{.cm}$. Very large value of ρ_0 in Film-B arises from its rather small nanoscopic grains. In FIG. 3.5, we show the normalized temperature derivatives of the resistivity ($= \frac{1}{\rho_0} \frac{d\rho}{dT}$) as a function of T . For the bulk sample there is a clear change in slope of the $\frac{1}{\rho_0} \frac{d\rho}{dT}$ at T_C . This is similar to that observed in single crystal of Gd at T_C [20]. This is a hallmark of the critical scattering of electrons from the spin disorder that is seen in all ferromagnetic materials like Ni [21].

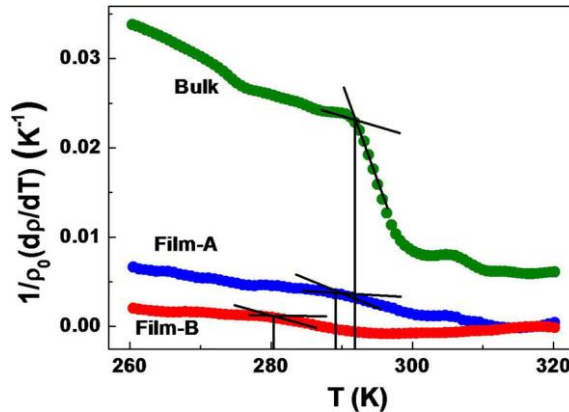


FIG. 3.5. Temperature dependence of the normalized derivative $\frac{1}{\rho_0} \frac{d\rho}{dT}$ in the vicinity of T_C for the three samples studied.

The T_C obtained by us from $\frac{1}{\rho_0} \frac{d\rho}{dT}$ of the Bulk matches with single crystals [19] to within 0.5 K. In Table 3.2, the value of T_C is compared with previous works. The clear feature in $\frac{1}{\rho_0} \frac{d\rho}{dT}$ of the bulk sample becomes progressively smeared out in Film-A and Film-B and there is a distinct shift of the temperature to lower value as the grain size decreases. This feature

matches with the previously observed work by Michels et al. [6] and Ferdinand et al. [22], where T_C decreases with the grain size. Due to the finite size effect, T_C decreases as the grain size decreases [23]. The critical scattering at T_C , although much smeared out persists in the films. It has been shown by our group that the critical scattering persists in ferromagnetic nanowires even when the diameter of the nanowire is reduced to nanoregime [24].

3.5. Magnetization measurement and analysis

The $M-H$ and $M-T$ curves serve as the two important magnetic characterizations for our samples. Collages of the important magnetic data in all the three samples are shown in FIG. 3.6. The left panel shows $M-H$ curves taken at different temperatures with the bulk data at the top and the Film-B data at bottom. The right panel shows the $M-T$ taken at a field of 0.01 T. The determination of T_C was done using modified Arrott plot [25,26] (see Appendix 2). The values of T_C are shown in Table 3.1. For bulk and Film-A, T_C values obtained from Arrott plots and the resistivity derivatives are close to within ± 1.3 K. On reduction of grain size, the T_C decreases, as has been found also from the resistivity derivative data. However, for Film-B, the T_C values obtained from both methods differ by ≈ 5.7 K. This difference principally arises due to the problem in locating T_C properly from the smeared out derivative in the nanostructured film.

Table 3.2. Comparison of T_C of the samples studied with previous works.

Experimental technique	Average grain size (μm)	Curie Temperature (T_C in K)	References
Resistivity derivative	4	292.5 (Bulk)	This work
	0.128(d_L), 0.081(d_W)	288.9 (Film-A)	This work
	0.035	280.8 (Film-B)	This work
Arrot plot [16]	4	291.4 (Bulk)	This work
	0.128(d_L), 0.081(d_W)	290.2 (Film-A)	This work
	0.035	286.5 (Film-B)	This work
Resistivity derivative	Single crystal	293.2	[19]
AC susceptibility	Single crystal	292.8	[12]
Calorimetric measurement	0.14	292	[6]
	0.024	284	
AC susceptibility	100	291.9	[22]
	0.025	285.6	
	0.0095	252.4	

The $M-T$ data of the bulk sample which was taken at low field (0.01 T) show that the FC and ZFC curves merge below $T \approx T_{SR}$. This feature in the $M-T$ curves that can be associated with the T_{SR} gets suppressed for $\mu_0 H > 0.1$ T. It is noted that the spin reorientation transition is the point where the magnetocrystalline anisotropy constants $\rightarrow 0$, as a result if the applied field is high, the spins will get aligned with applied field and features associated with the spin reorientation transition that depends on the intrinsic anisotropy field due to magnetocrystalline anisotropy, will not be visible. This is also corroborated by our MR measurements that have been done below 0.2 T which will be discussed later on in this chapter.

In the film samples, the $M-T$ curves taken in FC and ZFC conditions at low field ($< H_C$) differ at low T and the features associated with T_{SR} (unlike that in the bulk sample) are not seen. The manifestation of spin disorder is apparent in the films and it is accentuated in Film-

B. This corroborates recent magnetization data taken on polycrystalline and nanostructured samples that extensive spin disorder exists in the grain boundary that shows-up in the magnetization [2].

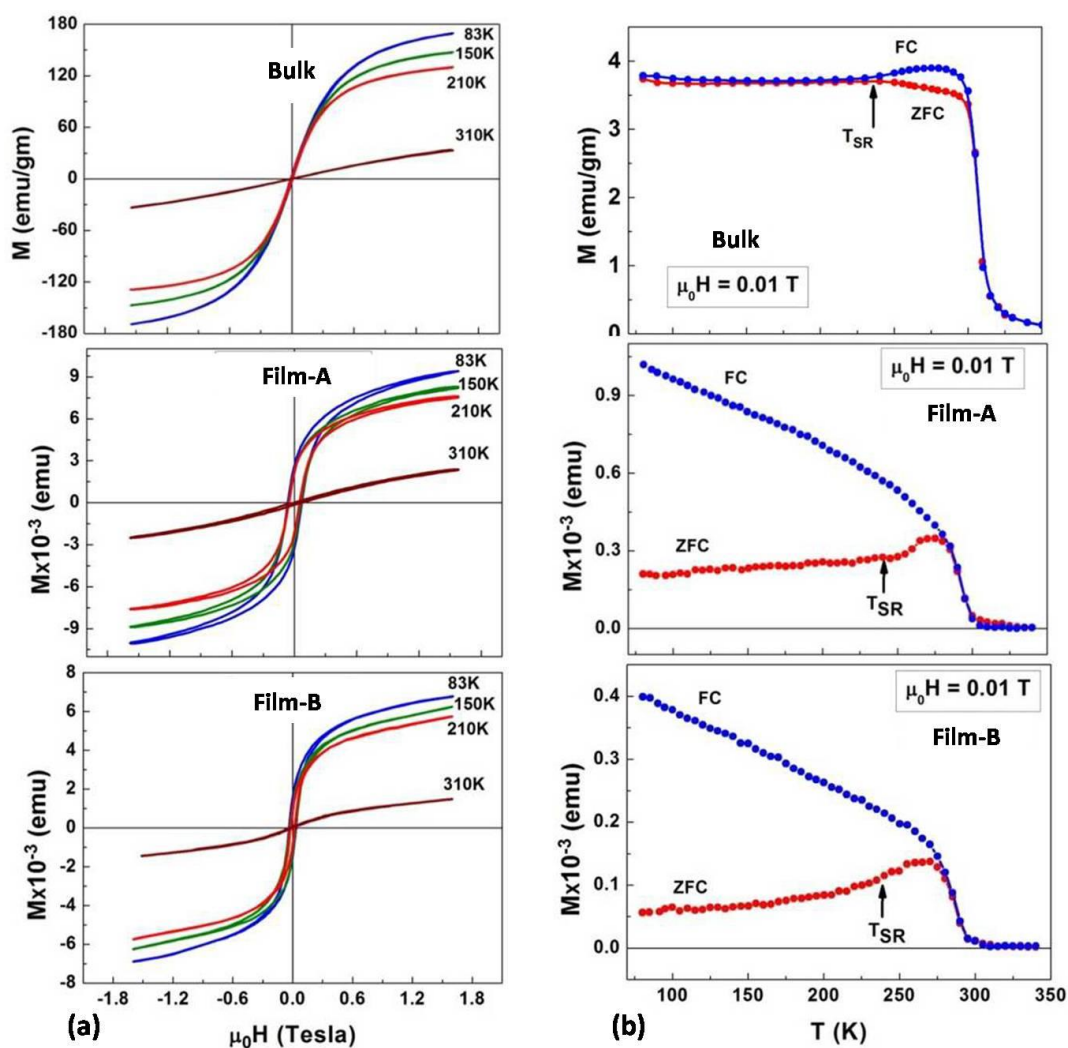


FIG. 3.6. The magnetization data of the three samples. (a) The left panel shows the $M - H$ data at different temperatures. (b) The right panel shows the $M - T$ data taken at a field of 0.01 T. Zero Field Cooled (ZFC) and Field Cooled (FC) data are shown, Due to uncertainty in film mass the magnetization data for the films have been shown in emu only.

The coercive fields H_C as a function of T obtained from the $M-H$ curves at different temperatures are shown in FIG. 3.7. For the bulk sample, the coercive field is low ($\mu_0 H_C < 5$ mT). In the $M-H$ curve, there is approach to technical saturation beyond 1 T, although there is clear sign of finite spin disorder even at high field.

The coercive field in the films are much larger, as expected in samples with reduced grain sizes that are expected to have spin disordered grain boundaries. H_C increases on cooling. The substantial hardening of the H_C strongly suggests enhancement of anisotropy energy or pinning potential for the magnetic domains. The H_C in the Film-A is somewhat larger than that in Film-B although the later one has smaller grain size. This is expected in many magnetic materials where the enhancement of H_C on size reduction gets reversed when the

size is reduced below the critical size for a single magnetic domain with coherent magnetization reversal [27]. The value of $\mu_0 H_C$ observed by us is of the same order but somewhat larger than that seen in other nanostructured Gd films [16]. The enhancement of the H_C on size reduction points to the fact that the intrinsic magnetocrystalline anisotropy no longer plays any dominant role.

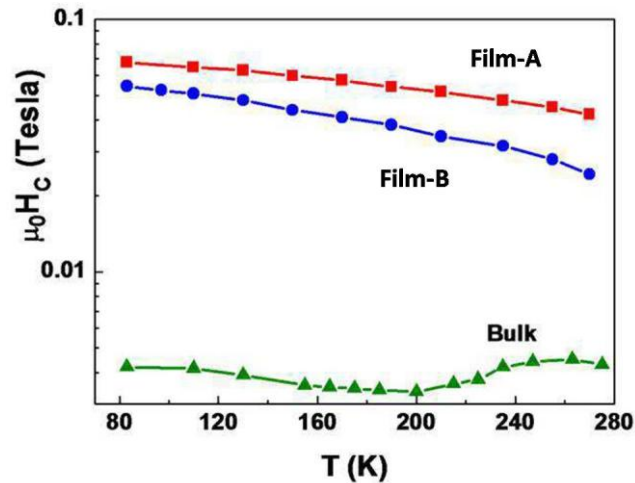


FIG. 3.7. The variation of the coercive field H_C as a function of T as obtained from the $M - H$ curves. (Note: The data for H_C are in log scale.)

Although MR measurements at low field is the principal aim of this investigation, the above detailed structural and microstructural, electrical resistivity and magnetization data were necessitated by the fact that in polycrystalline samples, unlike single crystal, the micro/nanostructures can vary from sample to sample and benchmarking the observed MR data would need these characterizations.

3.6. Magnetoresistance measurement and analysis

3.6.1. Temperature dependence

The MR (change of resistance due to applied field) $\Delta\rho$ ($=\rho(H) - \rho(H=0)$) as a function of T measured at field $\mu_0 H = 0.15$ T are shown in FIG. 3.8 for all the samples. Results are shown for field (H) parallel (\parallel) and perpendicular (\perp) to the measuring current (j) direction. In all the three samples the $\Delta\rho$ is negative (i.e., $\rho(H) < \rho(H=0)$). (Note that in FIG. 3.8, data are plotted as $-\Delta\rho$ to bring out the magnitude.) The qualitative differences in the $\Delta\rho$ data for the three samples are immediately apparent. For the Bulk sample, the magnitude of $\Delta\rho$ is comparatively larger and as the grain sizes become smaller the magnitude of $\Delta\rho$ is suppressed. The MR observed in the Bulk sample is comparable to that reported in the single crystal of Gd [28].

For the Bulk sample, the $|\Delta\rho_{\parallel}|$ (where $H \parallel j$) and $|\Delta\rho_{\perp}|$ (where $H \perp j$), both rise on cooling below T_C and show a very distinct and sharp peak at $T = T_{SR}$. $|\Delta\rho_{\parallel}|$ shows a distinct minimum at $T \approx 183$ K close to T^* . After the minima, it then rises again showing the broad maxima at $T \sim 125$ K and on further cooling $|\Delta\rho_{\parallel}|$ decreases. In case of $|\Delta\rho_{\perp}|$ there is no signature of T^* and below T_{SR} it decreases sharply with temperature. The prominent and sharp peak at T_{SR} is similar to that observed in the work of Hirakoa and Suzuki [29]. It is not, however, clear whether it is due to a phase transition type of behaviour at T_{SR} , where the magneto-crystalline anisotropy energy $\rightarrow 0$. Existence of

such a phase transition like behaviour has been suggested from recent magnetoimpedance measurement in strongly textured samples [4].

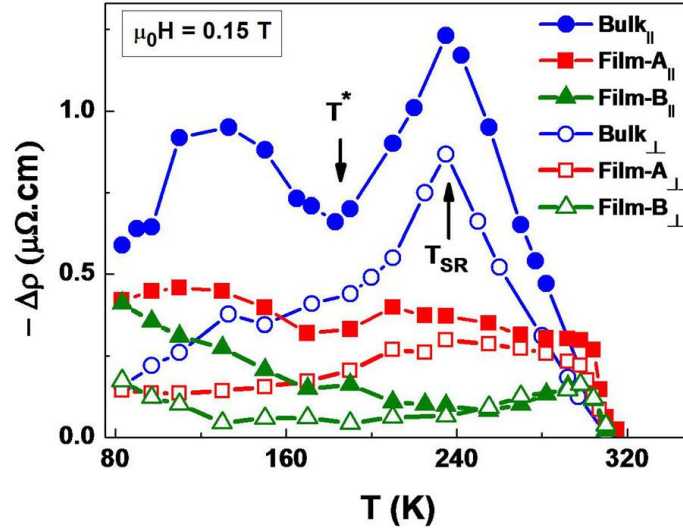


FIG. 3.8. Comparison of the resistivity change $-\Delta\rho$ (as a function of T) of three samples Bulk, Film-A and Film-B. Results are shown for both $H \parallel j$ and $H \perp j$ conditions with magnetic field $\mu_0 H = 0.15$ T. Transition temperatures (T_{SR} and T^*) are marked by arrows.

In Film-A, with intermediate grain size, these features at T_{SR} and T^* which have seen in the Bulk sample also persist to some extent, although much suppressed and appear at lower temperatures. The $|\Delta\rho_{||}|$ in low field shows the broad maxima at 210 K and shallow minima at ~ 165 K. On cooling to lower T , $|\Delta\rho_{||}|$ increases again. $|\Delta\rho_{\perp}|$ has a broad maximum around 210 K and below that temperature it decreases with decreasing temperature. For the nanostructured Film-B, $|\Delta\rho|$ rises sharply at and near T_C (like Film-A) but unlike other samples, the features seen at T_{SR} and T^* are absent. It establishes that in the nanostructured films with such small grain size, the magnetocrystalline anisotropy within a crystallographic grain is not the dominant factor (Note: For the existence of small but finite value of anisotropy energy [11], there is a finite value of $|\Delta\rho|$ above T_C that persists till 320 K.). The $|\Delta\rho|$ rises very sharply as T_C is approached from above. In the film samples the $|\Delta\rho|$ being small, the rise is more visible as T_C is approached. After the initial rise near T_C and a peak at T_C , $|\Delta\rho|$ monotonically decreases on cooling and reaches a small value till 250 K. Below that temperature $\Delta\rho_{||}$ and $\Delta\rho_{\perp}$ deviate from each other but both rise again somewhat as the sample is cooled further. At low temperatures, the rise in $|\Delta\rho|$ occurs due to enhancement of the magnetization on cooling. Due to the anisotropic magneto-resistance (AMR) and the Lorentz-MR contribution, the magnitude of $\Delta\rho_{\perp} < \Delta\rho_{||}$ for all the samples.

3.6.2. Field dependence

In FIG. 3.9, we show the field dependence of $\Delta\rho$ for $H \parallel j$ and $H \perp j$ conditions at four different temperatures. In the Bulk sample for $H \parallel j$ condition, below T_C , the field dependence of $\Delta\rho$ shows a clear two stage behaviour that develops below $0.9 T_C$.

There is a region of sharp rise in the magnitude of $\Delta\rho$ in a low field followed by an almost linear field dependent region at higher field. This sharp two stage behaviour

persists till $T \approx 150$ K. Below 150 K, it shows more gradual field dependence. The field dependence of $\Delta\rho$ does not show any hysteresis. The two stage behaviour, as we would discuss below, is related to the response of the magnetic domains to the applied field. In case of $H \perp j$ condition the two stage behaviour develops below $T \approx 190$ K. As the temperature decreases, $\Delta\rho$ becomes saturated for small values of $\mu_0 H$. The two stage behaviour is not seen in either of the films. The high value of coercive field (H_C) in the films leads to a clear hysteresis in $\Delta\rho$ under field cycling over certain temperature region. In both the films, at low T the butterfly pattern in $\Delta\rho$ vs. $\mu_0 H$ curve can be seen. For Film-B, the hysteresis effect becomes maximum with minimum values of $\Delta\rho$ at $T = 190$ K and $H \perp j$ condition.

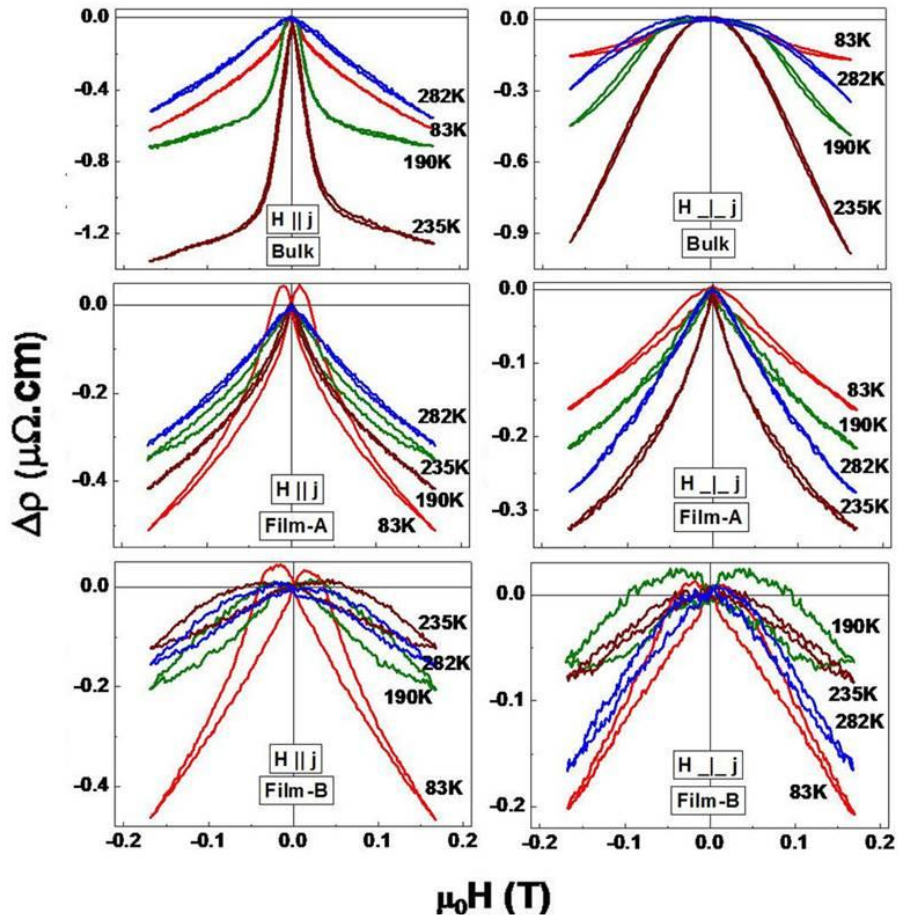


FIG. 3.9. Comparison of the resistivity change $\Delta\rho$ (as a function of H) of three samples Bulk, Film-A and Film-B. Results are shown for four different temperatures.

The two stage behaviour seen in the MR of the Bulk can be better observed in the field derivatives $\frac{d(\Delta\rho)}{d(\mu_0 H)}$ taken at different fields and at different temperatures. This is shown as a contour plot in FIG. 3.10. These plots show the differences in $\frac{d(\Delta\rho)}{d(\mu_0 H)}$ as a function of H and T in the three samples. With $H \parallel j$ condition it can be seen that the derivative has the largest magnitude in the Bulk and it is largest at $T \sim T_{SR}$ and at a very low field of ~ 0.01 T. In other temperature ranges, it tends to a low value and the derivative becomes smaller at higher field. This clearly establishes the two stage dependence of the $\Delta\rho$ on the field. For films the derivative has much smaller magnitudes, showing the

gradual dependence of the $\Delta\rho$ on the applied field. For $H \perp j$ the derivative behaves differently. The qualitatively different behaviours observed in the field dependences show that in the Bulk with large crystallographic grains (where the MR might mimic closely that seen in single crystal) the SR transition temperature has a clear presence in the low field MR. At higher fields its presence is much suppressed. This feature near T_{SR} is gradually suppressed in films as the grain boundary contributions win over those from the interior of the grain. It is completely absent in Film-B which has average grain size ~ 35 nm. In the following, we would discuss implications of some of the main results.

3.7. Discussion

The MR in this material is likely to have two major components

$$\Delta\rho = \Delta\rho_{domain} + \Delta\rho_{spin} \quad (4.3)$$

The first component $\Delta\rho_{domain}$ arises from the domains that are pinned at the GBs. In an applied field when the domain slips from the GB, its contribution to the resistance drops. The second component $\Delta\rho_{spin}$ is the component of MR that arises due to the reduction of spin fluctuations or the suppression of thermally excited magnons by an applied field. Temperature increment enhances the spin fluctuations [30]. The MR at low field is likely to be dominated by the first term provided, since the field needed to align domains is not very large. The MR at high field will be controlled by the suppression of thermally excited magnons [31] and $\Delta\rho_{spin}$ is going to be the dominant contributor. In the low field range of the present investigation the first component is likely to be the dominant controlling factor. As a rough model for $\Delta\rho_{domain}$ we could write

$$\Delta\rho_{domain} \propto N_d \delta \psi(\mu_0 H) \quad (4.4)$$

, where N_d is the number of domains within a crystallite that are pinned at the GB and slip from the pinning site in the applied field, δ is reduction of resistance when the domain slips. Again, $\psi(\mu_0 H) \equiv \int_0^{\mu_0 H} \phi(\epsilon) d\epsilon$, where $\phi(\epsilon)$ is the distribution function for the local field ϵ . The local field in this case represents a pinning field that pins the domains at the GB and can act as a local anisotropy field. The distribution function can have a most probable field H_A . For the low field region the field derivative $\frac{d(\Delta\rho)}{d(\mu_0 H)}$ is $\propto \phi(\epsilon)$.

The observation that the MR has different behaviours, particularly at low fields in the three samples, is a reflection of dominance of the domains in the low field MR, which evolve as the grain size changes. In bulk sample since $D \gg D_C$, the main contribution of $\Delta\rho$ is $\Delta\rho_{domain}$. $|\Delta\rho|$ shows a prominent peak at $T = T_{SR}$ (see FIG. 3.8) along with large peak in $\frac{d(\Delta\rho)}{d(\mu_0 H)}$ at low field. In bulk sample, with larger grains, the electron scattering will be mainly within the grain. The domain movement will be controlled by the local anisotropic field. When the field is applied ($> H_A$), the magnetic domains slip from the GB pinning sites and align to the field, reducing the resistance thus giving rise to a sharp low field MR. For $T < T_{SR}$, the magnetocrystalline anisotropy energy builds up and the magnitude of low field MR goes down. For $T > T_{SR}$ the MR goes down because the magnetization goes down when $T \rightarrow T_C$.

The sharp value of derivative $\frac{d(\Delta\rho)}{d(\mu_0 H)}$ observed for the bulk sample close to T_{SR} occurs at field which we call H_{max} . The value of H_{max} then can be connected to the maximum in the distribution of ϵ . In FIG. 3.11, we show the temperature dependence of H_{max} . The low value of H_{max} that is seen for $T \leq T_{SR}$ is thus a reflection of low value of H_A . In a recent investigation of magnetoimpedance in Gd, it has been shown that there is a small anisotropy

field ~ 0.015 T that is finite at low T and reduces to zero as $T \rightarrow T_{SR}$ [4]. This is similar to the value of H_{max} observed by us. Above T_{SR} for Bulk Gd, E_A has a finite value with a maximum at T_C [11] and the magnetization gradually decreases as T approaches to T_C . This causes the sharp rise of H_{max} for $T > T_{SR}$ (Since $E_A = \mu_0 H_{max} M_S / 2$, where M_S is the saturation magnetization [32]). The MR of Film-A has contributions from both (domains and spin disorder) and therefore the derivative $\frac{d(\Delta\rho)}{d(\mu_0 H)}$ shows a shallow maximum from which we can identify H_{max} as we did for the bulk sample. In Film-A, the value of the field H_{max} is larger. It shows a minimum at $T \simeq T_{SR}$ and then rises again as T_C is approached from below, like the bulk sample.

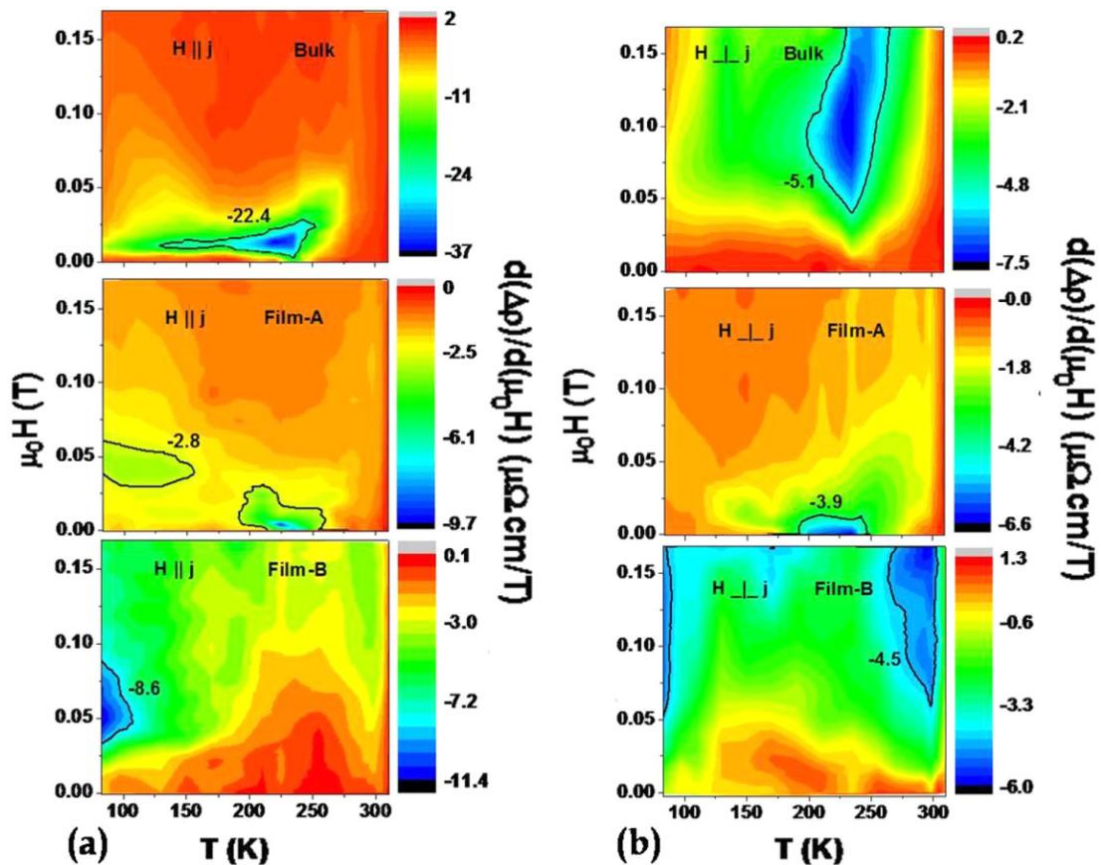


FIG. 3.10. Contour plot of $\frac{d(\Delta\rho)}{d(\mu_0 H)}$ as a function of $\mu_0 H$ and T for all three samples (Bulk, Film-A and Film-B). Columns (a) and (b) show $\frac{d(\Delta\rho)}{d(\mu_0 H)}$ for the conditions $H \parallel j$ and $H \perp j$.

In the films as the grain size becomes smaller, there is progressive increase of ϵ , arising mainly from the pinning of domains at the disordered surface of the grains. In that case, larger field will be needed to align the magnetic domains. The manifestation of the magnetocrystalline anisotropy energy is completely suppressed when the grain size (~ 35 nm) is comparable or less than the characteristic length D_C as in the Film-B.

At comparatively higher field ($\mu_0 H > 0.1$ T), the MR seems to reach a limiting behaviour. For all the samples at both the conditions ($H \parallel j$ and $H \perp j$), the derivative shows a nearly field independent value, $\frac{d(\Delta\rho)}{d(\mu_0 H)} \simeq 1$ to $-4 \mu\Omega \cdot \text{cm}/\text{T}$. In the region the applied field is more than the H_C . This is the region where domain alignment will not contribute and the

contribution will be from the spin or thermally excited magnons fluctuation term $\Delta\rho_{spin}$. In that case, the film grain structure may not play a dominant role, leading to similar behaviour in all the samples.

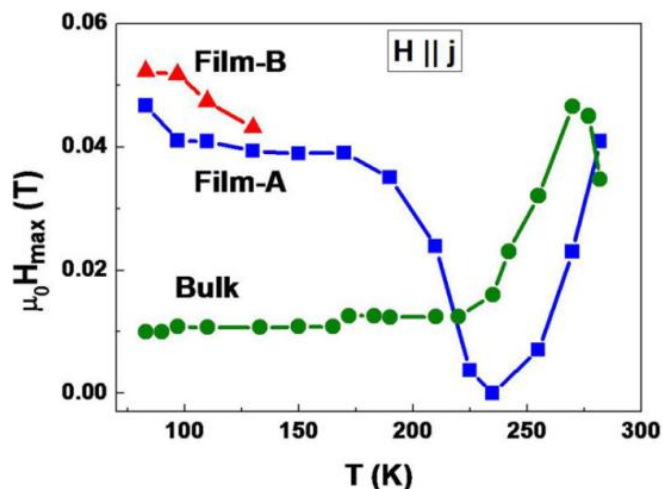


FIG. 3.11. Observed T dependence of the field H_{max} (where the field derivative $\frac{d(\Delta\rho)}{d(\mu_0 H)}$ shows a maximum).

A prominent manifestation of the magnetocrystalline anisotropy occurs in the anisotropic MR (AMR) in ferromagnetic metals and alloys. In the field region of our study, the MR is mainly controlled by the domain orientations. Thus, anisotropy arises from anisotropy in Fermi surface and the differences in the electron rates in the s - s scattering and s - f scattering may not be the leading contributor in the MR anisotropy in this case. The observed anisotropy may arise from local anisotropy fields that control domain dynamics. In the Bulk sample, the local anisotropy field will occur due to internal mechanism that will depend on the anisotropy constants. In the film samples, the domains being predominantly pinned in grain boundary regions (where local spin disorder plays role), the MR is mainly isotropic with small residual anisotropy. Thus, similar MR derivative were observed in Film-B for field parallel and perpendicular conditions (FIG. 3.10).

3.8. Conclusion

The present investigation is a comprehensive study of magnetoresistance done on polycrystalline samples of Gd with varying grain sizes. The magnetoresistance investigation was done in the low field region. The grain sizes range from few μm to few tens of nm. In the sample with grain sizes \sim few μm or more, the dominant effect arises from the magnetocrystalline anisotropy of Gd and the observed MR (its temperature dependence as well as its anisotropy) is a reflection of the temperature dependence of the intrinsic magnetocrystalline anisotropy. The most prominent feature is a sharp peak like feature of the magnitude of MR at the spin reorientation transition temperature. As the grain size decreases, the contribution of the grain boundary increases. The spin disorder at the grain boundaries and pinning by disorder become important. A larger pinning potential for the domains reduces the MR in the films. This suppresses the features associated with the intrinsic magnetocrystalline anisotropy. The evolution of the MR with grain size shows clear cross over from an intrinsic magnetocrystalline anisotropy dominated regime to a grain boundary spin disorder dominated regime.

References

1. D. H. Ryan, A. Michels, F. Döbrich, R. Birringer, Z. Yamani and J. M. Cadogan, *Phys. Rev. B*, **87**, 064408 (2013).
2. F. Döbrich, J. Kohlbrecher, M. Sharp, H. Eckerlebe, R. Birringer and A. Michels, *Phys. Rev. B*, **85**, 094411 (2012).
3. S. P. Mathew and S. N. Kaul, *J. Phys.: Condens. Matter*, **24**, 256008 (2012).
4. G. L. F. Fraga, P. Pureur and L. P. Cardoso, *J. Appl. Phys.*, **107**, 053909 (2010).
5. P. M. Shand, J. G. Bohnet, J. Goertzen, J. E. Shield, D. Schmitter, G. Shelburne and D. L. Leslie-Pelecky, *Phys. Rev. B*, **77**, 184415 (2008).
6. D. Michels, C. E. Krill III and R. Birringer, *J. Magn. Magn. Mater.*, **250**, 203 (2002).
7. C. Ward, G. Scheunert, W. R. Hendren, R. Hardeman and M. A. Gubbins, *Appl. Phys. Lett.*, **102**, 092403 (2013).
8. P. Grünberg, *Acta Mater.*, **48**, 239 (2000).
9. K. Maezawa, T. Mizushima, K. Mori, K. Sato, Y. Saito and S. Wakabayashi, *J. Phys. Soc. Jpn.*, **47**, 585 (1979).
10. K. A. Mcewen, G. D. Webber and L. W. Roeland, *Physica B*, **86**, 533(1977).
11. C. D. Graham, Jr., *J. Appl. Phys.*, **34**, 1341 (1963).
12. S. N. Kaul and S. Srinath, *Phys. Rev. B*, **62**, 1114 (2000).
13. W. D. Corner and B. K. Tanner, *J. Phys. C: Solid State Phys.*, **9**, 627(1975).
14. M. Colarieti-Tosti, T. Burkert, O. Eriksson, L. Nordström and M. S. S. Brooks, *Phys. Rev. B*, **72**, 094423 (2005).
15. G. Scheunert, C. Ward, W. R. Hendren, A. A. Lapicki, R. Hardeman, M. Mooney, M. Gubbins and R.M. Bowman, *J. Phys. D: Appl. Phys.*, **47**, 415005 (2014).
16. G. Scheunert, W. R. Hendren, C. Ward and R. M. Bowman, *Appl. Phys. Lett.*, **101**, 142407 (2012).
17. T. P. Bertelli, E. C. Passamani, C. Larica, V. P. Nascimento, A.Y. Takeuchi and M. S. Pessoa, *J. Appl. Phys.*, **117**, 203904 (2015).
18. G. K. Williamson and W. H. Hall, *Acta Metallurgica*, **1**, 22 (1953).
19. H. E. Nigh, S. Legvold, and F. H. Spedding, *Phys. Rev.*, **132**, 1092 (1963).
20. D. S. Simons and M. B. Salamon, *Phys. Rev. B*, **10**, 4680 (1974).
21. O. Källbäck, S. G. Humble and G. Malmström, *Phys. Rev. B*, **24**, 5214 (1981).
22. A. Ferdinand, A-C. Probst, A. Michels, R. Birringer and S. N. Kaul, *J. Phys.: Condens. Matter*, **26**, 056003 (2014).
23. M. E. Fisher and M. N. Barber, *Phys. Rev. Lett.*, **28**, 1516 (1972).
24. M. V. Kamalakar and A. K. Raychaudhuri, *Phys. Rev. B*, **82**, 195425 (2010).
25. Anthony Arrott, *Phys. Rev.*, **108**, 1394 (1957).
26. Anthony Arrott and John E. Noakes, *Phys. Rev. Lett.*, **19**, 786 (1967).
27. Gisela Herzer, *J. Magnetism and Magnetic Material*, **112**, 258 (1992).
28. J. A. M. Santos, J. F. Collingwood, J. B. Sousa and S. B. Palmer, *J. Magn. Magn. Mater.*, **272**, e491 (2004).
29. T. Hirakoa and M. Suzuki, *J. Phys. Soc. Jpn.*, **31**, 1361 (1971).
30. M. V. Kamalakar and A. K. Raychaudhuri, *Phys. Rev. B*, **79**, 205417 (2009).
31. S. N. Kaul and S. P. Mathew, *Phys. Rev. Lett.*, **106**, 247204 (2011).
32. *Physics of Ferromagnetism*, 2nd ed., edited by S. Chikazumi (Oxford University Press, 1999).

CHAPTER 4

Low field magnetoresistance of Gadolinium nanowire

In this chapter we report low field ($\mu_0 H < 0.2$ T) magnetoresistance (MR) studies on a single Gd nanowire patterned from a nano-structured film (average grain size ~ 35 nm) by focused ion beam. For comparison, we did similar MR measurements on a polycrystalline sample with large crystallographic grains (~ 4 μm). It is observed that in the low field region where the MR is due to motion of magnetic domains, the MR in the large grained sample shows a close relation to the characteristic temperature dependent magnetocrystalline anisotropy including a sharp rise in MR at the spin reorientation transition at 235 K. In stark contrast, in the nanowire, the MR shows complete suppression of the above behaviours and it shows predominance of the grain boundary and spin disorder controlling the domain response.

4.1. Introduction

As we discussed in the previous chapters that the magnetism in Gd is fast re-emerging as an actively researched area [1,2]. The magnetism, spin structure, and magnetocrystalline anisotropy in Gd (a 4f metal) is qualitatively different from those found in more conventional ferromagnetic 3d metals like Fe, Co, and Ni. Recent Small Angle Neutron Scattering (SANS) studies have established that in Gd below an average grain size of 35 nm, the spin disorder at the grain boundaries plays an important role [1,2].

The present investigation approaches the problem from the view point of magnetotransport, which we show below can change qualitatively when the size is reduced to nano-metric range. This work specifically investigates what happens to the weak magnetocrystalline anisotropy on size reduction as they are reflected in low field magnetoresistance (MR), where it is governed by response of magnetic domains to an applied field. We show that the low field MR reflects a change from a magnetocrystalline anisotropy dominated behaviour to a disorder dominated behaviour as the grain size is reduced to a length scale of few tens of nm. We note that while transport and magnetotransport in single crystalline Gd have been reported extensively [3], there are no reports of magnetotransport measurements in nano-structured Gd, particularly in nanowire. Here low field MR of Gd nanowire has been studied rigorously and the results were compared with its bulk counterpart.

4.2. Sample preparation and characterization

The measurements were done on two samples of Gadolinium (Gd). Sample S-1 is a polycrystalline annealed ingot (dimensions in mm range), which served as a reference sample which to some extent mimics a single crystal in the MR due to its rather large grain size. Sample S-2 is a nanowire of width ≈ 275 nm and length ≈ 10 μm . The nanowire was fabricated by nano-patterning a Gd film of thickness 250 nm using Focused Ion Beam (FIB) with 30 keV Ga^+ ions. The starting film was grown by physical vapour deposition on quartz substrate. The bulk polycrystalline sample (S-1) was annealed in 1 mbar Ar at 850 $^{\circ}\text{C}$ for 24 h and subsequently cooled slowly to room temperature. Sample S-2 was annealed for 4 h in Ar after deposition. Both the samples were made from the same starting batch of Gd with 99.9% purity.

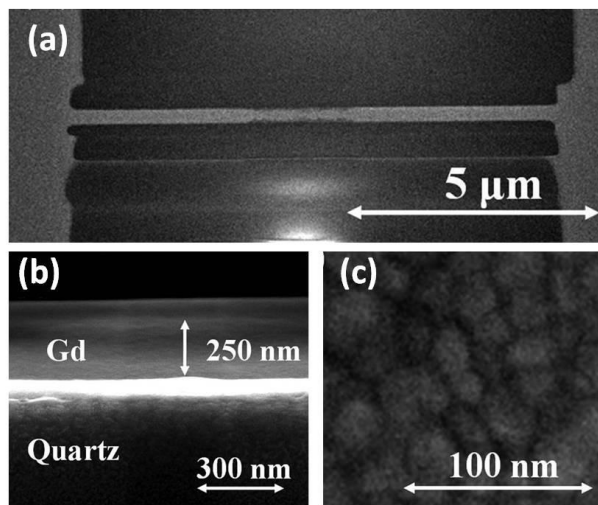


FIG. 4.1. (a) Image (top view) of the nanowire of width ~ 275 nm made by FIB (sample S-2). (b) Cross-sectional SEM image of the nanowire on the Quartz substrate. (c) SEM images of the top surface of the film showing grain structure (before the nanowire was fabricated).

The structures of the samples were determined by X-Ray diffraction (XRD) and the data (FIG. 3.3(a)) were indexed into hcp structure of Gd. The micro/nano-structures of the samples were studied using Scanning Electron Microscope (SEM), Cross-sectional SEM, and Atomic Force Microscope (AFM). For sample S-1, the average grain size is $\approx 4 \mu\text{m}$, as observed from SEM micrograph (shown in FIG. 3.2(a)). Sample S-2 is nano-structured nanowire (see FIG. 4.1(a)). It contains a compact collection of nearly spherical grains with average size $\approx 35\text{nm}$ (FIG. 4.1(b)), which extends across the cross-section of the film as can be seen from FIG. 4.1(c).

4.3. Electrical resistance and MR measurement techniques

All electrical measurements were made in a homemade variable temperature cryostat with liquid nitrogen bath. High-precision resistance and MR measurement processes which are described elaborately in chapter-2 are followed here. The resistance of the samples has been measured by four probe method. We used a low measuring current ($\leq 10 \text{ mA}$) to avoid Joule heating. The Lock in amplifier (LIA), Digital multimeter (DMM), transformer preamplifier (PA) and a high resistance R_H ($\sim 10 \text{ k}\Omega$) were used to measure the resistance by high precision phase sensitive detection technique (see FIG. 4.2). We used silver (Ag) leads which were fabricated by e-beam lithography for making electrical contact pads.

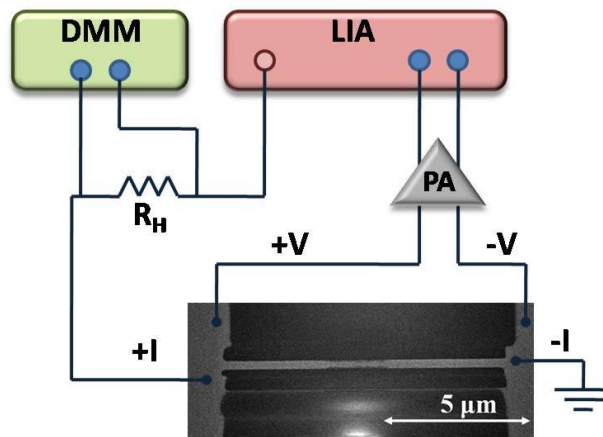


FIG. 4.2. Circuit diagram of four probe AC resistance measurement technique of Gd nanowire.

The MR measurement process was same as we followed for the film samples (see 3.3.3). The measurement of MR was done up to a field of $\mu_0 H < 0.2 \text{ T}$ at different temperatures ranging from 80 K to 310 K. Here magnetic field was applied parallel/perpendicular to the direction of current.

4.4. Resistance measurement and analysis

In FIG. 4.3, we show the resistivity (ρ) data as a function of T . The residual resistivity ρ_0 (contribution of defects and disorder) of the nanowire sample is larger than the bulk sample and because of that the ρ of S-2 is nearly four times larger than the S-1 sample.

The derivative of the resistivity $d\rho/dT$ is shown in inset of FIG. 4.3. The derivative also shows the characteristics of a ferromagnetic transition at T_C although it is much smeared out (in S-2) due to the finite size effect [4]. From the slope change of the resistivity derivative the T_C of S-1 and S-2 was found out at 292.5 K and 286.5 K.

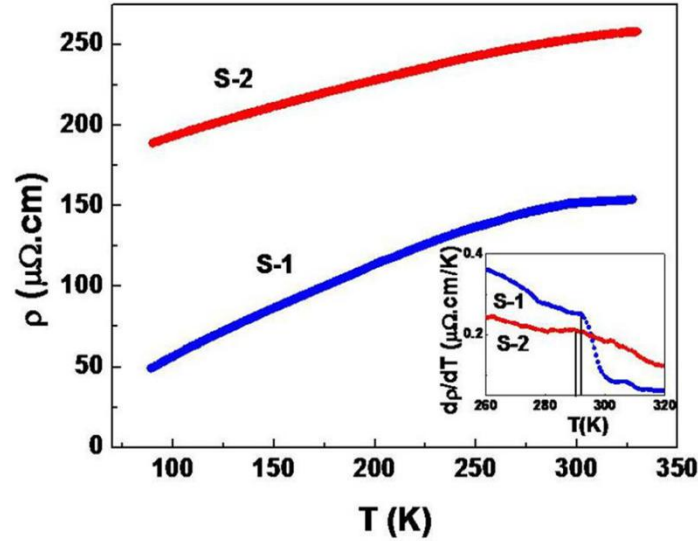


FIG. 4.3. Resistivity ρ vs. T for the two samples with inset showing the derivative to cleanly identify the T_C , marked by line.

4.5. Magnetoresistance measurement and analysis

In FIG. 4.4, we show the MR data as a contour plot to capture both the H and T dependence of the MR (data shown here are for field \parallel to current). The data are given as $\Delta\rho(H) \equiv \rho(H) - \rho(H = 0)$. The MR ($\Delta\rho(H)/\rho(H = 0)$) is negative ($\rho(H = 0) > \rho(H)$) at all H and T . The contour plot shows that there is a significant reduction of the magnitude of the $\Delta\rho(H)$ in the sample S-2; more importantly, these two samples show qualitatively different H and T dependences that reflect the differences in the underlying MR mechanism.

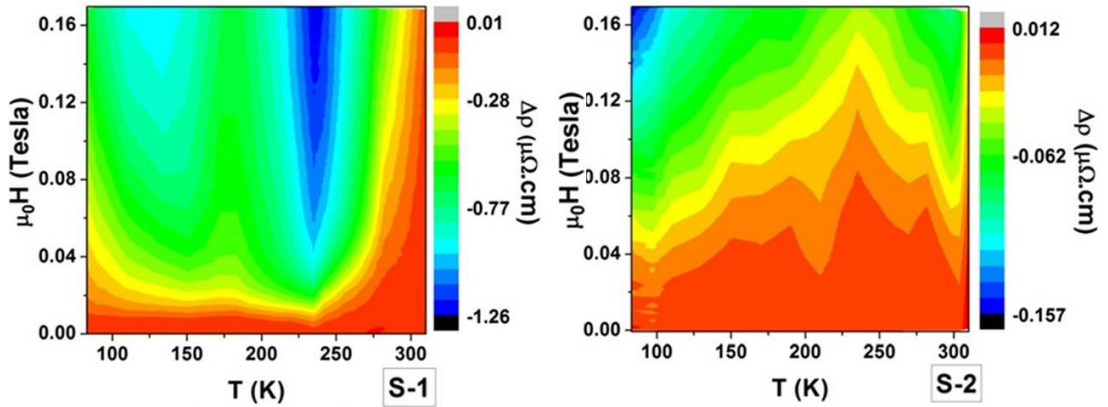


FIG. 4.4. Colour Plot of $\Delta\rho$ as a function of $\mu_0 H$ and T .

To bring out the distinction more clearly in FIG. 4.5, we show $\Delta\rho(H)$ as a function of T for both the samples measured at a field of $\mu_0 H = 0.17$ T. For sample S-1, the magnitude of $\Delta\rho(H)$ shows a very distinct and sharp peak at $T = 235$ K, which is spin reorientation transition T_{SR} . On further cooling, the magnitude of $\Delta\rho$ shows a distinct minimum at $T \approx 175$ K, a broad maximum at $T \sim 125$ K and on further cooling it decreases. The Magnetic Anisotropy Energy (E_A) in Gd has two distinct temperatures associated with it. Between T_C and T_{SR} , the easy axis of magnetization is in the same direction as the c -axis. In this

temperature range, the E_A as well as the two constants are small but finite. But at T_{SR} the anisotropy constants both are zero and E_A also is zero. Below the T_{SR} , the canting of the easy axis with c-axis increases, reaches a maxima at $T \equiv T^* \sim 190$ K, and then slowly decreases on cooling [2] but both the anisotropy constants increase [5]. The observed low field MR data in sample S-1 suggest that the response of the magnetic domains to the applied field is controlled by intrinsic magnetocrystalline anisotropy within the large crystallographic grain. The temperature variation of MR in sample S-1 is thus a clear reflection of the temperature variation of E_A and anisotropy constants that change at the spin reorientation transition.

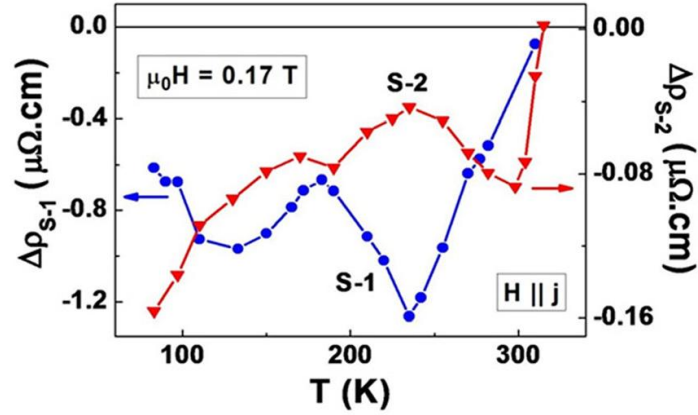


FIG. 4.5. $\Delta\rho$ as a function of T for $\mu_0H = 0.17$ T, plotted for both samples in same graph. $\Delta\rho_{S-1}$ and $\Delta\rho_{S-2}$ correspond to the resistivity change of S-1 and S-2.

At T_{SR} , the magnetocrystalline anisotropy energy becomes zero. Spins are isotropic in nature and they are free. As a result, MR is maximum at T_{SR} . In the region 235K and T_C the anisotropy energy is not zero. When the temperature increases, the magnetization decreases and correspondingly the absolute value of MR decreases with the increase of temperature. Below T_{SR} , the anisotropy energy and the canting angle both increase. This leads to a strong reduction of MR below T_{SR} . But simultaneously magnetization increases with decrease of temperature and it favours enhancement of MR. As a result, when the temperature is reduced below T_{SR} , these two competing process act in tandem and around 180 K the second one wins over the first and the magnitude of MR increases.

The nano-structured sample S-2, in contrast, does not show any prominent features in the magnitude of $\Delta\rho(H)$. After a sharp rise just below T_C , it slightly decreases on cooling and after reaching a shallow minimum around 235 K, it rises again at lower T . The MR in sample S-2 has no feature that can be associated with the intrinsic magnetocrystalline anisotropy within a crystallographic grain. In the nanowire sample (with average grain size ~ 35 nm), the intrinsic anisotropy within a crystallographic grain is thus not the dominant factor that controls the response of the magnetic domains. Size effect arising from lateral size reduction as well as dominance of disorder in grain boundaries reduces the effect of intrinsic anisotropy. This is a major result of this investigation.

The magnitude of the MR when H is \parallel to the current is larger than that when H is \perp to the current. This difference also has a clear temperature dependence that also shows the absence of any effect of the magnetocrystalline anisotropy in the MR of sample S-2. In FIG. 4.6, we show that the value of $\Delta\rho_{\parallel}$ for the sample S-1 is larger than the value of $\Delta\rho_{\perp}$ at all temperatures and the difference $\Delta\rho_a (= \Delta\rho_{\parallel} - \Delta\rho_{\perp})$ has a temperature dependence similar to $\Delta\rho_{\parallel}$ reaching a maxima at $T = T_{SR}$ and a minima close to T^* . In contrast, sample S-2 shows

isotropic MR with ($\Delta\rho_{\parallel} \approx \Delta\rho_{\perp}$) till $T \sim 150$ K. Below 150 K, $\Delta\rho_a$ gets a finite value but remains small. Thus, the features associated with magnetocrystalline anisotropy in $\Delta\rho_a$ of sample S-1 are absent in sample S-2.

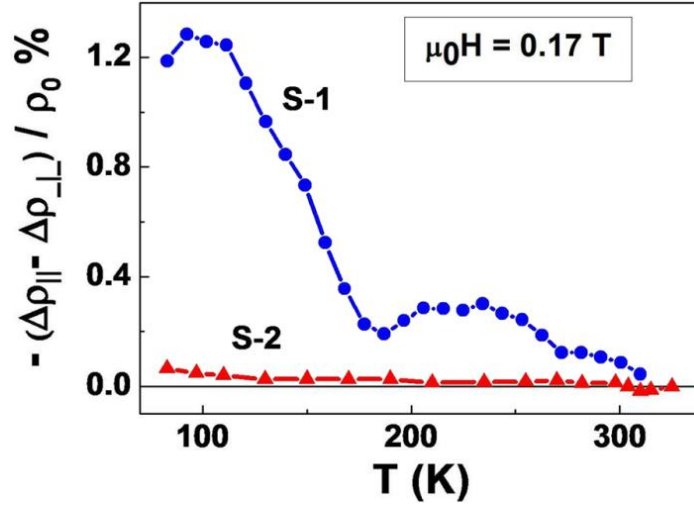


FIG. 4.6. $\Delta\rho_a / \rho_0 (\Delta\rho_a = \rho - \rho_0)$ as a function of T for $\mu_0 H = 0.17$ T, plotted for both samples in same graph. ρ_0 is the value of ρ at $\mu_0 H = 0$ T.

4.6. Discussion

The qualitative difference in the MR of the two samples can also be seen in the field dependence of MR %. These are shown at four representative temperatures for the two samples in FIG. 4.7 for H_{\parallel} to current geometry. In case of the reference sample (S-1), the field response is sharp and there is a rapid fall in the resistance at a low field typically $\mu_0 H < 0.015$ T. After that resistance changes slowly with field. The sharp response in the low field region arises when the magnetic domains align with the applied field thus reducing electron scattering that arises from misaligned magnetic domains. The gradual change at higher field arises due to reduction of spin fluctuations by an applied field. In S-1, the domains rotate against the local anisotropy field that is determined by the magnetocrystalline anisotropy. The magnetocrystalline anisotropy being small, the response occurs at a small field. In contrast, in the nano-structured sample, the field response is very different. There is no sharp change in the resistance in low field. Below a certain magnetic field, MR shows a fluctuation which is likely due to the random domain wall motion. This field (marked by an arrow in the figure), which we call H_S , reaches a temperature independent value ≈ 0.035 T at lower T . The value of H_S increases from $T \approx 190$ K and becomes 0.07 T around T_C (see FIG. 4.8).

In nano sample (S-2), the anisotropy energy (E_A) is dominated by shape anisotropy (K_S) which is independent of temperature. It can be represented by

$$K_S = \frac{1}{2} M_S H_K \quad (4.1)$$

, where M_S is the saturation magnetization and H_K is the anisotropic field [6]. When temperature approaches T_C , M_S sharply decreases and to make K_S constant H_K must increase. This H_K is equivalent to H_S .

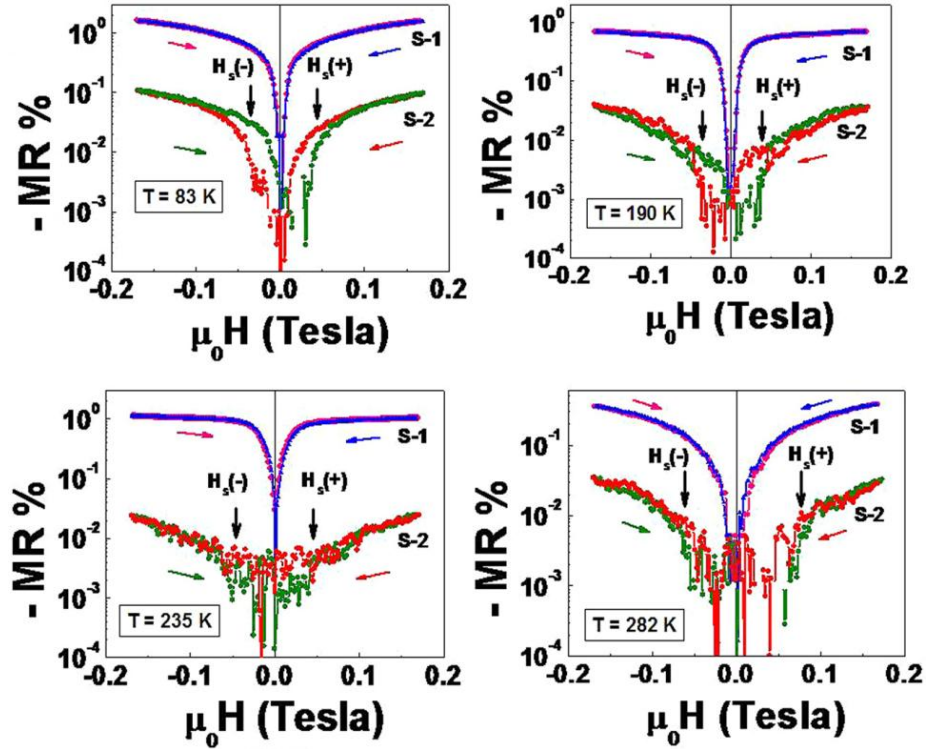


FIG. 4.7. MR% ($\Delta\rho/\rho_0\%$) as a function of μ_0H , plotted for both samples in same graph. Applied field is along the current direction ($H \parallel j$). The field H_S is indicated by arrow. $H_S(+)$ corresponds to the red curve, whereas $H_S(-)$ for the green. Note: Negative MR has been plotted to highlight the magnitude in log-scale.

For $H > H_S$, there is a gradual change in MR, whose field derivative is similar to that in the sample S-1. For $H < H_S$, there is an oscillatory behaviour of the resistance that is enhanced as T is increased. The magnitude of this oscillation is small. However, it is larger than the instrumental resolution for measurement of MR % ($\sim 10^{-4}$ %) although of the same order. These small oscillations can be manifestation of thermally induced de-pinning of domain walls. These decrease as the sample temperature is lowered.

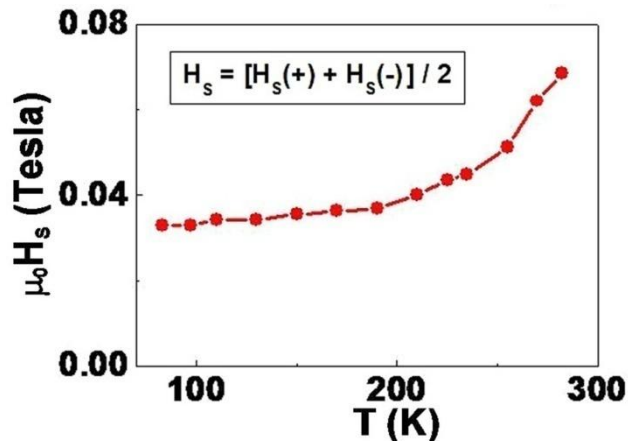


FIG. 4.8. Plot of μ_0H_S as a function of temperature.

Using the value of M_S of single crystal Gd (≈ 250 emu/g at 80 K) [7] and the measured switching field H_S (≈ 0.035 T at 80 K), we estimate a value of K_S of S-2 $\approx 3.4 \times 10^4$ J/m³.

The value of MR in S-2 is one order less than the value of MR in S-1. This indicates that before application of magnetic field, spins are already aligned along the field direction, which is parallel to the nanowire axis. Furthermore, the switching field H_S increases when the temperature T_C is approached from below (FIG. 4.8). H_S corresponds to the shape anisotropy field H_K . This is expected from Eqn. 4.1. M_S , the saturation magnetization decreases as the Currie temperature T_C is approached from below. Since K_S is T independent (being controlled by shape anisotropy), this will make H_K increase as T_C is approached from below.

Recent SANS studies have shown that the scale of spin disorder in a crystallographic grain is in the range of 30–40 nm [1]. Thus, in nanowires with grain size in this range one would expect sharp departure in the domain wall motion compared to samples with large grains or single crystals. From the above mentioned evidences, it appears that the MR in S-2 is not controlled by the magnetocrystalline anisotropy. It is controlled by the shape anisotropy and the spin disorder on the surface of the grain boundary.

4.7. Conclusion

This investigation shows how the low field magnetoresistance of Gd gets modified when it is taken from a bulk (with grain sizes in few μm ranges) to a nanowire that is nano-structured with grain sizes in the range of few tens of nm. The low field magnetoresistance is linked to motion of magnetic domains that is governed by local anisotropy field. In the sample with grain sizes of \sim few μm or more, the dominant effect arises from the intrinsic magnetocrystalline anisotropy. This gives rise to a prominent feature in MR at the spin reorientation transition temperature T_{SR} . In the nanowire, there is a stronger anisotropy field arising from a temperature independent anisotropy constant that can arise from the shape anisotropy of the nanowire and/or the spin disorder. The response of magnetic domains to the applied field and hence the MR is controlled by this anisotropy field. This leads to absence of features in MR that are associated with the intrinsic magnetocrystalline anisotropy. Though the micro-structure of the wire is similar to a bulk nanocrystal film and the lateral dimension of the nano wire 275 nm is much greater than the average grain size 35 nm, MR seems to be governed by the shape anisotropy and disorder. Magnetocrystalline anisotropy appears not to play an important role on MR in this case.

References

1. F. Döbrich, J. Kohlbrecher, M. Sharp, H. Eckerlebe, R. Birringer and A. Michels, *Phys. Rev. B*, **85**, 094411 (2012).
2. D. H. Ryan, A. Michels, F. Döbrich, R. Birringer, Z. Yamani and J. M. Cadogan, *Phys. Rev. B*, **87**, 064408 (2013).
3. A. McEwen, G. D. Webber and L. W. Roeland, *Physica*, **86B**, 531(1977).
4. M. Venkata Kamalakar and A. K. Raychaudhuri, *Phys. Rev. B*, **82**, 195425 (2010).
5. C. D. Graham, *J. Appl. Phys.*, **34**, 1341 (1963).
6. *Physics of Ferromagnetism*, **2nd ed.**, edited by S. Chikazumi (Oxford University Press, 1999).
7. S. Yu. Dan'kov, A. M. Tishin, V. K. Pecharsky and K. A. Gschneidner, Jr., *Phys. Rev. B*, **57**, 3478 (1998).

CHAPTER 5

Proposed Bose Einstein condensation of Magnons in nanostructured films of Gd at low temperature and its manifestations in electrical resistivity and magnetoresistance

In this chapter we report observation of proposed Bose Einstein Condensation (BEC) of magnons in the temperature range of around 20-25 K in nanostructured films of Gd with grain sizes that are much larger than the size range where superparamagnetism is expected. The observation was carried out using magnetic as well as high precision resistivity and magnetoresistance (MR) measurements done to low temperatures. We observe that the experimental observations depend crucially on one parameter, namely softening of the spin wave stiffness parameter D at BEC and the resistivity as well as MR can be related quantitatively to magnetic measurements through the temperature variation of the constant D in the vicinity of the transition. This paper establishes that the BEC reported before in nanocrystalline Gd can be extended to somewhat larger size range.

5.1. Introduction

In last decade there have been many reports of observation of Bose Einstein Condensation (BEC) of quasi-particle magnon in different solid state systems. BEC have been reported in spin-dimer compounds $\text{Pb}_2\text{V}_3\text{O}_9$, $\text{Sr}_3\text{Cr}_2\text{O}_8$, $\text{Ba}_3\text{Cr}_2\text{O}_8$, $\text{BaCuSi}_2\text{O}_6$, TiCuCl_3 , NH_4CuCl_3 , KCuCl_3 [1-9], quantum spin-1/2 antiferromagnet Cs_2CuCl_4 [10] and organic spin gap compound $\text{NiCl}_2\cdot 4\text{SC}(\text{NH}_2)_2$ [11,12]. BEC of magnons has been observed at room temperature [13] in Yttrium-iron-garnet (YIG) film by application of microwave pumping that creates a large enhancement of quasi-particle density which in turn leads to BEC. Very recently, there are also reports of temperature driven BEC of magnons in nanomaterials where by lowering the temperature one observes BEC. This type of temperature driven BEC have been reported in Co/Pt multilayer nanopillars [14] and more recently in Gd nanocrystal [15–17]. The last work is highly relevant to the present report as it is directly related to the present investigation that has been done on nanostructured Gd films.

In the nanostructured materials, the observations of magnon BEC have been made mainly through magnetic measurements like magnetization (M) or AC-susceptibility (χ). In very small size domains magnetic nanoparticles can also display superparamagnetism, although BEC and superparamagnetism are mutually exclusive. A size dependent phase diagram for Magnetic nanoparticles have been suggested [18,19]; where one may demarcate the ferromagnetic regime, BEC regime and superparamagnetic regime. We have also carried out frequency dependent AC-susceptibility measurements to establish that the observed magnetic transition is not a superparamagnetic blocking temperature. In view of the above discussion, it will be an important contribution if other experimental probes can be found that when done along with magnetic measurements, would strengthen the claim of BEC. In this paper we show that resistivity and magnetoresistance are excellent probes of finding magnon BEC. Briefly, the temperature driven BEC softens the Spin wave stiffness constant D near the transition [16]. Since the contribution of Spin waves to resistivity is related to D , one expects that the onset of BEC will lead to a change in resistivity as well as in the MR. This has been first showed in nanostructured Gd samples with average grain size of diameters 12 nm and 18 nm where the BEC temperatures is ≈ 16.5 K [15]. In this report we demonstrate the signature of BEC, in resistivity and MR in nanostructured Gd films around the BEC temperature ~ 20 K. The main motivation is to check whether the signature of magnon BEC is present in nanostructured solids with very different morphologies and with much larger grain size that are larger than previously reported grain size by a factor of 3 to nearly 10. We also carry out magnetic measurements in these samples and show that the signature of magnon BEC in resistivity as well as in MR can be quantitatively linked to the Spin wave constant softening obtained from the magnetization data.

Temperature driven magnon BEC transition had been very well studied in nanocrystalline samples of Gd [16,17] using magnetic, transport [15] as well as heat capacity measurements. These measurements were done on nanocrystalline Gd with average diameters of 12 and 18 nm which have T_{BE} around 20 K. The samples used in the above studies are high pressure compacted nanopowders produced by inert gas condensation. We used in this present investigation nanocrystalline films of Gd that have very different sample morphology as well as they have larger average grain sizes (35 nm and 105 nm). For comparison we also studied a polycrystalline bulk with average grain size ~ 4 μm . The choice of larger size has been done primarily to minimize the appearance of superparamagnetic contributions. In Gd this occurs for diameter ~ 10 nm [20].

5.2. Experimental

Three different Gd samples which were used in the work of low field MR measurement have been studied here. Two film samples of thickness 1900 nm (Film-A) and 250 nm (Film-B) with a bulk sample (Bulk) was studied. The average grain diameter of the Film-B, Film-A and Bulk sample is 35 nm, 105 nm and 4 μm . In Chapter-3 the sample preparation and characterizations are described in details.

X-ray diffraction (XRD) and Atomic force microscope (AFM) and scanning electron microscope (SEM) were used for structural and microstructural characterizations. Magnetization measurements were carried out with a commercial Quantum Design superconducting quantum interference device (SQUID) magnetometer. DC magnetization was measured in Zero Field Cooled (ZFC) and Field Cooled (FC) conditions under a magnetic field of 0.01 T for temperatures ranging from 5 K to 330 K. Isothermal magnetization curves were obtained under an applied magnetic field that varied from -1 T to $+1$ T. AC-susceptibility measurements were done in 3 different frequencies (17 Hz, 170 Hz and 1202 Hz) and in the presence of 3 different DC bias fields (0 T, 0.01 T and 0.1 T). The AC field was kept constant at 0.4 mT. The film samples were mounted such that the plane of the films was parallel to the direction of the applied magnetic field. The electrical measurements were done by conventional collinear four probe method. A lock-in amplifier based phase sensitive AC measurement technique with a low frequency transformer pre-amplifier was used for the resistance measurement that allows an accuracy and high precision of better than ± 1 ppm. The high precision AC measurement was also used for MR measurements, where the magnitude of the MR even at a field as high as 9 T was $< 6\%$. For temperature dependent resistivity measurement (3 K to 330 K) a closed cycle pulsed tube Helium cryostat was used.

5.3. Magnetization

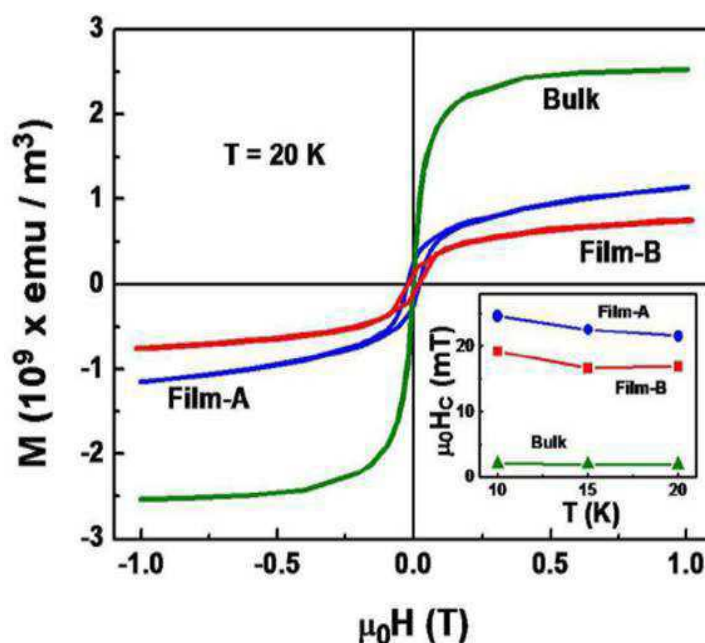


FIG. 5.1. Field (H) dependent magnetization (M) at 20 K. Inset shows the T dependent coercive field (H_C) of all samples at low temperature.

The magnetization (M) studies were done to align our measurements with past studies on nanocrystalline Gd and thus establish our samples show magnon BEC. We also used the temperature dependence of M to find the temperature dependence of the spin wave stiffness constant D as shown below. The field dependence of M at 20 K shows that all three samples are ferromagnetic in nature (FIG. 5.1). Above 0.2 T, M shows technical saturation but there exists a very small finite slope dM/dH beyond 0.2 T. From FIG. 5.1 it can be seen that in the nanostructured film H_C is finite and the superparamagnetism phenomena in the samples is ruled out by the results.

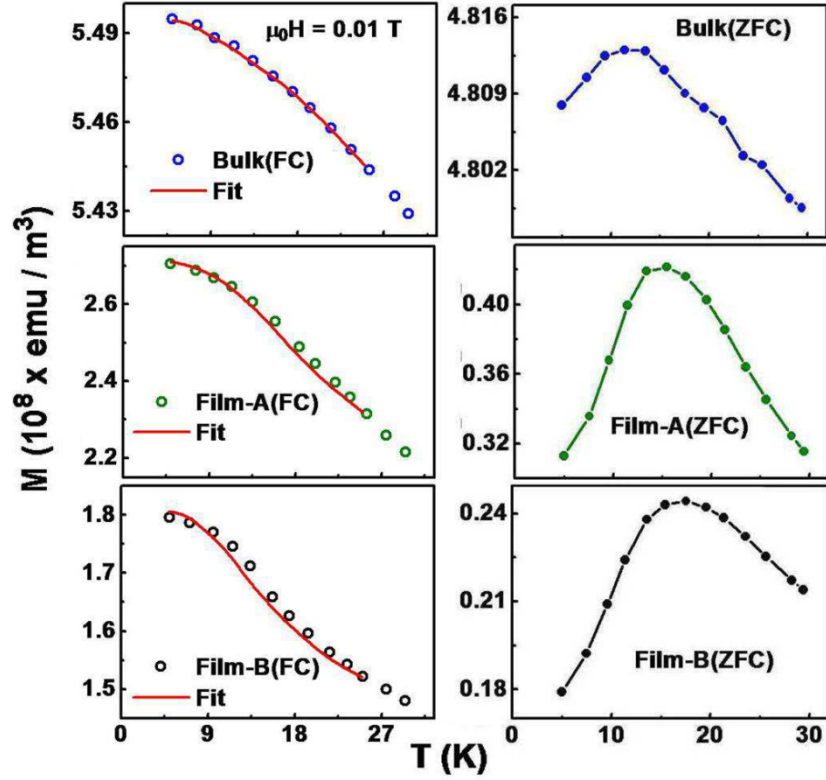


FIG. 5.2. M vs. T curve (FC and ZFC) for the film and bulk samples. The applied field is 0.01 T. The line through the FC data are fits to the Equation (5.1). (See text)

FIG. 5.2 shows the T dependence of M for ZFC (zero field cooled) and FC (field cooled) conditions for $T < 30$ K. The ZFC data show a peak for $T \approx 15$ K. Previous works in nanostructured Gd show similar features [17,21]. These features have been identified as due to BEC of the magnon. We show below that the T dependence of the ZFC $M - T$ is not a Blocking temperature. Though the amplitude is very small, surprisingly a peak is seen even in the ZFC magnetization data of the Bulk sample where the grain size is $\sim 4 \mu\text{m}$.

5.4. Softening of spin wave stiffness constant D

We utilize the M -TFC data to find out the dependence of the Spin wave stiffness constant D on T . The energy dispersion relation of the Spin waves can be written as [16] $\epsilon = Dk^2 + \Delta - \mu$, where k is the wave vector, D is the spin wave stiffness constant and $\Delta = \Delta_0 + g\mu_B H$. Δ_0 is the energy gap which is developed by the anisotropy energy. In our work we were using the value of single crystal Gd [16] ($\Delta_0 = 0.155(3)$ meV). The second term is the Zeeman term with Lande g factor, $g = 2$ for Gd (since $L = 0$ and $S = 7/2$). μ is the chemical potential.

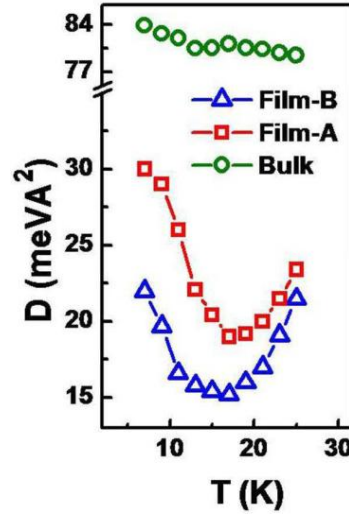


FIG. 5.3. D vs. T as obtained from the $M - T$ curve.

In the BEC state $\mu = 0$. As a result $\epsilon \approx Dk^2 + \Delta$. Therefore, at low temperature the magnon density n in a system of grain size d can be expressed by the following relation as [22],

$$n = \frac{1}{2\pi^2} \int_{k_0}^{\infty} \frac{k^2 dk}{e^{\beta(Dk^2 + \Delta)} - 1} \quad (5.1)$$

, where $\beta = 1/k_B T$. In the finite size sample grain, the spin waves are constrained inside the grains with the maximum wave length $\lambda \approx d$. Therefore, the integration must have a finite value of lower limit and it is $k_0 = 2\pi/d$. Finally the temperature dependence relation of n becomes (see Appendix-3)

$$n = AT^{3/2} - f(T, d) \quad (5.2)$$

, where $A = \left(\frac{k_B}{4\pi D}\right)^{3/2} \sum_{l=1}^{\infty} \frac{e^{-l\Delta\beta}}{l^{3/2}}$ and $(T, d) = \frac{1}{2\pi^2} \int_0^{k_0} \frac{k^2 dk}{e^{\beta(Dk^2 + \Delta)} - 1}$.

The magnetization (M) is related with the magnon density n as [16]

$$M = M_0 - g\mu_B n \quad (5.3)$$

, where $M_0 = M$ at $T = 0$ K. n increases with temperature T and thus leads to a deviation of M from M_0 . Eqn. 5.3, with n given by Eqn. 5.2, is the modified Bloch $T^{3/2}$ law.

Eqn. 5.3 is fitted to the low field FC $M-T$ data. The fits are shown in FIG. 5.2 as solid lines. It can be seen that the fit of Eqn. 5.3 to data are excellent. We obtain the T dependence of D from the fit and the data are shown in FIG. 5.3. It can be clearly seen that there is an anomalous softening of D in the temperature range around 20–25 K.

The value of D also goes down with decrease in the grain size d from the bulk to the film B. The smaller values of D s in the nanostructured films enhance the values of magnon densities in them leading to the observation of BEC. The temperature at which the anomalous softening of D occurs can be taken as the transition temperature T_{BE} .

5.5. Resistivity

The temperature (T) dependent resistivity (ρ) for all the samples is shown in FIG. 5.4. Though all the samples show metallic nature in spite of their high resistivities, there are observable differences between the film and the bulk resistivity data. For the bulk sample, as in a metallic solid, it has a residual resistivity $\approx 10.5 \mu\Omega\text{cm}$ and the normalized value $R_N = \rho(300\text{K})/\rho(5\text{K}) = 14.4$. At 300 K ρ shows approach to saturation as is often observed in

highly resistive metals and alloys that have $\rho > 100 \mu\Omega\cdot\text{cm}$. The values of ρ for the films are noticeably higher as expected primarily due to the grain boundary resistances. There are at low temperatures clear features (marked by arrows). These features we show below are associated with the softening of the Spin wave stiffness constant D .

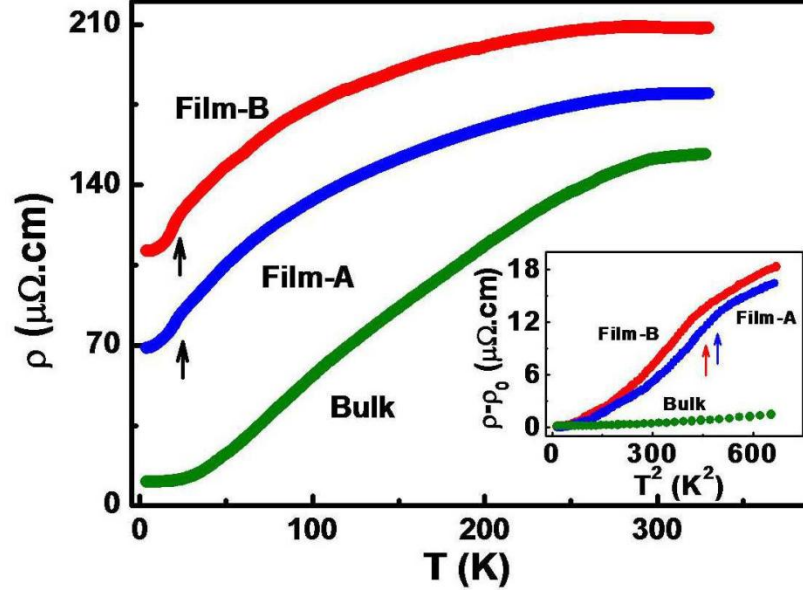


FIG. 5.4. ρ vs. T curve of all three samples. Inset shows the $\rho - \rho_0$ vs. T^2 plot. Transition temperatures are indicated by the arrows.

The resistivity ρ of a magnetic metal follows the Matthiessen's rule

$$\rho = \rho_0 + \rho_L + \rho_M \quad (5.4)$$

, where ρ_0 is the temperature independent residual resistivity (depends on the lattice defects and grain boundaries etc.), ρ_L is the temperature dependent lattice (phonon) contribution and ρ_M is the magnetic contribution. In most metallic solid the ρ_L is given by the Bloch-Grüneisen theory [23] which is determined primarily by the Debye Temperature θ_D . The magnetic contribution arises from the Spin wave and is given as [24],

$$\rho_M = \psi \left(\frac{T}{D} \right)^2 \quad (5.5)$$

, where ψ is a constant that depends on the ratio of s - f spin-orbit interaction energy and Fermi energy (E_f). Clearly a low D will accentuate the value of ρ_M and will make it more visible. In most magnetic solid the ρ_M is generally overwhelmed by the ρ_L except at low T .

To check for the existence of a discernible magnetic contribution at low temperatures, we have plotted $\rho(T) - \rho_0$ as a function of T^2 (for $T \leq 25$ K in the inset of FIG. 5.4). It can be seen that for the films the ρ at low T have a substantial magnetic contribution ($\sim T^2$) that follows Eqn. 5.5. For both the films for $T > 17$ K, there is an upward enhancement of the magnetic contribution due to softening of D as T_{BE} is approached. The features marked by arrows in the main figure are visible as change in slopes in the inset (also marked by arrow). For the bulk Gd sample, the value of D is much lower than that seen in conventional 3d ferromagnetic materials like Fe and Ni but it is much larger than the D seen in the films. As a result the magnetic contribution is much smaller in the bulk Gd compared to that in the films and we may neglect it. This observation allows us to use its temperature dependent resistivity ($\rho_L \approx \rho(T) - \rho_0$) as a measure of the lattice contribution for all the samples.

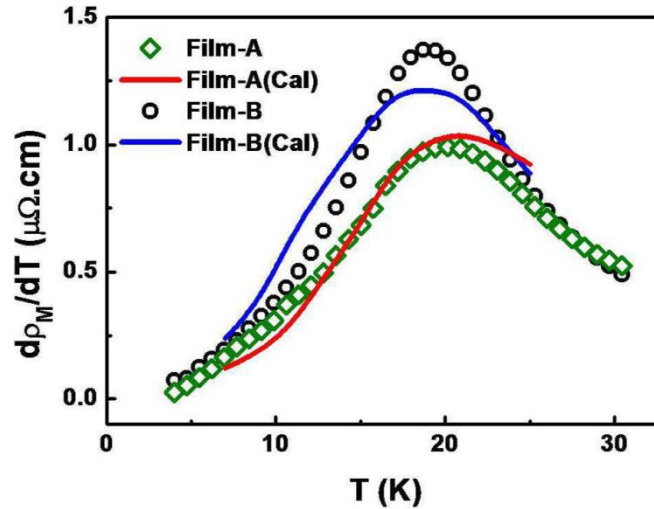


FIG. 5.5. $d\rho_M/dT$ vs. T curve of the film samples. Calculated value of $d\rho_M/dT$ is mentioned as “Cal”.

To identify the magnon BEC and connect the softening of D as seen in the resistivity data, we use the derivative of ρ as $d\rho_M/dT = d\rho/dT - d\rho_L/dT \approx d\rho/dT - d\rho_{bulk}/dT$, where $d\rho_L/dT$ is taken as the $d\rho/dT$ for the bulk sample (marked as $d\rho_{bulk}/dT$), following the argument above. A plot of $d\rho_M/dT$ for the two films is shown in FIG. 5.5. The features marked by arrows in the resistivity curves for the films in FIG. 5.4 show up clearly as rather sharp peak in the derivative curves. The maximum in $d\rho_M/dT$ can be identified with the minima in D vs. T curve evaluated from the magnetization data (see FIG. 5.3). To test this quantitatively, we calculate the derivative ($d\rho_M/dT = 2\psi T/D^2$) as a function of T from Eqn. 5.5 using the experimentally observed D at a given T . We obtain γ from the experimental derivative curve at $T = 7$ K by using the observed value of D at that temperature. $d\rho_M/dT$ was calculated from the temperature variation of D . The calculated curves are shown as lines in FIG. 5.5. It can be seen that they match well the experimental curves. It establishes the fact that the softening of D , which is taken as the signature of magnon BEC, leads to a maxima in the $d\rho_M/dT$ curve. We can then identify the T_{BE} from the temperature where $d\rho/dT$ peaks are observed at low T .

5.6. Magnetoresistance

Since the magnetic contribution to resistivity shows up a clear signature of BEC, it is expected that the magnetoresistance (MR) would also show a signature of BEC. Application of magnetic field will enhance T_{BE} [16]. Thus for a $T < T_{BE}$, application of field (H) will lead to an enhancement of D at a given temperature which will reduce ρ_M as given by Eqn. 5.5, leading to a negative MR. The effect is expected to be largest for $T \approx T_{BE}$. This would thus make MR yet another probe to identify the BEC. (We define the MR as $MR\% = 100 \times \frac{\Delta\rho}{\rho_0} =$

$$100 \times \frac{(\rho - \rho_0)}{\rho_0}, \text{ where } \rho_0 \equiv \rho(H=0).)$$

At a temperature ($T = 20$ K) the H dependent in-plane transverse MR (applied field and measuring current are perpendicular) are shown in FIG. 5.6(a). MR is negative for all the samples. MR has been measured up to a field of 9 T. At low temperature and high field, the MR for the film samples become larger compared to that of the bulk. There are also differences in field dependence. In the film samples there is a clear linear component, which we show below is linked to the field dependence of D . The T dependence of MR at a given

field $\mu_0 H = 9$ T are shown in FIG. 5.6(b). The magnitude of MR is clearly low (Note that the data have been plotted as $-\text{MR}\%$). However, for films A and B there are clear maxima for $T \approx T_{BE}$, as determined from the resistivity derivative curve (FIG. 5.5).

MR can be fitted by a single function of H as [15]

$$\frac{\Delta\rho}{\rho_0} = c_1 H - c_2 H^2 \quad (5.6)$$

, where c_1 and c_2 are the weight factors of the representative terms. The first term ($c_1 H$) represents the contribution arising from the breaking of coherent long range ordering of magnons and the second term ($-c_2 H^2$) is the Lorentz term (present in transverse MR) contribution. The value of c_1 and c_2 has been obtained from the data by fitting them to Eqn. 5.6.

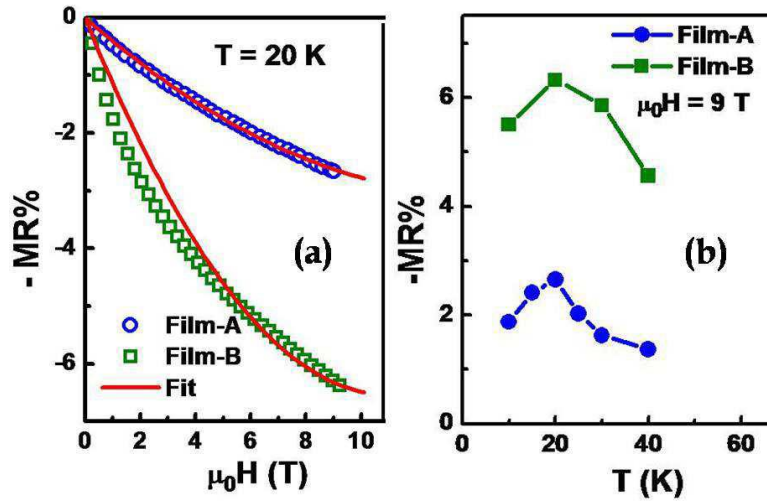


FIG. 5.6. (a) Field (H) dependent MR% at 20 K for film samples. Data is fitted by Eqn. 5.6. (b) Temperature (T) dependent $-\text{MR}\%$ ($\mu_0 H = 9$ T). To show the absolute value negative MR has been plotted.

The parameter c_1 ($-4.22(4) \times 10^{-3} \text{ T}^{-1}$ and $-11.92(1) \times 10^{-3} \text{ T}^{-1}$ for Film-A and Film-B) varies. We show that this happens due to dependence of c_1 on D which itself has a dependence on H .

Using Eqn. 5.5 for a particular temperature it can be written as

$$\frac{\Delta\rho}{\rho_0} = \frac{\rho - \rho_0}{\rho_0} = \left(\frac{1}{D^2} - \frac{1}{D(0)^2} \right) D(0)^2 = \frac{D(0)^2}{D^2} - 1$$

Therefore,

$$\frac{d}{dH} \left(\frac{\Delta\rho}{\rho_0} \right) = -2 \left(\frac{D(0)}{D} \right)^2 \left[\frac{1}{D} \frac{dD}{dH} \right]$$

Again from Eqn. 5.6, neglecting the Lorentz part in the field range concerned:

$$\begin{aligned} \frac{d}{dH} \left(\frac{\Delta\rho}{\rho_0} \right) &= c_1 \\ \text{or, } c_1 &= -2 \left(\frac{D(0)}{D} \right)^2 \left[\frac{1}{D} \frac{dD}{dH} \right] \\ c_1 &= -\frac{2}{D_N^2} c_{1N} \end{aligned} \quad (5.7)$$

, where $c_{1N} = \frac{1}{D} \left(\frac{dD}{dH} \right)$ and $D_N = D/D(0)$ is the normalized value of D , where $D(0)$ is the value of D at $H = 0$. Since D increases with H , c_{1N} is > 0 and c_I is < 0 , as observed experimentally.

It is noted that the low temperature ρ as well as the MR data of the films done in this investigation, have a broad similarity to the data on nanostructured bulk solid done previously. The present investigation showed that barring details the signatures of BEC in magnetic as well as the transport data are mostly independent of the morphology of the nanostructured Gd.

5.7. AC-susceptibility

The discussion so far assumed that the transition seen at low T is distinct from what is expected of a superparamagnetic transition. In fact the particle size used here being much larger than the size range where superparamagnetism is expected, we can rule out such effects. In addition, we have two more experimental reasons to rule out the above effect. First, it can be seen from FIG. 5.1 inset that the nanostructured films have finite coercive field H_C which are much larger than those of the nanostructured films. In a superparamagnetic particle the H_C is expected to ≈ 0 . Next we show using measurement of AC χ that there is no evidence of blocking transition as it happens in superparamagnetic particles which often lead to a hump in ZFC M vs. T curve similar to those seen in FIG. 5.2.

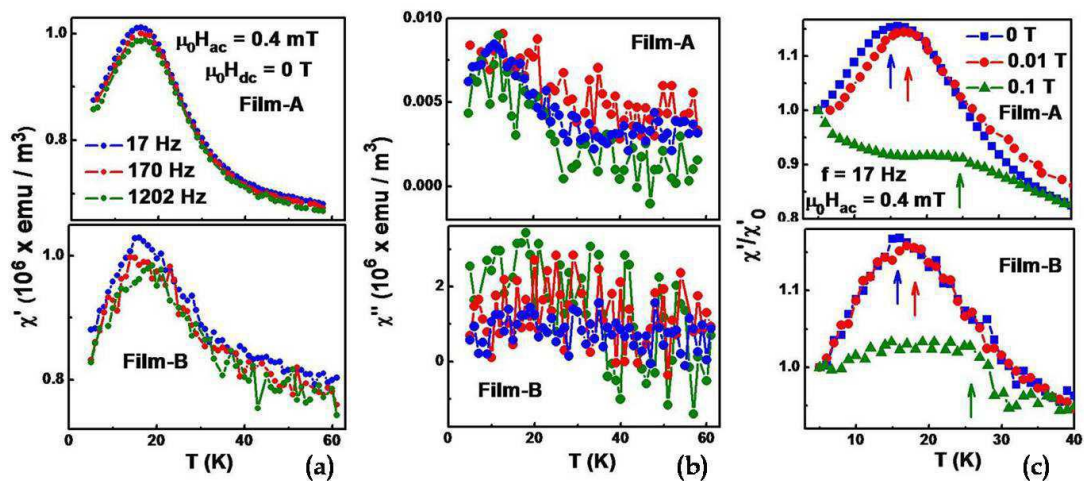


FIG. 5.7. (a) Temperature dependence of the real part of AC-susceptibility (χ') for two films samples at three different frequencies (17 Hz, 170 Hz and 1202 Hz). Amplitude of AC-magnetic field ($\mu_0 H_{ac}$) and dc bias field ($\mu_0 H_{dc}$) is 0.4 mT and 0 T. (b) Same for the imaginary part of AC-susceptibility (χ''). (c) The T dependence of the normalized susceptibility (χ'/χ'_0), where $\chi'_0 = \chi'(T = 5 \text{ K})$, at frequency 17 Hz of three different samples for DC bias field 0 T, 0.01 T and 0.1 T. Arrows indicate the shifting of T_{BE} with DC field intensity.

For zero DC bias field the T dependent real (χ') and imaginary (χ'') part of the susceptibility have been plotted for three different frequencies ranging from 17 Hz to 1200 Hz. The data were taken with no applied dc field and a modulation field of 0.4 mT. In Film-A and Film-B there are peaks in χ' - T curve is observed at temperatures where the ZFC M - T curves show a hump (the data in bulk sample shows no such features). Importantly, the peak position is independent of the measurement frequency. This is unlike blocking temperature, which being a kinetic effect, shows a clear dependence on frequency of measurement. One thus can rule out blocking temperature associated with these features.

In FIG. 5.7(c) we plot the χ' as a function of T for different applied DC field (H_{dc}) for a fixed frequency at 17 Hz. The data are normalized as χ'/χ'_0 (here $\chi'_0 = \chi'$ at $T = 5$ K). As H_{dc} increases result shows that the transition temperature moves toward higher T values. This is the indication of a phase transition where T_{BE} shifts to higher value as a DC field is applied [16].

5.8. Conclusion

Magnetic measurements as well as high precision resistivity and MR measurements were carried out to low temperatures on nanostructured films of Gd. One film with thickness of 250 nm and nearly spherical grains, have average grain size of about 35 nm. The other film with thickness of 1.9 μm has oblate grains with average diameter in excess of 100 nm. Magnetic as well transport measurements show clear signatures of BEC of magnons in the temperature range of ≈ 20 –25 K. The transport measurements can be related quantitatively to magnetic measurements through the Spin wave stiffness constant D that show anomalous softening near the BEC transition temperature T_{BE} .

This work establishes that the BEC reported before in nanocrystalline Gd can be observed even in nanostructured materials somewhat larger size. We also ruled out occurrence of superparamagnetism using AC-susceptibility measurements. Absence of frequency dependence of AC-susceptibility showed that the transition temperature observed in magnetic measurements cannot be related to superparamagnetic blocking temperature. The paper also establishes the independence of BEC on sample morphology. The observation of magnon BEC is possible in Gd nanostructures due to its relatively much lower spin stiffness constant D compared to other magnetic nanomaterials.

References

1. B. S. Conner, H. D. Zhou, Y. J. Jo, L. Balicas, C. R. Wiebe, J. P. Carlo, Y. J. Uemura, A.A. Aczel, T. J. Williams and G. M. Luke, *Phys. Rev. B.*, **81**, 132401 (2010).
2. A. A. Aczel, Y. Kohama, C. Marcenat, F. Weickert, M. Jaime, O. E. Ayala-Valenzuela, R. D. McDonald, S. D. Selesnic, H. A. Dabkowska and G. M. Luke, *Phys. Rev. Let.*, **103**, 207203 (2009).
3. A. A. Aczel, Y. Kohama, M. Jaime, K. Ninios, H. B. Chan, L. Balicas, H. A. Dabkowska and G. M. Luke, *Phys. Rev. B.*, **79**, 00409(R) (2009).
4. M. Kofu, H. Ueda, H. Nojiri, Y. Oshima, T. Zenmoto, K. C. Rule, S. Gerischer, B. Lake, C. D. Batista, Y. Ueda and S.-H. Lee, *Phys. Rev. Let.*, **102**, 177204 (2009).
5. M. Jaime, V. F. Correa, N. Harrison, C. D. Batista, N. Kawashima, Y. Kazuma, G.A. Jorge, R. Stern, I. Heinmaa, S. A. Zvyagin, Y. Sasago and K. Uchinokura, *Phys. Rev. Let.*, **93**, 087203 (2004).
6. V. N. Glazkov and A. I. Smirnov, *Phys. Rev. B.*, **69**, 184410 (2004).
7. Ch. Rüegg, M. Oettli, J. Schefer, O. Zaharko, A. Furrer, H. Tanaka, K.W. Krämer, H.-U. Güdel, P. Vorderwisch, K. Habicht, T. Polinski and M. Meissner, *Phys. Rev. Let.*, **93**, 037207 (2004).
8. A. Oosawa, T. Takamasu, K. Tatani, H. Abe, N. Tsujii, O. Suzuki, H. Tanaka, G. Kido and K. Kindo, *Phys. Rev. B.*, **66**, 104405 (2002).
9. T. Nikuni M. Oshikawa, A. Oosawa and H. Tanaka. *Phys. Rev. Let.*, **84**, 5868 (2000).
10. T. Radu, H. Wilhelm, V. Yushankhai, D. Kovrizhin, R. Coldea, Z. Tylczynski, T. L'uhmann and F. Steglich, *Phys. Rev. Let.*, **95**, 127202 (2005).
11. L. Yin, J. S. Xia, V. S. Zapf, N. S. Sullivan and A. Paduan-Filho, *Phys. Rev. Let.*, **101**, 187205 (2008).
12. V. S. Zapf, D. Zocco, B. R. Hansen, M. Jaime, N. Harrison, C. D. Batista, M. Kenzelmann, C. Niedermayer, A. Lacerda and A. Paduan-Filho, *Phys. Rev. Let.*, **96**, 077204 (2006).
13. S. O. Demokritov, V. E. Demidov, O. Dzyapko, G. A. Melkov and A. N. Slavin, *New J. Phys.*, **10**, 045029 (2008).
14. E. Della Torre, L. H. Bennett and R. E. Watson, *Phys. Rev. Let.*, **94**, 147210 (2005).
15. S. P. Mathew and S. N. Kaul, *J. Phys.: Condens. Matter.*, **27**, 056003 (2015).
16. S. N. Kaul and S. P. Mathew, *Phys. Rev. Let.*, **106**, 247204 (2011).
17. S. P. Mathew and S. N. Kaul, *J. Phys.: Condens. Matter.*, **23**, 266003 (2011).
18. L. H. Bennett, E. Della Torre, P. R. Johnson and R. E. Watson, *J. Appl. Phys.*, **101**, 09G103 (2007).
19. Lawrence H. Bennett and Edward Della Torre, *J. Modern Phys.*, **5**, 693 (2014).
20. X. G. Liu, D. Y. Geng, Q. Zhang, J. J. Jiang, W. Liu and Z. D. Zhang, *Appl. Phys. Let.*, **94**, 103104 (2009).
21. S. P. Mathew and S. N. Kaul, *J. Phys.: Condens. Matter.*, **24**, 256008 (2012).
22. P. Crespo, J. M. González, A. Hernando and F. J. Yndurain, *Phys. Rev. B.*, **69**, 012403 (2004).
23. Neil W. Ashcroft and N. David Mermin, *Solid State Physics*, Brooks/Cole-Thomson Learning, (2007), ISBN: 81-315-0053-5.
24. Isao Mannari, *Prog. Theo. Phys.*, **22**, 335 (1959).

CHAPTER 6

Current driven magnetic domain wall motion in a nanoconstriction on a Gd microstrip and its application to find out the value of anisotropy energy

We report observation of a DC-current driven magnetic domain wall (DW) motion in an artificially created nano constriction (size ~300 nm) in a microstrip of 4f ferromagnet Gd (film thickness 40 nm), where beyond a critical current density a sharp reduction in the resistance is observed that gives the DW resistance R_w . This is similar to that seen in nanoconstrictions made in a conventional 3d ferromagnet like Ni and its alloys. The effect is most prominent at 100K or below and becomes smaller as the temperature increases and it vanishes as $T \rightarrow T_C$. The value of R_w was used in conjunction with the measured anisotropic magnetoresistance (AMR) to find the domain wall thickness (δ) and the anisotropy energy (E_A) of the Gd film. Observation of this phenomenon in a 4f metal Gd, which is distinct from itinerant conventional 3d transition metal, extends the phenomena to a new class of ferromagnet. Low ferromagnetic transition temperature of Gd, also allows us to study the phenomena and the evolution of δ and E_A as a function of temperature.

6.1. Introduction

One of the important developments in the field of magnetism in last decade has been the observation of domain wall motion in 3d transition metals (like Ni) and alloys (like Permalloy) driven by a DC-current in a nanoconstriction (NC) of sizes ranging from few tens of nanometers to few hundreds of nanometers [1,2]. The effect shows up as jump in resistance of the NC at a critical current when the current through the NC is increased. The resistance jump has been linked to the resistance of the domain wall (DW) which is driven out of the constriction and has been explained [2-4] as arising from current induced s-d exchange interaction. While the above phenomena has been well studied in 3d transition metals like Ni and its alloys, the applicability of the fundamental concepts in a 4f ferromagnetic metal like Gd has never been tested, although as explained below there are reasons to expect that such a phenomena can indeed occur in Gd. Gd has a ferromagnetic Curie temperature ~ 293 K and at low temperatures it is a strong ferromagnet, having a saturation magnetic moment of $7.55 \mu_B$ arising from 4f electrons. In Gd there are well-localized spin only moments that are indirectly coupled via the Ruderman-Kittel-Kasuya-Yosida (RKKY) interaction. This is distinct from the magnetism in more itinerant conventional 3d ferromagnetic materials like Fe, Ni, Co etc. that do not have a localized moment. Observation of the current induced DW motion in Gd will therefore would allow its generalization beyond conventional s-d interaction.

Gd has been used with NC on Ni to modify the DW pinning as well as for lowering the critical current. A thin layer of Gd (~ 4 nm) sandwiched between two permalloy thick layer was found to trap a in plane DW and was used to measure cleanly the current driven DW motion in permalloy [6]. Recently Gd has been alloyed with Ni to reduce the threshold current for switching [7]. It is thus of interest to investigate such a current induced DW motion directly in a NC in a Gd film.

Table 6.1: A_{ex} of different magnetic materials.

Material	Co	Fe	Ni ₈₀ Fe ₂₀	Ni	Gd
A_{ex} (10^{-12} J/m)	30	21	13	9	5

The physics of current driven DW motion in nanoconstrictions (NC) have been theoretically worked out before in 3d ferromagnetic metals [3,4] and the magnitude of the resistance jump has also been deduced [8]. The observation of the current driven DW motion in a NC depends on the capability of the NC to trap a DW (Néel type) during a field cooling to below T_C . The trapping depends on the exchange stiffness co-efficient A_{ex} . Trapping of a DW at the constriction is energetically favourable for smaller value of A_{ex} . For instance, it has been observed in NC's of Nickel (Ni) and its alloy Permalloy (Ni₈₀Fe₂₀) that have relatively smaller A_{ex} , while it has not been seen in Iron (Fe) and Cobalt (Co) that have with larger A_{ex} [1]. In Table 6.1, we show a collection of A_{ex} values for the 3d metals and alloys. Interestingly, the above phenomenon has never been investigated beyond 3d transition metals. Table 6.1 shows that 4f transition metal Gd has even less value of A_{ex} compared to Ni. It is thus expected that the phenomenon should be observable in Gd. In this work we show that a clean jump in resistance of a NC (~ 300 nm) made on a microstrip of Gd could be observed when the current through the constriction crosses a specific current density J_C . The observed phenomenon is very similar to that observed in Ni and Permalloy NC.

The observed resistance jump when the current is ramped up, gives the domain wall resistance R_W . When a domain wall is present at the NC, the applied current directions that is perpendicular to the magnetization at the constriction shows a higher resistance. Beyond a critical J_{dc} when no domain wall is present at the constriction at zero magnetic field, the

magnetization lies along the length of the wire due to the shape anisotropy and the applied current direction is parallel to the magnetization. This lowers the resistance of the NC. From the measured RW, we deduced the DW thickness δ using the measured anisotropic magnetoresistance (AMR) (the method is elaborated below) and then the anisotropy energy (E_A) in the film of Gd. The use of the DW resistance to determine E_A had not been done before and this turns out to be a viable alternative to use of torque magnetometry to measure the same. In addition, the experiment has been done on Gd that has a low ferromagnetic transition temperature ($T_C \approx 293$ K), which also allows us to study evolution of the current driven DW motion as a function of temperature below T_C .

One of the main themes of the thesis is to investigate different aspects of the anisotropy energy in Gd nanostructures. The observation of the domain wall orientation in an artificially fabricated nanoconstriction in a Gd microstrip is predominantly an anisotropy driven phenomena. The utilization of the phenomena in quantitatively evaluating the value of E_A is thus a significant contribution of this thesis. We also would like to point out that using a DC biasing for stressing and using a superimposed small AC to find the resistance is an innovation that is rarely used in this field.

6.2. Experimental

The NC was fabricated on a film of Gd (thickness $t \approx 40$ nm) grown on quartz substrate at 350°C in a base vacuum of 5×10^{-8} mbar using an e-beam evaporation system. The film was grown with a rate of 0.05 nm/s. The film after growth was covered with a thin layer (3 nm) of Au to protect it from the oxidation. The film was then patterned into a microstrip of dimension $30 \times 5 \mu\text{m}^2$ using optical lithography and chemical etching with 5 % HCl. A constriction of width ~ 300 nm was made on the middle of the rectangle by milling with 30 keV Ga ions using a Focused Ion beam (FIB). The NC was then electrically contacted by Au/Cr contact pads fabricated using electron-beam lithography writing and lift-off. The microstrip with the NC is shown in FIG. 6.1.

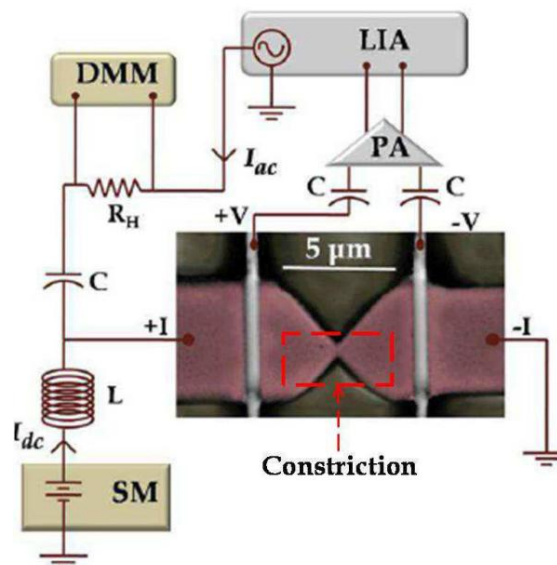


FIG. 6.1. A $0.3 \mu\text{m}$ constriction was made on a $5 \mu\text{m} \times 30 \mu\text{m}$ microstrip of a 40 nm Gd film by Ga ion Focused Ion Beam milling. The constriction is shown by a red box. The schematic measurement scheme is shown that allows measurement of resistance using an AC modulation current and phase sensitive detection that is mixed with the stressing DC-current I_{dc} . The two current sources are protected by Inductor L and capacitor C .

The experiment of current driven DW motion was carried out in the set-up shown in FIG. 6.1, which allows measurement of very small resistance change using phase sensitive AC detection in presence of a DC driving current through the constriction. In this method a small AC current (i_{ac}) generated by the lock-in amplifier (LIA), is mixed with a DC-current ($I_{dc} \gg i_{ac}$) regulated by a Source Meter (SM). The two sources are separated out by a capacitor ($C = 10 \mu\text{F}$) and an inductor ($L = 6.8 \text{ mH}$). The resistance is measured by measuring the AC-voltage v_{ac} developed across the voltage terminals across the NC using a phase sensitive detection so that resistance measured $R(= v_{ac}/i_{ac})$ is measured independent of the driving DC-current I_{dc} . We could achieve a resolution better than 1 ppm by this method.

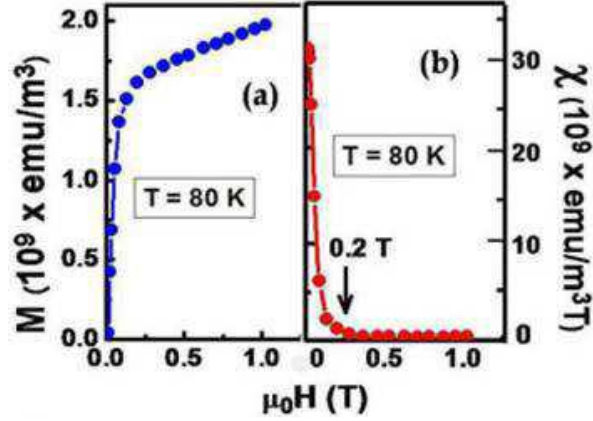


FIG. 6.2. (a) Magnetization (M) vs. Field ($\mu_0 H$) of the Gd film taken at 80 K. (b) Shows the susceptibility $\chi = M/H \rightarrow 0$ beyond the technical saturation field of 0.2 T.

The measurement was carried out in a liquid nitrogen bath type cryostat that allows measurement from 80 K to 300 K using an air core solenoid that can produce a magnetic field up to 0.2 T. This field is enough to make the Gd reach its technical saturation as measured from the magnetization curve, shown in FIG. 6.2 that also shows the susceptibility $\chi = M/H \rightarrow 0$ beyond 0.2 T.

6.3. Current driven resistance change

Isothermal $R-I_{dc}$ measurements have been done from 100 K to 250 K. The following protocol was followed. At each temperature, the sample was cooled from above T_C to the specific temperature $T(T < T_C)$, with a magnetic field of $\mu_0 H = 0.2$ T, applied along the long axis of the sample. At low temperature when the field was removed, a DW was plugged at the constriction [1, 2]. At that fixed temperature the stressing current I_{dc} was then ramped up. At a critical DC-current (I_C) the DW was extracted from the constricted region and the resistance of the sample sharply falls down to a lower value (see FIG. 3(a)).

The resistance difference measured, $\Delta R = R - R_f$, where $R_f = R \text{ at } I_{dc} = 10 \text{ mA}$ ($>$ the critical current I_C), is the resistance value of the sample without DW. When the current is ramped down the sample stays in the low resistance state, showing that the critical current has extracted the DW from the constriction and the DW is not re-captured by current removal. A Néel DW can be plugged at the constricted region of a thin film. Previous reports showed that the extraction of this DW by a high density DC-current ($\sim 10^7 \text{ A}/\text{m}^2$) makes a sharp fall in the resistance of the NC [2]. This occurs due to the positive contribution of DW resistance arising due to spin-dependent impurity scattering at the DW [8].

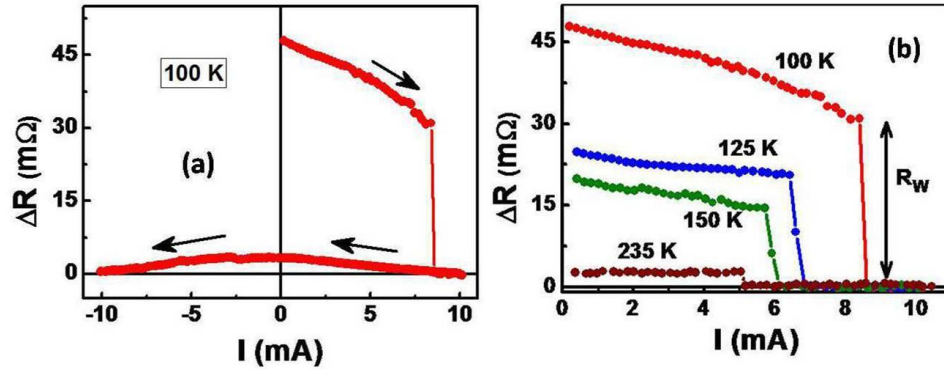


FIG. 6.3. (a) Change in the resistance ΔR of the NC as a function of the DC stressing current I_{dc} . The sharp fall in resistance of the NC takes place when the DW is driven out of the constriction and it does not form again at the constriction when the current is cycled back. (b) The resistance R vs. I_{dc} at different temperatures. The domain wall resistance R_W is marked by arrow. As $T \rightarrow T_C$, $R_W \rightarrow 0$.

The experiment was carried out at different temperatures below T_C . At each temperature the sample was heated above T_C and then cooled to the desired temperature in an axial field of 0.2 T as described before. The data for few selected temperatures are shown in FIG. 3(b). The full data are given below in Table 6.2.

Table 6.2: Full data of the experiment.

T (K)	R_f (Ω)	R_W (m Ω)	R_W/R_f %	I_C (mA)
100	67.86	30	0.044	8.40
126	71.01	20	0.028	6.45
150	73.81	14	0.019	5.70
170	75.73	12	0.0158	6.10
215	78.82	5.4	0.0068	5.90
235	79.81	2.58	0.0032	5.06
250	80.51	0.625	0.00078	4.90

* Here R_W is the domain wall resistance and $R_f = R$ at $I_{dc} = 10$ mA ($> I_C$).

6.4. Domain wall resistance R_W

The resistance arising from the DW can be measured directly by $R_W = R_C^- - R_C^+$, where R_C^- and R_C^+ are the values of R for $I = I_C^-$ (just below I_C) and $I = I_C^+$ (just above I_C). The experiment allows us to measure the evolution of R_W and I_C as the temperature is taken from $T \approx 0.33 T_C$ to $T \rightarrow T_C$. Data are shown in FIG. 6.4, where we show temperature variation of R_W and the critical current density (J_C) as a function of T .

As the temperature increases, the value of both R_W and J_C decrease. As $T \rightarrow T_C$, R_W and $J_C \rightarrow 0$. The value of R_f , R_W and the change in percentage R_W/R_f are shown in Table 6.2. Closer to T_C ($T > 0.9 T_C$) the resistance change becomes < 1 ppm, which is the limit of our experimental resolution.

Observation of the DW motion by a DC stressing current beyond a critical current density in the 4f metal Gd, as has been observed in 3d metals and alloys before, is definitely a confirmation of the applicability of the basic theory in a system that has s-f interaction and localized moment. It is noted that such a phenomena in a 4f metal has not been seen before. Observation of the temperature evolution of the phenomena from $0.3 T_C$ to nearly $0.85 T_C$ is

also new, because high value of T_C in conventional 3d metals and alloys being high, this cannot be investigated in such materials.

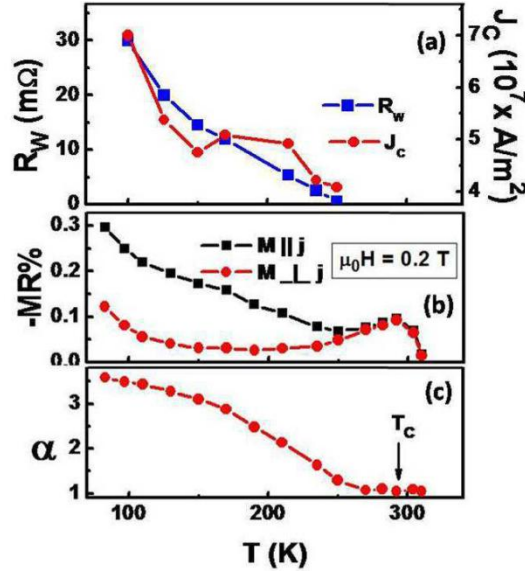


FIG. 6.4. (a) DW resistance R_W and the critical current density J_C as a function of T . The T_C is marked by an arrow. (b) Anisotropic magnetoresistance AMR as measured as a function of T . (c) The anisotropy parameter α as calculated from AMR as a function of temperatures.

6.5. Calculation of domain wall thickness δ

Next we use the value of R_W to find the thickness of domain wall (δ) which we then use to find the value of the anisotropy energy E_A using the relation [9]:

$$\delta = \pi \sqrt{\frac{A_{ex}}{E_A}} \quad (6.1)$$

A spin dependent impurity scattering mechanism for the positive contribution of DW resistance has been proposed [8]. The current passes perpendicular to the DW and the resistivity ratio between the resistivity ρ_W (ρ with DW) and ρ_0 (ρ without DW) can be expressed as:

$$\frac{\rho_W}{\rho_0} = \frac{\varphi^2}{5\delta^2} \frac{(\alpha - 1)^2}{\alpha} \left(3 + \frac{10\sqrt{\alpha}}{\alpha + 1} \right) = \frac{\varphi^2}{5\delta^2} \alpha_T \quad (6.2)$$

$$\alpha_T = \frac{(\alpha - 1)^2}{\alpha} \left(3 + \frac{10\sqrt{\alpha}}{\alpha + 1} \right) \quad (6.3)$$

Where, $\alpha = \rho_{\uparrow}/\rho_{\downarrow}$, is the ratio of the resistivities corresponding the two different electron spin channels up (\uparrow) and down (\downarrow), $\varphi = \hbar^2 k_F / 16\pi m J_{so}$, J_{so} being the spin-orbit interaction has a typical value of $J_{so} = 0.5$ eV [8], m_e is the electron mass, the Fermi wave vector, $k_F = 1.1 \text{ \AA}^{-1}$ for Gd [10]. α_T can be evaluated from measured value of the anisotropic Magnetoresistance (AMR). The AMR is defined as $\text{AMR} = \text{MR}_{\perp} - \text{MR}_{\parallel} = [\rho_{\perp} - \rho_{\parallel}] / \rho \simeq (\alpha - 1)\gamma$. $\text{MR} = [\rho(H) - \rho(0)] / \rho(0)$. MR_{\parallel} and MR_{\perp} refer to the configurations where applied field H is respectively \parallel and \perp to the current I in the sample. The constant $\gamma = 3q^2/4$. q is defined from the magnetomechanical factor (g') as $g' \simeq 2(1 - q)$ [11]. $G' = 1.94$ for Gd [12]. It is clear from Eqns. 6.2 and 6.3 that if the $\text{AMR} = 0$, $\alpha = 1$ and $\alpha_T = 0$ there will be no domain

wall resistance contribution. A finite AMR thus plays a crucial role here. Measured MRs (in 2 configurations) and α derived from the AMR as a function of T are shown in FIG. 6.4. α reaches a high value for $T \ll T_C$.

The domain wall thickness thus can be related to the observed domain wall resistance using Eqn. 6.2 above through the relation (see Appendix-4):

$$\delta = k \frac{\varphi^2 \rho_0}{5wtR_W} \alpha_T \quad (6.4)$$

Where k is a correction factor arising from the nonlinear current flow in the constriction region and is given as:

$$k = \left(1 + \frac{\rho_0 \varphi^2 \alpha_T}{10R_W w^2 t} \right)^{-1} \quad (6.5)$$

The correction factor is close to unity and has shallow temperature dependence. It varies from 0.977 at $T = 100$ K to 0.952 at $T = 250$ K.

6.6. Anisotropy energy E_A calculation

Using the measured value of ρ_0 , α_T and R_W the value of the DW thickness (δ) is calculated as a function of T using Eqns. 6.4 and 6.5. The δ is shown in FIG. 6.4. In the same graph (inset curve C) we show the temperature dependence of the anisotropy energy E_A as obtained from Eqn. 6.1 using the value of δ . At low temperature δ rises sharply and above 170 K ($= 0.58 T_C$) it becomes nearly independent of temperature with value around 30 nm.

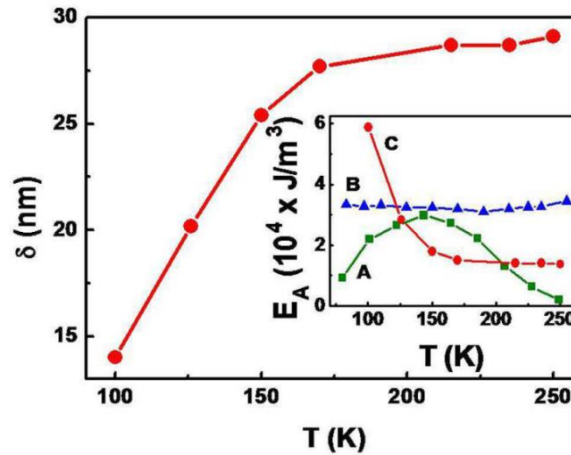


FIG. 6.5. The DW thickness δ as a function of T as measured from the experiment. The graph shows the temperature variation of the anisotropy energy E_A as obtained from the measured value of δ . The inset shows the E_A of Gd as a function of T as obtained from magnetocrystalline anisotropy for a polycrystalline sample (A) (using the relation $E_A = k_1/2 + 3k_2/8$ and obtaining the value of k_1 and k_2 from previous report [13]) and that measured from switching fields (B) ($H_S = E_A/M_S$) seen previously [14] along with E_A measured in the present study (C).

The anisotropy energy E_A shows strong temperature dependence at low T . It has a low value of $\approx 10^4$ J/m³ from T_C down to about 170 K. Below 170 K, E_A sharply rises and at $T = 100$ K, the value of $E_A \approx 6.1 \times 10^4$ J/m³. For Gd nanowire (diameter = 100 nm) where the anisotropy is fixed predominantly by the uniaxial shape anisotropy, a value of $E_A \approx 3.4 \times 10^4$ J/m³ at 100 K has been measured from switching fields as observed from low field MR experiments [14]. The value obtained from our experiment is somewhat larger but is similar in magnitude to the value seen in a 100 nm nanowire (inset curve B). Interestingly, for Gd the intrinsic

anisotropy energy depends on the crystallographic axis and in single crystal Gd it shows a spin reorientation transition at $T = 235$ K where $E_A = 0$. For polycrystalline Gd, when an average is made over different axes E_A shows temperature dependence as depicted in FIG. 6.5 inset (curve A). The value of E_A obtained by us for the NC is similar order but is larger than that expected from the intrinsic single ion anisotropy energy. The E_A in our case will be dominated by such factors as size and shape anisotropy along with the intrinsic anisotropy. The method depicted here, that the DW resistance can be measured and utilized effectively to find E_A , is thus established as a method to find E_A in thin films where a DW can be tagged to a constriction in the film.

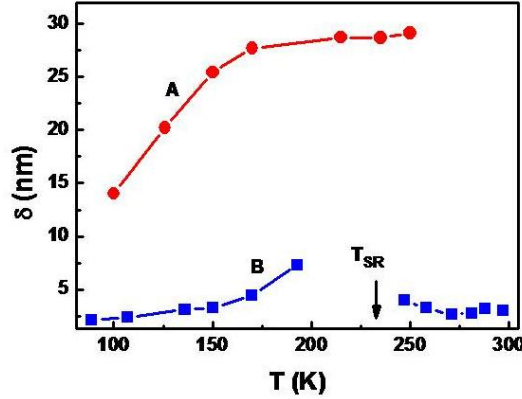


FIG. 6.6. The DW thickness δ as a function of T which is measured in this work for a NC of Gd (A). DW thickness δ of a single crystal Gd sample (B) [15]. Spin reorientation temperature T_{SR} is indicated by arrow.

In FIG. 6.6 we are comparing our result with a previous work on single crystal Gd sample. The δ of a single crystal sample is nearly 5 times smaller than the δ of a nanoconstriction (NC). At the spin reorientation temperature (T_{SR}) $E_A \rightarrow 0$ for a single crystal bulk Gd sample where E_A is mainly governed by the magnetocrystalline anisotropy. Since $\delta \propto 1/\sqrt{E_A}$, at T_{SR} domain wall thickness δ for a bulk sample diverges. This phenomenon completely vanishes in the NC sample where E_A is mainly dominated by the shape anisotropy which does not become 0 at T_{SR} and has a weak temperature dependency.

6.7. Conclusion

To summarize, we show that a current induced DW motion can be seen in a NC made on a microstrip of 4f metal Gd where the critical current density for inducing the DW motion was found to be similar to that seen in Ni and Permalloy although the magnetism in Gd is very different from that of conventional 3d metals. Since Gd has a low T_C we could also study the temperature evolution of the domain wall resistance, the critical current and also the domain wall width. We have also utilized the knowledge of domain wall thickness to find the evolution of the anisotropy energy as a function of T in Gd.

References

1. S. Lepadatu, Y. B. Xu and E. Ahmad, *J. Appl. Phys.*, **97**, 10C711 (2005).
2. S. Lepadatu and Y. B. Xu, *Phys. Rev. Let.*, **92**, 127201(2004).
3. P. P. Freitas and L. Berger, *J. Appl. Phys.*, **57**, 1266(1985).
4. L. Berger, *J. Appl. Phys.*, **55**, 1954 (1984).
5. *Handbook of Magnetism and Advanced Magnetic Materials* edited by Helmut Kronmüller and Stuart Parkin (John Wiley and Sons, Volume 2: Micromagnetism, 2007).
6. José L. Prieto, Mark G. Blamire and Jan E. Evetts, *Phys. Rev. Let.*, **90**, 027201 (2003).
7. Serban Lepadatu, Jill Claydon, David Ciudad, Adam Naylor, Christy Kinane¹, Sean Langridge, Sarnjeet Dhesi and Christopher Marrows, *Appl. Phys. Express.*, **3**, 083002 (2010).
8. Peter M. Levy and Shufeng Zhang, *Phys. Rev. Let.*, **79**, 5110 (1997).
9. *Physics of Ferromagnetism* edited by Sōshin Chikazumi (Oxford University Press, Second Edition, 1999).
10. Isao Mannari, *Prog. Theo. Phys.*, **22**, 335 (1959).
11. I. A. Campbell, A. Fert and O. Jaoul, *J. Phys. C: Solid State Phys.*, **3**, S95 (1970).
12. Arthur F. Kip, *Rev. Mod. Phys.*, **25**, 229 (1953).
13. C. D. Graham, JR., *J. Appl. Phys.*, **34**, 1341 (1963).
14. Manotosh Chakravorty and A. K. Raychaudhuri, *J. Appl. Phys.*, **115**, 054308 (2014).
15. R. L. Smith, W. D. Corner and B. K. Tanner, *J. Magnetism and Magnetic Material*, **20**, 265 (1980).

CHAPTER 7

Size induced change of compensation temperature in Gd_xCo_{1-x} ($x = 0.4$) alloy nanowire (diameter ~100 nm)

Binary alloy of Gadolinium (Gd) and Cobalt (Co) with 40% Gd composition was prepared in the form of bulk and nanowire. The Nanowires were fabricated within the pores of an Anodic Aluminium Oxide (AAO) template by Electrochemical deposition technique. Magnetic measurements up to a field of 1.6T and in temperature range 80 K to 1100 K were done. In the temperature range 80 K to 1100 K multiple magnetization compensation temperatures were observed. It has been observed that in the nanowire the compensations temperatures (T_{cm}) are severely modified and shifted to higher temperatures by 100's of Kelvin when compared to those of the bulk alloy. From magnetic measurements the Anisotropy energy E_A was determined as a function of temperature. It has been proposed that the upward shift of T_{cm} 's in nanowire is linked to the temperature derivative of E_A which becomes softer due to larger contribution of temperature independent size/shape anisotropy compared to the magentocrystalline anisotropy that dominates in the bulk.

7.1. Introduction

Alloying of Rare-earth (RE) and 3d transition metals (TM) show exotic magnetic order like ferrimagnetism with compensation temperature. For instance, when Co is alloyed with Gd, the RE-TM coupling becomes strongly anti-ferromagnetic [1]. This leads to ferrimagnetic order with well-defined compensation temperature (T_{cm}) where the total magnetization becomes a minimum. The value of T_{cm} depends on the relative compositions of Gd and Co. [2]. There is a wide range of application of Gd-Co binary alloys. Gd rich alloys ($Gd_{0.75}Co_{0.25}$, $Gd_{0.65}Co_{0.35}$) and intermetallic compounds (Gd_3Co_4 , Gd_4Co_3) [3-5] has a very high magneto caloric effect (MCE) which could be used in magnetic refrigeration process. In these materials the Néel temperature (T_N) or Curie temperature (T_C) is observed in place of T_{cm} . The Co rich compositions are greatly used for magneto-optical devices [2]. Due to its large spin polarization, the compensated composition of Gd-Co is used in multilayer giant magnetoresistance (GMR). For temperature (T) below and above T_{cm} the alloy shows negative and positive GMR effect [1,6]. The Hall effect measurement of the TM rich $GdCo_3$ and $Gd(Co_{0.25}Ni_{0.75})_3$ showed that the Hall voltage is associated with the Co moment and at T_{cm} the sign of Hall resistance is sharply changed [7].

Recently different interface engineering showed that Gd which has low work function ($\phi_m = 3.5$ V), could be used in the spintronic devices for complete removal of Schottky barrier. Due to its large tunnel spin polarization (TSP) and low ϕ_m value if the contact pads of the Si-spintronic device is modified as Ferromagnet/Gd/Insulator/Si, the RA product (contact resistance \times contact area) decreases 10^8 times for a Gd film of thickness larger than 1 nm [8, 9].

The ϕ_m value of Gd-Co alloy can be tuned by tuning the composition. If we use this alloy in place of Gd, the TSP increases at high temperature [9] and the device could be used above room temperature. Recently theoretical reports showed that the T_{cm} value of binary alloys can be shifted to high temperature by increasing its anisotropy energy (E_A) [11,12]. Also in the low dimension structure the shape anisotropy (E_k) dominates over magnetocrystalline anisotropy (E_{mc}) and the overall $E_A (= E_k + E_{mc})$ value increases due to larger contribution by E_k . Therefore, if we use low dimension structure of GdCo alloy like nanowires, in spintronic devices, it is possible to shift T_{cm} at further high temperature and the device could be used at very high temperature with large TSP value. With this motivation we explored whether nanowires of Gd-Co alloys can have higher T_{cm} . As described in details below, we find that this indeed is the case that the T_{cm} in nanowires are much larger compared to those of bulk alloys of same compositions. In fact the shift in T_{cm} can even be termed “spectacular” as we will observe below.

In this investigation we have chosen the composition Gd_xCo_{1-x} with $x = 0.4$, which has a T_{cm} nearly 200 K higher than the room temperature [2]. To study further increment of T_{cm} in nanodimensions, we prepared two samples of different sizes but with same composition. One is a bulk material and another one is an array of nanowire (NW) which was prepared by electrochemical method. The magnetization (M) of both the samples has been studied and the T dependent anisotropy energy (E_A) was estimated from M . In our knowledge this is the first work where magnetization behaviour of GdCo alloy NW has been studied rigorously to high enough temperatures. The observations have been made for a very wide range of temperature (from 80 K to 1100 K).

7.2. Experimental

The measurements have been done on two samples. One was the array of $Gd_{0.4}Co_{0.6}$ alloy nanowires with diameter ~ 100 nm and length ~ 50 μm . The sample is mentioned as “NW” and it was prepared by electrochemical deposition technique within Anodic Aluminium

Oxide (AAO) template using three electrodes. The pore diameter of the AAO template used was 100 nm. This technique was elaborately described in chapter-2. Platinum (Pt) plate was used as counter electrode (anode) and Hg/HgCl₂ was used as a reference electrode. In previous works by organic electrolyte was used to prepare this alloy NW [13]. But in that case the Gd content becomes very small. In our case we used inorganic electrolyte which contained 0.2 M GdCl₃, 7H₂O and 0.2 M CoSO₄, 5H₂O. By adding 0.3 M H₃BO₃ the pH of the electrolyte was maintained at 3.5. Best deposition occurred at this pH value.

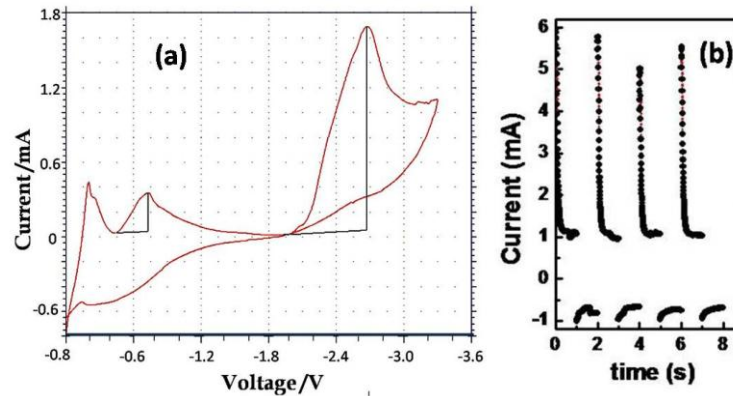


FIG. 7.1. (a) Cyclic voltammetry curve of GdCo NW deposition. (b) XRD of both the samples. (b) Pulse current vs. time for NW preparation.

The Cyclic voltammetry (CV) curve shows a peak at -2.5 V and this is the oxidation potential to prepare Gd_{0.4}Co_{0.6} alloy nanowire inside the AAO template. The electrochemical deposition has been done at -2.5 V. Here pulse deposition technique was used with a pulse width of 1 s. A 50% duty cycle was used. For deposition potential within the range of 0 V to -2 V, GdCo oxide NW forms preferably. As the potential increases above -2 V the Gd content increases. At this electrolyte solution -2.5 V is the appropriate deposition potential for preparation of a 100 nm diameter NW with 40 % Gd content.

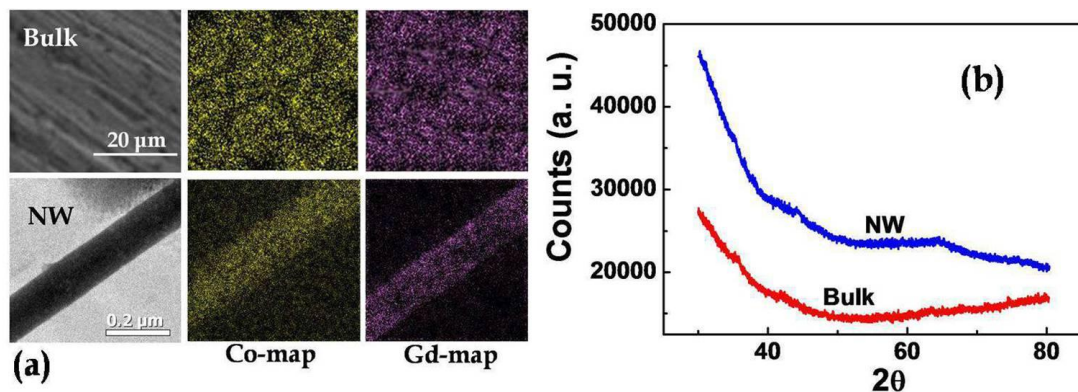


FIG. 7.2. (a) SEM image for the surface of Bulk sample and TEM image of a single nanowire. Co and Gd elemental mapping of the samples using EDX. (b) XRD of both the samples.

A bulk sample of Gd_{0.4}Co_{0.6} alloy with dimension $0.8 \times 1.2 \times 4.8$ mm³ was also prepared by arc melting. This sample was prepared by a mixture of Gd and Co in ratio 2:3 in an arc furnace. Ingots of Gd and Co with a purity of 99.99 % were used. The metal base of the chamber which acts as an anode was cooled by a continuous water flow. Two sharp tip Tungsten rods were used as a cathode. At first the chamber was made vacuum at an air

pressure of 10^{-2} mbar. After that 1 mbar Argon (Ar) gas was put inside the chamber. This Ar was used to create the arc (luminous electric discharge) which simultaneously melt the ingots and made the alloy. This process of melting was repeated three times to make homogeneous mixing of the elements inside the sample. To make further homogeneous mixing, the sample was annealed for 24 hours at 600°C in a sealed quartz tube which contains 0.1 mbar Ar.

The elemental analysis has been done by using energy dispersive X-ray (EDX) spectroscopy in a Transmission Electron Microscope (TEM) for NW sample and Scanning Electron Microscope (SEM) for the Bulk. The data show that the Gd Atomic% for Bulk and NW are 39.4 ± 4.8 and 42.1 ± 6.3 respectively. This result confirms that the concentration of Gd in both the samples are nearly equal and it is $x = 0.4$. The elemental mapping (spot EDX) in SEM and TEM confirms the uniform distribution of Co and Gd throughout the surface of bulk and nanowire (FIG. 7.2(a)). TEM image shows that the diameter of a single nanowire is ~ 100 nm. X-ray diffraction (XRD) pattern for Bulk and NW (FIG. 7.2(b)) shows that the samples are amorphous in nature.

7.3. Magnetization

All magnetic measurements have been done in a Vibrating Sample Magnetometer (VSM) for a temperature range 80 K to 1100 K with magnetic field range up to 1.6 T in a continuous Ar flow of 0.1 mbar pressure.

7.3.1. Temperature dependence of magnetization: $M(T)$ vs. T

In FIG. 7.3 the T dependence of low field (10 mT) magnetization (M) and its derivative for Bulk and NW are plotted. The magnetization is normalized as $m = M/M_{80}$ where M_{80} is the value of M at 80 K. For the NW sample, the field was applied parallel to the nanowire axis or c-axis.

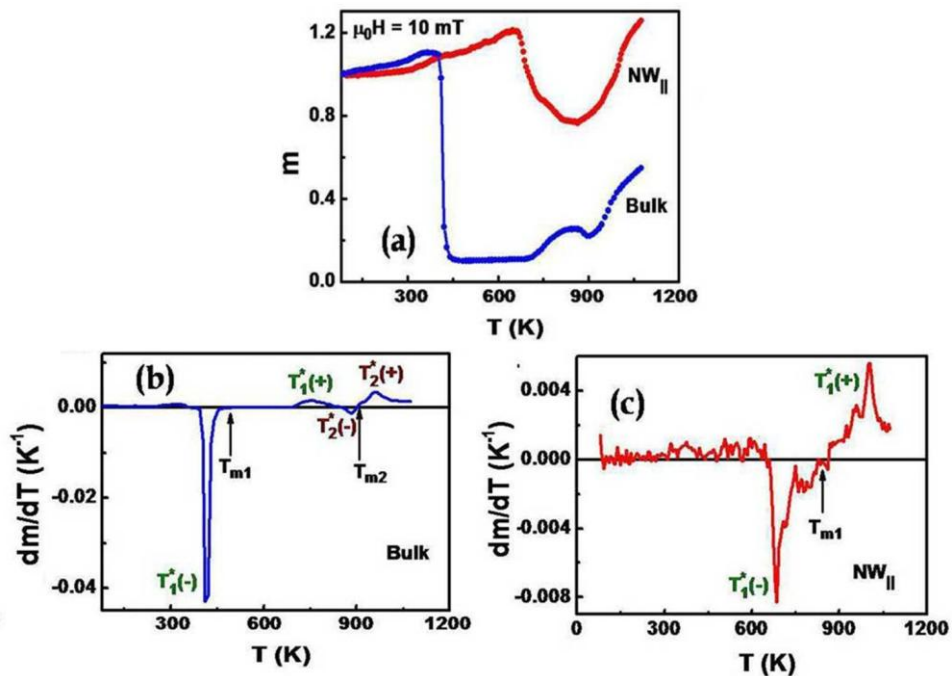


FIG. 7.3. (a) Temperature (T) dependence of the normalized magnetization $m(=M/M_{80})$ for bulk and nanowire samples. The applied field is $\mu_0 H = 10$ mT and for NW it is applied parallel to the wire axis. T dependence of dm/dT for (b) Bulk and (c) NW. Two phase transition temperatures (T_{m1} , T_{m2}) and the spin reorientation temperatures ($T^*_1(-)$, $T^*_1(+)$, $T^*_2(-)$ and $T^*_2(+)$) are indicated by arrows.

There are two minima in the $m - T$ curve of bulk sample. These minima are defined by the temperatures T_{m1} and T_{m2} at which $dm/dT = 0$. Below and above T_m s the magnetization is sharply changed which is defined by the sharp minima and maxima in the derivative curve. These temperatures are mentioned as $T^*(-)$ and $T^*(+)$ within which the magnetization strongly depends on temperature. In a ferrimagnet there is a temperature where the magnetization of each sub-lattices are arranged in such a way that the total magnetization becomes minimum. This temperature is called magnetization compensation temperature (T_{cm}). Therefore in our sample the T_m s can be the magnetization compensation temperatures. Later on in discussion section we did provide confirmation that T_m s are the T_{cm} s. The different magnetic regions which are separated by T_m s are defined as $P_1 (T < T_{m1})$, $P_2 (T_{m1} < T < T_{m2})$ and $P_3 (T > T_{m2})$. Within the temperature range 80–1100 K in Bulk two transition temperatures ($T_{m1} \approx 490$ K and $T_{m2} \approx 900$ K) are observed where in NW only one ($T_{m1} \approx 850$ K) is present. From this result it is clear that in NW either T_{m1} is shifted to the higher value or T_{m2} is shifted to the lower value. This issue will be resolved later on through measurements of the coercive field H_C and the saturation magnetization M_S .

7.3.2. Magnetic Field dependence of M

The magnetization (M) of the bulk sample was measured by applying a field ($\mu_0 H$) along the length of the Bulk sample. For the magnetic measurement of NW we used $3 \times 5 \text{ mm}^2$ AAO template (one side Ag coated) where the nanowires were present inside the nano channels. The mass of the Ag coated bare template (before deposition of nanowire) was 0.9 mg and after deposition it was 3.7 mg. Therefore the total mass of the nanowires which was used in the magnetization measurement was 2.8 mg. Using the value of mass density (9.56 g/cm^3 , measured from bulk) the total volume of the nanowires was calculated. M was measured for two different field directions which were mentioned in this work as NW_{\parallel} (H parallel with c-axis or nanowire axis) and NW_{\perp} (H perpendicular with c-axis).

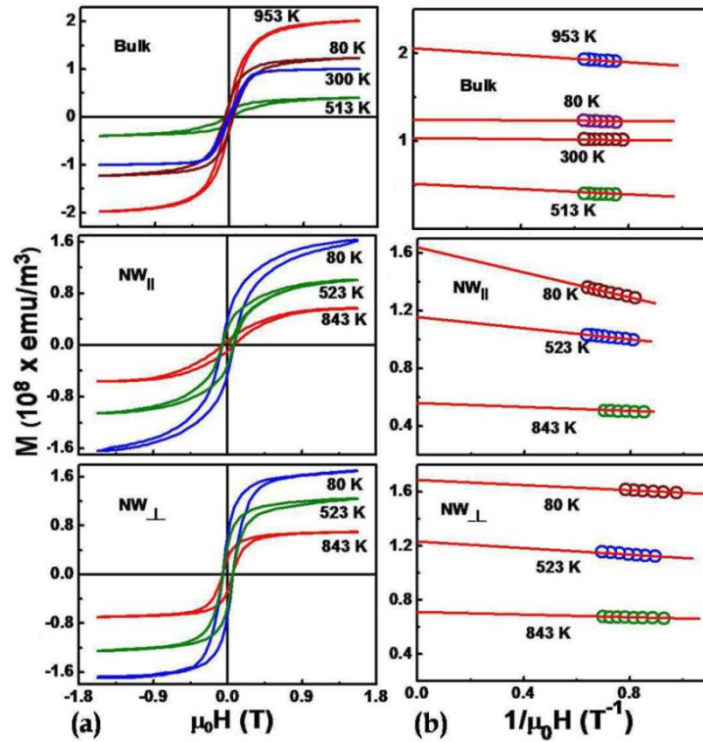


FIG. 7.4. (a) Field ($\mu_0 H$) dependence of M for Bulk, NW_{\parallel} and NW_{\perp} . Field applied parallel and perpendicular to the nanowire axis are indicated by \parallel and \perp sign. (b) M vs. $1/\mu_0 H$ plot for different temperatures. Solid lines are the linear fit of the data to find the value of saturation magnetization (M_S).

The field ($\mu_0 H$) dependence of the magnetization (M) of Bulk and NW sample at different temperatures showed that the hysteresis loop has a finite value of coercive field H_C which is larger in NW than that in the Bulk. At all the temperatures the technical saturation of M occurs for a field > 1 T for all the samples (FIG. 7.4(a)). The saturation magnetization (M_S) was defined from the $M-H$ loop. The linear fit of M vs. $1/\mu_0 H$ curve gives a measure of the saturation magnetization (M_S) where $1/\mu_0 H = 0$ (FIG. 7.4(b)).

7.3.3. Saturation magnetization M_S and Coercive field H_C

FIG. 7.5(a) shows the temperature (T) dependence of saturation magnetization (M_S) of Bulk and NW. Within the temperature range 80 K to 370 K, M_S for Bulk sample slowly decreases from 1.2×10^8 emu/m³ to 0.86×10^8 emu/m³. Above this temperature M_S sharply decreases to 0.44×10^8 emu/m³ ($T \sim 475$ K). Within the temperature range 475 K to 900 K, M_S is small enough and is nearly independent of temperature. For further increase of temperature M_S sharply jumps to a value of 1.98×10^8 emu/m³ at 950 K.

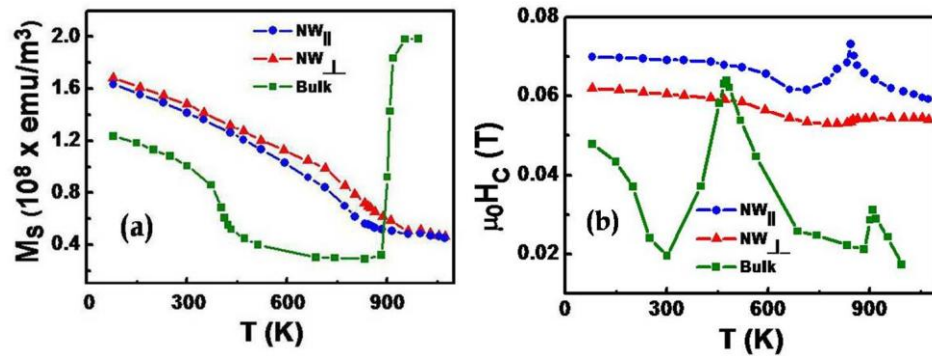


FIG. 7.5. T dependence of (a) saturation magnetization (M_S) and (b) coercive Field ($\mu_0 H_C$).

The resultant magnetization ($\vec{M}_S = \vec{M}_{Co} + \vec{M}_{Gd}$) is highly dependent on temperature through the temperature dependence of angle ($\theta(T)$) between the vectors \vec{M}_{Co} and \vec{M}_{Gd} . For $\theta = 0$, the subatomic magnetization vectors are parallel to each other and M_S becomes maximum.

In contrast to bulk sample in NW, M_S is gradually decreases. The value of the change M_S is always larger in NW_⊥ than NW_{||}, of temperature. At T_m the slope of M_S-T curve shows accelerated suddenly changes.

The coercive field (H_C) vs. temperature curve shows that the bulk sample has two sharp peaks at the transition temperatures T_{m1} and T_{m2} . In NW within the experimental temperature window only one transition is present and therefore it has only one peak in the H_C-T curve. For the condition field parallel to the nanowire axis (NW_{||}) only shows a sharp peak. For field perpendicular to the axis (NW_⊥) shows a little hump at T_{m1} . The coercive field H_C has a dependence on the saturation magnetization M_S and the anisotropy energy E_A as $H_C \propto (E_A/M_S)$. This relation is a very good indicator of finding the magnetization compensation temperature (T_{cm}) where the magnetization (M) has a minimum value. If E_A does not have a strong variation with temperature, at T_{cm} magnetization becomes minimum and in the H_C-T curve, H_C shows a sharp peak [14]. Therefore to understand the nature of the transitions at T_{m1} and T_{m2} (either it is T_{cm} or not) the value of E_A of our sample must be determined.

7.3.4. Angular dependence of $M-H$ curve in nanowires

The values of M_S and H_C of the NW for two field orientations parallel to the NW (NW_{||}) and perpendicular to the NW (NW_⊥) are different. By applying the magnetic field at

different angle ϕ with the nanowire axis we determine the magnetic easy direction of NW.

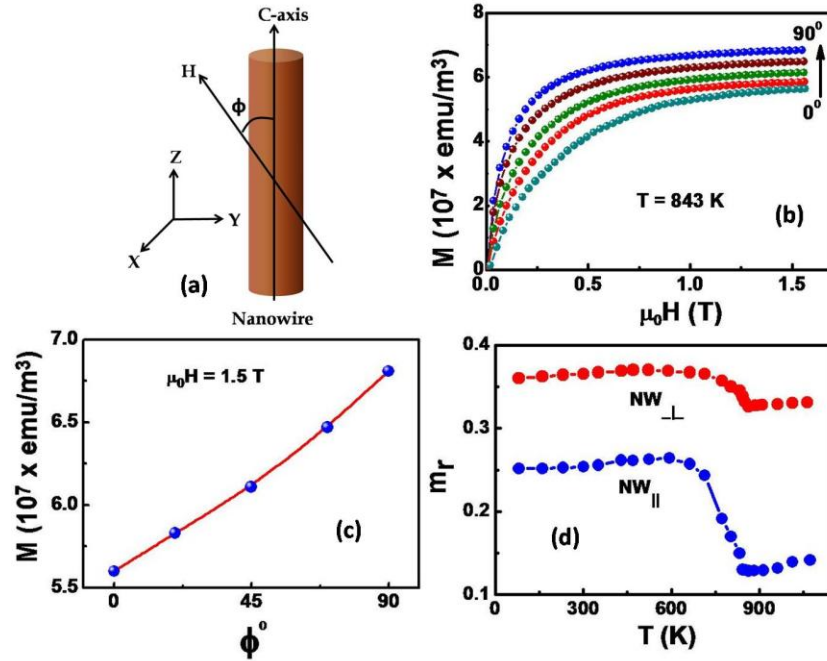


FIG. 7.6. (a) Schematic diagram of field direction and nanowire axis or c-axis. (b) Field (μ_0H) dependence of M of NW for different field angle ϕ (angle between H direction and c-axis) from 0° to 90° at 843 K (near T_{ml} of NW). (c) M vs. ϕ for field 1.5 T. (b) Temperature variation of the retentivity (m_r) of NW for both \parallel and \perp conditions.

The $M-H$ for \perp ($\phi = 90^\circ$) condition is always sharper than the \parallel ($\phi = 0^\circ$) condition. The magnetization depends on the angle (ϕ) between applied field (H) and c-axis or nanowire axis (FIG. 7.6(a)). The value of M is maximum for $\phi = 90^\circ$ (FIG. 7.6(c)). Therefore if c-axis is parallel to the z-axis, the easy direction of magnetization is in the x-y plane. It can clearly understand from the T dependent retentivity ($m_r = M(H=0)/M_S$) curve of the NW (FIG. 7.6(c)) where m_r for \perp condition is always higher than the \parallel condition.

In the array of nanowire system due to the dipolar interaction between nearest neighbour nanowires where each nanowire approximates as a dipole the anisotropy field H_{xy} and H_z can be expressed as [15],

$$H_{xy} = H_{mc} + 2.1 \frac{M_S V}{D^3} \quad (7.1)$$

$$H_z = H_k - 4.2 \frac{M_S V}{D^3} \quad (7.2)$$

, where H_{mc} and H_k are the magnetocrystalline and shape anisotropy field respectively. H_k is much larger than H_{mc} in the nanowire. M_S is the saturation magnetization and V is the volume of a nanowire. Here one assumption has been made that the volume is same for all the nanowires. D is the inter-wire distance. Now as the aspect ratio of the nanowire increases, V increases and due to the negative signs in Eqn. 7.2 H_z decreases. There is a crossover value of the aspect ratio (AR) above which H_{xy} becomes larger than H_z . There was an example of a past work [15] which showed that the crossover value of the AR of 150 nm diameter Co nanowire is nearly ~ 315 . In our GdCo NW sample (diameter ~ 100 nm) AR ~ 500 . Therefore it is larger than the crossover value of the AR of the common magnetic materials like Co. For this large AR the NW sample has an

easy direction of magnetization along the x - y plane or $H_{xy} > H_z$. It is for this reason, M is maximum at $\varphi = 90^\circ$ and m_r for \perp condition is always higher than the \parallel condition.

7.4. Anisotropy energy E_A calculation

To confirm the nature of the transitions at T_m s, anisotropy energy (E_A) determination is important. The relation between coercive field (H_C), anisotropy field (H_A) and demagnetization field (H_D) is given as, $H_C = \Gamma H_A - H_D$ [16]. Γ is the micro-structural parameter and for a non-ideal micro-structure of a real magnet $\Gamma = 0.16$ [17]. $H_A = 2E_A/\mu_0 M_S$ [18] and $H_D = NM_S/\mu_0$. N is the effective demagnetization factor. Therefore,

$$H_C = \frac{2\Gamma E_A}{\mu_0 M_S} - \frac{NM_S}{\mu_0}$$

or,

$$E_A = \frac{1}{\Gamma} \left[\frac{1}{2} \mu_0 H_C M_S + \frac{1}{2} NM_S^2 \right] \quad (7.3)$$

The value of N completely depends on the shape of the sample. The applied magnetic field direction also plays a role here. In case of Bulk sample the field H is applied along the width of the rectangular shape (see FIG. 7.7(a)) and N for Bulk becomes 0.372 [19]. N for \parallel to the c -axis (z -axis) of a cylinder of radius R and length L becomes $N_Z = (L + R - \sqrt{L^2 + R^2})/L$ and for \perp to the c -axis (x or y -axis) it becomes $N_X = N_Y = (1 - N_Z)/2$ [20] (see FIG. 7.7(b)). For a nanowire of length 50 μm and radius 50 nm $N_Z = 0.00099$ and $N_X = N_Y = 0.4995$. In our case for field applied \parallel and \perp to the c -axis of nanowire $N = N_Z$ and N_X respectively in Eqn. 7.3.

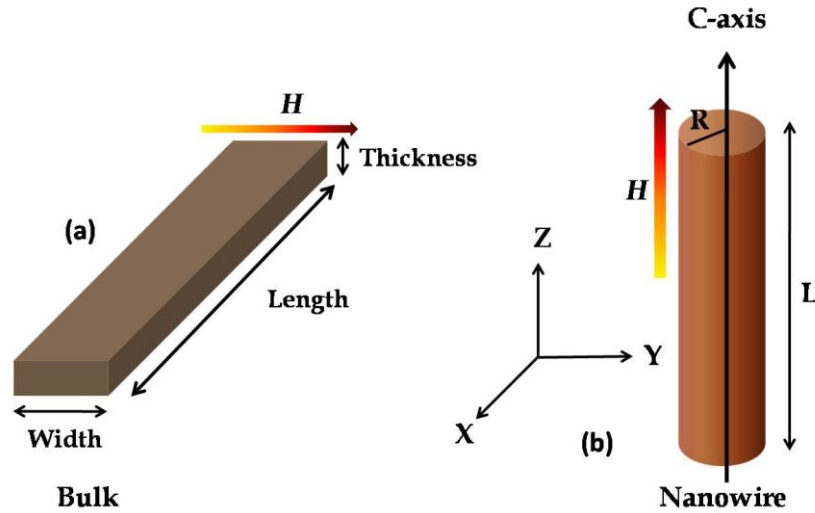


FIG. 7.7. Schematic diagram of magnetic field direction in (a) Bulk and (b) NW sample. In nanowire the field is applied in the \parallel condition or along the z -axis. L and R are the length and radius of the cylindrical nanowire.

In FIG. 7.8 the E_A evaluated by Eqn. 7.3 and experimentally measured values of physical parameters are shown for both Bulk and NW. Above 150 K E_A is larger in NW than that in Bulk till $T \sim 900$ K. At 300 K E_A for Bulk ($2 \times 10^4 \text{ J/m}^3$) is nearly comparable with that reported in the previous work [21] where for this composition at room temperature value of

$E_A = 3 \times 10^4 \text{ J/m}^3$. In case of NW due to the dipolar interaction of nanowire arrays E_A for \parallel condition is always larger than the \perp condition and the separation increases with the decrease of temperature.

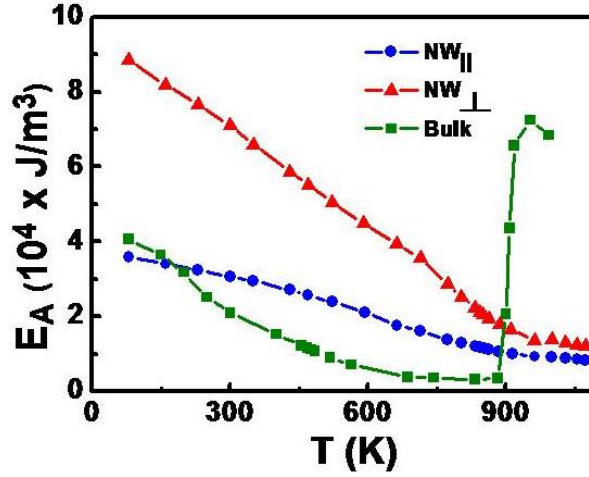


FIG. 7.8. Temperature (T) dependence of E_A for bulk and nanowire. NW_{\parallel} and NW_{\perp} indicate the field direction along \parallel and \perp to the nanowire axis.

At the first transition temperature $T_{m1} \sim 490 \text{ K}$ of Bulk, the derivative of E_A-T curve ($dE_A/dT \approx -43.91 \text{ Jm}^{-3}\text{K}^{-1}$) is negative and is much smaller compared with the same derivative ($dE_A/dT \approx 2535 \text{ Jm}^{-3}\text{K}^{-1}$) which is positive at the second transition temperature $T_{m2} \sim 900 \text{ K}$. Therefore at T_{m1} the condition, $H_C M_S \propto E_A \approx \text{constant}$, is nearly satisfied and it could be considered as magnetization compensation temperature T_{cm} [14]. The second transition temperature T_{m2} is likely not a compensation temperature and it may be a phase transition temperature where the magnetic spin orientation of the sub atomic moment suddenly changes.

In NW at the transition temperature $T_{m1} \sim 850 \text{ K}$ the slope ($dE_A/dT \approx -25.89 \text{ Jm}^{-3}\text{K}^{-1}$) is also of the same order of the slope of E_A-T curve of the bulk sample at T_{m1} . Therefore the transition in NW is also the magnetization compensation temperature T_{cm} . From the above discussion it is concluded that the first transition of bulk sample is a T_{cm} which is shifted to the higher temperature in the nanowire sample. T_{m2} has not been observed within the temperature window of the measurements. Either it occurs at a higher temperature or the large value of shape anisotropy suppresses the spin orientation as has been seen in earlier chapters for the spin reorientation transition in NWs.

7.5. Discussion

To find the reason of the shifting of T_{cm} in NW sample we investigate the total magnetization M . For the binary alloy of Gd and Co with concentration λ and μ , the magnetization is given as:

$$M = \frac{\lambda M_{Gd} + \mu M_{Co}}{\lambda + \mu} \quad (7.4)$$

, where $\lambda + \mu = 1$. The sub-lattice magnetizations of Gd and Co are represented by M_{Gd} and M_{Co} respectively. The magnetization of each sub-lattice can be expressed as $M_{Gd} \propto B_J \left(\frac{\epsilon_{Gd} + E_A + M_{Gd} H}{k_B T} \right)$ and $M_{Co} \propto B_J \left(\frac{\epsilon_{Co} + E_A + M_{Co} H}{k_B T} \right)$, where ϵ_{Gd} and ϵ_{Co} are the net exchange interaction energy of Gd atom ($\epsilon_{Gd} = \epsilon_{Gd-Gd} + \epsilon_{Gd-Co}$) and Co atom ($\epsilon_{Co} = \epsilon_{Co-Co} +$

ε_{Co-Gd}) respectively. $B_j(x)$ is the Brillouin function of x . For a low value of applied field $\varepsilon_{Gd} + E_A \gg M_{Gd}H$ and $\varepsilon_{Co} + E_A \gg M_{Co}H$. Therefore x could be approximated as, $x = (\varepsilon + E_A)/k_B T$. The lattice distances between Gd and Co atoms are as follows, $d_{Co-Co} \approx 2.4 A^0$, $d_{Gd-Co} \approx 2.9 A^0$ and $d_{Gd-Gd} \approx 3.5 A^0$ [3]. Therefore we consider the average unit cell volume as, $[(d_{Co-Co} + d_{Gd-Co} + d_{Gd-Gd})/3]^3 = 2.7 \times 10^{-30} m^3$. At T_{cm} (= 490 K) of Bulk where $E_A \approx 1.088 \times 10^4 J/m^3$ the anisotropy energy within a unit-cell becomes $2.9 \times 10^{-26} J$. Also the exchange interactions are $\varepsilon_{Co-Co} \approx 2 \times 10^{-21} J$, $\varepsilon_{Gd-Co} \approx 2 \times 10^{-22} J$ and $\varepsilon_{Gd-Gd} \approx 3 \times 10^{-23} J$ [22]. Therefore the value of ε_{Gd} and ε_{Co} becomes $\varepsilon_{Gd} = 2.3 \times 10^{-22} J$ and $\varepsilon_{Co} = 2.2 \times 10^{-21} J$. Therefore at T_{cm} the value of $x_{Gd} \approx \frac{2.3 \times 10^{-22} + 2.9 \times 10^{-26}}{1.38 \times 10^{-23} \times 490} \approx 0.034$ and $x_{Co} \approx \frac{2.2 \times 10^{-21} + 2.9 \times 10^{-26}}{1.38 \times 10^{-23} \times 490} \approx 0.33$.

Similarly for NW with $E_A \approx 1.187 \times 10^4 J/m^3$ at $T_{cm} = 850$ K the value of x becomes $x_{Gd} \approx \frac{2.3 \times 10^{-22} + 3.2 \times 10^{-26}}{1.38 \times 10^{-23} \times 850} \approx 0.019$ and $x_{Co} \approx \frac{2.2 \times 10^{-21} + 3.2 \times 10^{-26}}{1.38 \times 10^{-23} \times 850} \approx 0.187$.

Therefore for the small values of x ($\ll 1$) the Brillouin function for both the samples becomes $B_j(x) \propto x$. From Eqn. 7.4 the magnetization M can be approximated as,

$$\begin{aligned}
 M &= A_1 B_j(x_{Gd}) + A_2 B_j(x_{Co}) \\
 &\text{or,} \\
 M &\approx A_1 x_{Gd} + A_2 x_{Co}
 \end{aligned} \tag{7.5}$$

, where A_1 and A_2 are the constants.

$$\begin{aligned}
 M &= A_1 \left(\frac{\varepsilon_{Gd} + E_A}{k_B T} \right) + A_2 \left(\frac{\varepsilon_{Co} + E_A}{k_B T} \right) \\
 M &= B_1 \left(\frac{E_A}{T} \right) + B_2 \left(\frac{1}{T} \right)
 \end{aligned} \tag{7.6}$$

, where $B_1 = (A_1 + A_2)/k_B$ and $B_2 = (A_1 \varepsilon_{Gd} + A_2 \varepsilon_{Co})/k_B$ are independent of temperature. The only temperature dependence arises from that of the Anisotropy energy E_A .

At the compensation temperature T_{cm} , M is minimum and $\left(\frac{dM}{dT} \right)_{T_{cm}} = 0$. Therefore from Eqn.

7.6 a relation could be established as,

$$T_{cm} \left(\frac{dE_A}{dT} \right)_{cm} = (E_A)_{cm} + c \tag{7.7}$$

, where $c = B_2/B_1$ is a constant. The table 7.1 below gives a summary of the values of the relevant parameters.

Table 7.1: E_A and dE_A/dT of Bulk and NW at T_{cm} .

Sample-ID	T_{cm} (K)	$(E_A)_{cm}$ ($10^4 \times Jm^{-3}$)	$(dE_A/dT)_{cm1}$ ($Jm^{-3}K^{-1}$)	λ ($10^4 \times Jm^{-3}$)
Bulk	490	1.018	-43.91	-2.152
NW	850	1.187	-25.89	-2.158

Note: T_{cm} is experimentally determined and $(E_A)_{cm}$, $(dE_A/dT)_{cm1}$ and λ are measured.

$(E_A)_{cm}$ for NW and Bulk are nearly same (Table 7.1). The ratio c being determined by atomic level parameters is independent of the sample size/shape. Thus according to Eqn. 7.7, the parameter $\lambda = T_{cm} \times \left(\frac{dE_A}{dT} \right)_{cm}$ must be same for both the samples. Table 7.1 shows that our experimental result satisfies Eqn. 7.7.

In nanowire the shape and surface disorder anisotropy energy E_k is larger than the magnetocrystalline anisotropy energy E_{mc} . In nanowire $E_A \approx E_k$ and since E_k has a weak T dependency, dE_A/dT of nanowire is smaller than the bulk sample. E_{mc} has strong temperature

dependence and therefore dE_A/dT has a large value in the bulk sample. In our sample at T_{cm} , the value of dE_A/dT becomes nearly half for NW than that in the Bulk and to make the value of λ same in both of them, T_{cm} of NW increases nearly two times compared to that of the Bulk. This result shows that the shifting of compensation temperature (T_{cm}) does not depend on the change of anisotropy energy (E_A) but mainly is contributed by the softer temperature derivative of E_A in the nanowire and constancy of the product $\lambda = T_{cm} \times \left(\frac{dE_A}{dT}\right)_{cm}$.

7.6. Conclusion

In this work we for the first time prepared GdCo alloy nanowires of Gd content 40% by electrochemical method. In this composition range the material is Ferrimagnetic as established in the bulk by previous studies. We measured magnetic field (0 to 1.6 T) and temperature (80 K to 1100 K) dependent magnetization of the ensemble of nanowire (by retaining them in the AAO template) and compared them with those of with bulk. In this composition one T_{cm} and another transition temperature T_{m2} were observed in the bulk. In nanowire E_k is larger than E_{mc} and because of that dE_A/dT is smaller in nanowires than bulk. Due to this reason T_{cm} is shifted to a higher value in nanowire than that in the bulk. This work shows that the ferrimagnetic phases of binary alloys are stabilized in nanodimensions. At very high temperature (> 900 K) a transition is observed in the bulk (T_{m2}). This transition appears to be a transition to a ferromagnetic phase where the sub-lattice magnetizations may become parallel to each other and resultant value increases enormously. In nanowire it may be shifted to higher temperature which is above our experimental range or it does not occur.

References

1. M. Binder, A. Weber, O. Mosendz, G. Woltersdorf, M. Izquierdo, I. Neudecker, J. R. Dahn, T. D. Hatchard, J.-U. Thiele, C. H. Back and M. R. Scheinfein, *Phys. Rev. B*, **74**, 134404 (2006).
2. P. Chaudhari, J. J. Cuomo and R. J. Gambino, *Appl. Phys. Lett.*, **22**, 337 (1973).
3. Ji. Liang Zhang, Zhi Gang Zheng, Wen Huan Cao and Chan Hung Shek, *J. Magnetism and Magnetic Material*, **326**, 157 (2013).
4. D. A. Shishkin, A. S. Volegov, S. V. Andreev and N. V. Baranov, *The Phys. of Metals and Metallography*, **113**, 460 (2012).
5. Ikuo Nakai and Tomoki Fukagawa, *J. of the Phys. Society of Japan*, **63**, 4550 (1994).
6. N. T. Nam and L. Ranno, *J. Magnetism and Magnetic Material*, **322**, 1428 (2010).
7. R. Asomoza, I. A. Campbell, H. Jouve and R. Meyer, *J. Appl. Phys.*, **48**, 3829 (1977).
8. Ron Jansen, *Nature mat.*, **11**, 400 (2012).
9. Byoung Chul-Min, Kazunari Motohashi, Cock Lodder and Ron Jansen, *Nature mat.*, **5**, 817 (2006).
10. Manotosh Chakravorty and A. K. Raychaudhuri, *J. Appl. Phys.*, **117**, 034301 (2015).
11. N. De La Espriella, C. A. Mercado and G. M. Buendía, *J. Magnetism and Magnetic Material*, **417**, 30 (2016).
12. N. De La Espriella Vélez, C. Ortega López and F. Torres Hoyos, *Revista Mexicana de Física*, **59**, 95 (2013).
13. S. Y. Liu, A. K. Soh, L. Hong and L. Lu, *J. Phys. Chem. C*, **113**, 16934 (2009).
14. D. J. Webb, A. F. Marshall, Z. Sun, T. H. Geballe and Robert M. White, *IEEE Trans. On Magnetics*, **24**, 588 (1988).
15. Bipul Das, K. Mandal, Pintu Sen, Asish Bakshi and Pradip Das, *Physica B*, **407**, 3767 (2012).
16. D. J. Sellmyer, M. Zheng and R. Skomski, *J. Phys.: Condens Matter*, **13**, R433 (2001).
17. Wen-Yong Zhang, Jiang Zhang, Zhao-Hua Cheng, Shao-Ying Zhang and Bao-Gen Shen, *J. Phys.: Condens. Matter*, **13**, 3859 (2001).
18. Manotosh Chakravorty and A. K. Raychaudhuri, *J. Appl. Phys.*, **115**, 054308 (2014).
19. Amikam Aharoni, *J. Appl. Phys.*, **83**, 3432 (1998).
20. *Demagnetization Fields*, G. M. Wysin, Kansas State University (2012), <http://www.phys.ksu.edu/personal/wysin>.
21. R. C. Taylor and A. Gangulee, *J. Appl. Phys.*, **47**, 4666 (1976).
22. R. C. Taylor and A. Gangulee, *J. Appl. Phys.*, **48**, 358 (1977).

Summary and conclusions of the thesis

Experimental contributions

1. An integrated lithography process was developed by which nanowire and nanoconstriction in a microwire of Gd films were prepared. It was a combination of photo, chemical and ion beam lithography. FIB system was used in this process. Gd films were grown by thermal or electron beam evaporation at a high temperature (> 300 °C). The grain size of the films was controlled by thermal annealing.
2. By electrochemical method inside the AAO template $\text{Gd}_{0.4}\text{Co}_{0.6}$ nanowires were prepared. The diameter and length of the nanowires were ~ 100 nm and ~ 50 μm . XRD showed that the nanowires were amorphous. The grown wires were also characterized by SEM and TEM.
3. Low field MR measurement setup was developed for low temperature measurement of Gd bulk, film and single nanowire sample. Magnet was calibrated by a flux meter and necessary computer programming has been done for automation of the systems.

Physics contributions

1. Low field MR basically depends on domain wall (DW) motion and the domain movement is controlled by the local anisotropic field (H_A). The MR is the reflection of temperature dependent E_A and it becomes maximum at SR transition. As the grain size decreases this feature gradually vanishes. The important observation studied here is that the evolution of the MR with grain size shows clear cross over from an intrinsic magnetocrystalline anisotropy dominated regime to a grain boundary spin disorder dominated regime.
2. Nearly similar result has been observed in one dimensional nanostructure Gd nanowire. Below the switching field H_S low field MR shows oscillatory behaviour which increases with temperature. These small oscillations can be manifestation of thermally induced de-pinning of domain walls and it decrease as the sample temperature is lowered. The important phenomena observed here is that in nanowire MR is governed by the shape anisotropy and disorder. Magnetocrystalline anisotropy appears not to play an important role on MR in this case.
3. In this thesis we investigated what is the effect of the size of system on magnon BEC in Gd. We find that the occurrence of magnon BEC is a function of the spin wave stiffness constant (D) which is a function of E_A and since grain diameter (d) plays a major role in determining E_A , the size can tune the BEC of magnons.
4. Magnetic anisotropy energy E_A has a different temperature dependency in nanostructures (thin film, nanoparticle, nanowire, nanoribbon etc.) from its bulk material. The torque magnetometry which is generally using to find out E_A of bulk single crystals is difficult to use for nanostructures. Here current driven domain wall (DW) motion in artificially created nanoconstriction of 4f-ferromagnetic metal Gd has been done and find out the value of positive resistance coming from the DW. The DW thickness (δ) and correspondingly the anisotropy energy (E_A) were measured from the functional form of the DW resistance.
5. The important result we observed here is that T_{cm} value of GdCo alloy is not defined by E_A but by its T dependence as quantified by the derivative dE_A/dT . The rate dE_A/dT plays an important role to define T_{cm} and in nanostructure (here we use nanowire) since dE_A/dT is different from bulk, T_{cm} value also changes.

Scope for future works

1. The rigorous study of the low field MR on different Gd nanowire sample with different diameters could give a relation between diameter and the switching field H_S .
2. Detail study of the low temperature transition (~ 20 K) of Gd samples with sub 10 nm diameter grain size will make an another forward move towards the proposed physics which is based on Bose Einstein condensation (BEC) of magnons.
3. It is a challenge to make a Gd nanoconstriction of different widths and to make a detail study on current driven domain wall motion. The measurement could give the temperature dependent as well as the constriction width dependent anisotropy energy of different materials like 3d transition metals and its alloys.
4. The cheapest method, electrochemical deposition, could be used to make Gd_xCo_{1-x} nanowire for different value of x . The rigorous study of diameter dependent compensation temperature T_{cm} of this alloy nanowire could be done very easily.
5. The work function of Gd and GdCo is much smaller than other ferromagnetic material. Again the thesis showed that without changing composition the T_{cm} of GdCo alloy nanostructure can be shifted to the higher temperature. Therefore in future the alloy of GdCo may be rigorously used in high temperature (\gg room temperature) spintronic devices to reduce the Schottky barrier effect at contact pads. The RA (resistance \times contact area) factor of the device will also be reduced sharply. Therefore the result of the thesis could be used as an application in spintronic device system.

Appendix-1

Resistivity of Platinum (Pt) nanowire (NW) grown by FIB

Here four NWs were fabricated using the Dual Beam Helios 600 (FEI, Netherlands). The precursor molecule, methylcyclopentadienyl platinum trimethyl $(\text{CH}_3)_3(\text{CH}_3\text{C}_5\text{H}_4)\text{Pt}$, was first heated to around 48°C , and then the gas was introduced near the sample surface. The gallium ion (Ga^+) beam with four different beam energies was scanned over the defined area to form the C–Pt composite NWs. The beam current was in the range 28–30 pA in each case with a total beam diameter of about 42.5 nm. The length of the NWs was 20 μm with width and thickness of approximately 100 nm shown in FIG. A1(a). The dose for the Pt deposition used was maintained at $200\text{ pC}/\mu\text{m}^2$ for all the four beam energies. They were grown on a bi-layer substrate of approximately 190 nm thick silicon dioxide (SiO_2) on a 525 μm thick silicon (Si) wafer. The SiO_2 layer being insulating, does not allow any contribution of the Si substrate to the total conduction. Contact pads of Ag on a Cr adhesion layer were formed on the oxide layer by deposition through a silicon stencil mask.

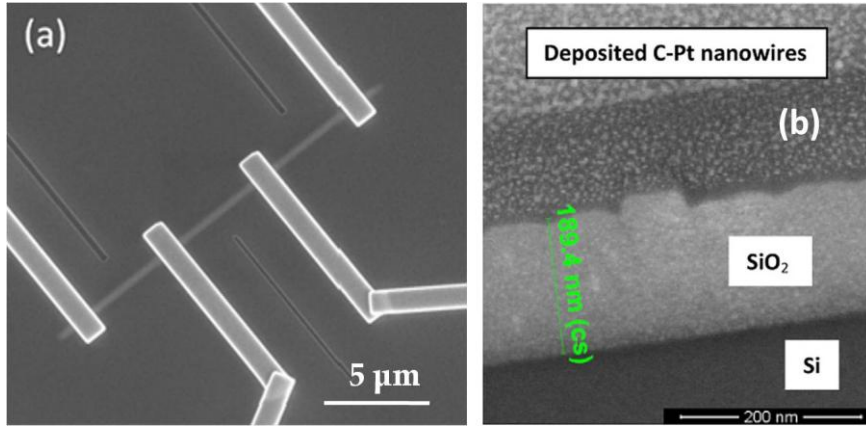


FIG. A1.1. (a) Four probe connection on FIB deposited nanowire of length 20 μm . (b) Cross section of FIB deposited C–Pt on SiO_2 coated Si wafer substrate. Pt islands are distributed in a carbon matrix.

In-situ Energy Dispersive X-ray (EDX) analysis using a Field Emission Scanning Electron Microscope (FE-SEM) was carried out to determine the composition of the wires grown by varying the Ga^+ ion accelerating voltage. EDX analysis confirmed that the FIB deposited NWs is a two-component composite conductor with low resistivity islands mostly composed of conducting materials (Pt + Ga) inside a high resistivity matrix composed principally of carbon. The volume fraction has been calculated from the atomic percentage obtained from EDX spectra using the relation:

$$V = \frac{At_{con} \times A}{\rho_m N} \quad (\text{A1.1})$$

, where V is the volume of the element with atomic concentration At_{con} obtained from the EDX spectra, A is the atomic weight, ρ_m is the mass density and N is the Avogadro number. Therefore the volume concentration (V_{con}) of the i th element can be expressed as,

$$V_{con}(i) = \frac{V_i}{\sum_i V_i} \quad (\text{A1.2})$$

Table A1.1: Volume concentration of conducting and non-conducting elements with FIB energy at 28 pA beam current ($\pm 0.1\%$) of four different NW samples.

Sample	Beam energy (keV)	At% (Pt)	At% (Ga)	At% (C)	Vol% of conducting component (Pt + Ga)	Vol% of nonconducting component (principally C)
S1	10	14.0	7.1	78.9	30.8	69.2
S2	20	16.2	7.3	76.5	33.7	66.3
S3	25	17.5	7.9	74.6	36.0	64.0
S4	30	17.2	8.9	73.9	37.0	63.0

With higher beam energy the beam profile gets narrower and hence the Ga incorporation in the nanowire also increases. Since the bulk electrical resistivities of Pt ($1.06 \times 10^{-8} \Omega\text{m}$) and Ga ($1.47 \times 10^{-8} \Omega\text{m}$) are three orders of magnitude smaller than that of amorphous carbon ($1.5 \times 10^{-5} \Omega\text{m}$), it can be reasonable to consider that the conducting clusters or nanoparticles consist of platinum and gallium dispersed in a nonconducting matrix which is mainly amorphous carbon. The average cluster size for the metallic regions is ≈ 7 nm with an average spacing ≈ 15 nm, as seen from the cross sectional data in FIG. A1.1(b).

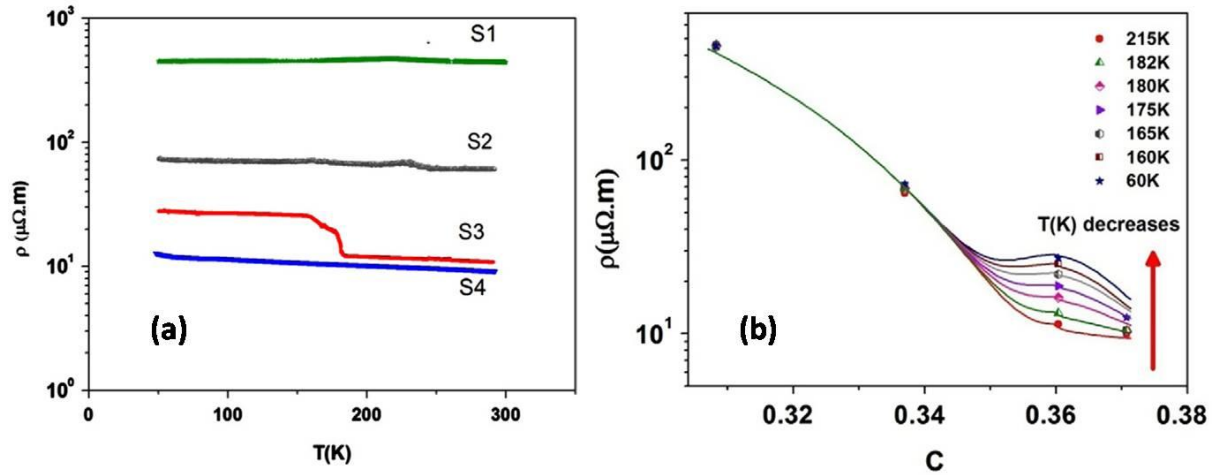


FIG. A1.2. (a) Resistivity vs. temperature of four NWs (b) Resistivity (ρ) vs. metallic concentration (C) for different temperatures.

The temperature dependent electrical resistivity shows that all the wires have a small negative temperature coefficient of resistivity (β). However, the sample S3, which has a metallic volume fraction of 36%, shows an anomalous jump in resistivity at ~ 150 K. A negative β is expected of a material where the majority matrix phase is an insulating material (amorphous carbon). For instance, $\beta \approx -0.0003 \text{ K}^{-1}$ for the sample S1 near room temperature, which is comparable to that of amorphous carbon $\beta \approx -0.0005 \text{ K}^{-1}$. The resistivity of the Pt NW decreases significantly with reduction in carbon concentration (increase of metallic phase concentration) when the wires are grown with higher voltage (see Table A1.1), and the effect flattens out beyond a total metallic phase concentration of 36% (17.5 at% Pt, 7.9 at% Ga), as shown in FIG. A1.2(b). We note that the resistivity decreases ~ 40 times for a variation of concentration from 31% to 36%, but changes only ~ 1.2 times for concentration variation from 36% to 37%. This type of behaviour is expected from a composite where the composition of the metallic phase is close to the percolation threshold. The

resistivity of such a composite changes rapidly as the percolation threshold is approached from the insulating side and once the metallic concentration is beyond the percolation threshold, the resistivity becomes somewhat insensitive to variation of the concentration. Therefore the NWs are basically a percolating system with involving a conducting phase of Pt (with some Ga) incorporated within a matrix which is predominantly C. The resistivity depends on the volume concentration v as,

$$\rho = \rho_0 + A|v - v_c|^k \quad (A1.3)$$

, where ρ_0 is the “background” resistivity of the C-Ga matrix and the second term is the percolation resistivity, subject to a threshold effect at the critical metallic volume concentration (CMVC) value v_c . Standard percolation theory suggests a value of $v_c \sim 30$ vol.%. This can be compared with our experimental result of $v_c \sim 36$ vol.%.

The anomalous behaviour in the temperature dependence of S3 needs special mention. This sample has the metallic phase concentration near the threshold value 36 vol.%. We observe reproducibly the anomalous temperature dependence of the resistivity, seen near 150 K. This is seen in FIG. A1.2(a) as a jump in resistivity in the temperature range 175 K to 150 K.

The difference in thermal expansion of composite material of NW and SiO₂ substrate will lead to a differential thermal strain $\Delta\varepsilon_T$ which is expressed as,

$$\Delta\varepsilon_T = (\alpha_{composite} - \alpha_{SiO_2})(T_{final} - T_{initial}) \quad (A1.4)$$

, where α is the thermal expansion coefficient. When temperature decreases, $\Delta\varepsilon_T$ will create a tensile stress at the NW, provided the adhesion is maintained. The tensile strain will increase the inter-particle separation of the Pt islands thus reducing the overall effective volume fraction. As stated earlier, near v_c , ρ is most sensitive to changes in this volume fraction and the effects of strain will be most visible. In particular, if the conduction is by tunnelling from one metallic grain to the next, the strain can change the conductance significantly as the inter-grain separation changes. This is because the tunnelling probability varies as the exponential of the inter-particle distance. The exact temperature at which the maximum change due to strain occurs will depend on the precise composition and its proximity to v_c .

In summary, the experiment suggests that the FIB fabricated Pt NW behaves as a percolating two-component system with a significant contribution to conduction arising from tunnelling between adjacent nanoparticles.

Reference:

Manotosh Chakravorty, K. Das, A. K. Raychaudhuri, J.P. Naik and P.D. Prewett, *Microelectronic Engineering*, **88**, 3360 (2011).

Appendix-2

Curie temperature (T_C) finding by Arrott plot

In the Weiss-Brillouin theorem the magnetization can be explained as,

$$M = M_0 \tanh \left[\frac{\mu(H + NM)}{k_B T} \right] \quad (A2.1)$$

, where M_0 is the spontaneous magnetization at absolute zero, μ is the moment per atom and N is the molecular field constant.

$$\frac{\mu H}{k_B T} + N \frac{\mu M}{k_B T} = \tanh^{-1} \left(\frac{M}{M_0} \right) \quad (A2.2)$$

Now for $M \ll M_0$,

$$\frac{\mu H}{k_B T} + N \frac{\mu M}{k_B T} = \frac{M}{M_0} + \frac{1}{3} \left(\frac{M}{M_0} \right)^3 + \frac{1}{5} \left(\frac{M}{M_0} \right)^5 + \dots \quad (A2.3)$$

In the limit of zero field

$$\frac{1}{\chi} = \frac{k_B T}{\mu M_0} - N \quad (A2.4)$$

At the Curie point $1/\chi = 0$ and therefore $T_C = (\mu N/k_B)M_0$. Hence at the Curie point

$$\frac{\mu H}{k_B T_C} = \frac{1}{3} \left(\frac{M}{M_0} \right)^3 + \frac{1}{5} \left(\frac{M}{M_0} \right)^5 + \dots \quad (A2.5)$$

Therefore Eqn. A2.3 can be rewritten as,

$$\frac{\mu H}{k_B T} = \epsilon \frac{M}{M_0} + \frac{1}{3} \left(\frac{M}{M_0} \right)^3 + \frac{1}{5} \left(\frac{M}{M_0} \right)^5 + \dots \quad (A2.6)$$

, where $\epsilon = (T - T_C)/T$. After neglecting the higher order terms the above equation can be re-written as,

$$M^2 = 3M_0^2 \epsilon + \frac{3\mu M_0^3}{k_B T} \left(\frac{H}{M} \right) \quad (A2.7)$$

At $T = T_C$, $\epsilon = 0$ and M^2 vs. H/M curve becomes a straight line.

The above equation can be corrected as,

$$M^{\frac{1}{\beta}} = 3M_0^2 \epsilon + \frac{3\mu M_0^3}{k_B T} \left(\frac{H}{M} \right)^{\frac{1}{\gamma}} \quad (A2.8)$$

Again,

$$M_S(T) = M_0 b (-\epsilon)^\beta, \epsilon < 0$$

and

$$\chi_i^{-1}(T) = \chi_0^{-1} c \epsilon^\gamma, \epsilon > 0$$

, where M_S is the saturation magnetization and χ_i is the susceptibility at a particular field H . The critical exponent β and γ can be determined from the fitting of the above equations with the experimental results. At $T = T_C$, $M_S^{\frac{1}{\beta}} = 0$.

In this thesis we were using Arrott plot to determine the Curie temperature of three different Gd samples of different grain sizes. The samples were bulk Gd ingot (Bulk), thick film of thickness 1.9 μm (Film-A) and another film of thickness 250 nm (Film-B).

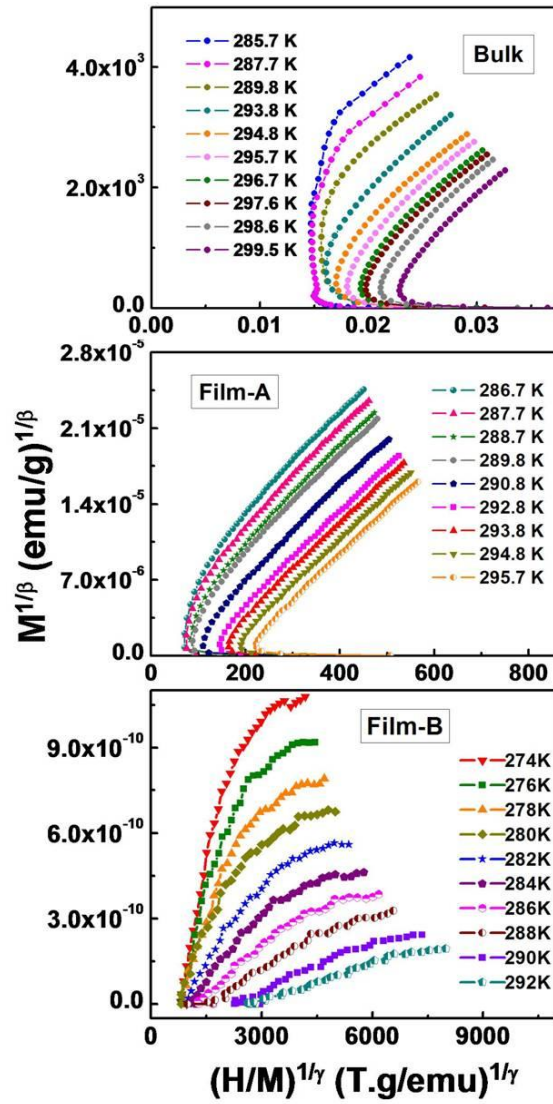


FIG. A2.1. Arrott plot of Bulk, Film-A and Film-B.

Table A2.1: Results of the Arrott plot experiment.

Sample	Grain size (μm)	β	γ	T_C (K)
Bulk	4	0.529	1.063	291.4
Film-A	0.105	0.514	0.968	290.2
Film-B	0.035	0.333	0.879	286.5

Reference:Anthony Arrott, *Phy. Rev.*, **108**, 1394 (1957).

Appendix-3

Magnon number density calculation

$$n = \frac{1}{2\pi^2} \left[\int_0^{\infty} \frac{k^2 dk}{e^{\beta(Dk^2 + \Delta)} - 1} - \int_0^{k_0} \frac{k^2 dk}{e^{\beta(Dk^2 + \Delta)} - 1} \right]$$

$$\text{or, } n = \frac{I_0}{2\pi^2} - f(T, d)$$

$$\text{Therefore, } I_0 = \frac{1}{2(\beta D)^{3/2}} \int_0^{\infty} \frac{(x - \Delta\beta)^{1/2} dx}{e^x - 1}$$

$$= \frac{1}{2(\beta D)^{3/2}} \int_0^{\infty} (x - \Delta\beta)^{1/2} e^{-x} (1 - e^{-x})^{-1} dx$$

$$= \frac{1}{2(\beta D)^{3/2}} \int_0^{\infty} (x - \Delta\beta)^{1/2} e^{-x} (1 + e^{-x} + e^{-2x} + \dots) dx$$

$$\text{Let, } x - \Delta\beta = z$$

$$= \frac{1}{2(\beta D)^{3/2}} \int_0^{\infty} z^{1/2} e^{-z} e^{-\Delta\beta} (1 + e^{-z} e^{-\Delta\beta} + e^{-2z} e^{-2\Delta\beta} + \dots) dz$$

$$= \frac{\Gamma(3/2)}{2(\beta D)^{3/2}} \left(\frac{e^{-\Delta\beta}}{1^{3/2}} + \frac{e^{-2\Delta\beta}}{2^{3/2}} + \frac{e^{-3\Delta\beta}}{3^{3/2}} + \dots \right)$$

$$= T^{3/2} \left(\frac{k_B}{D} \right)^{3/2} \frac{\sqrt{\pi}}{4} \sum_{l=1}^{\infty} \frac{e^{-l\Delta\beta}}{l^{3/2}}$$

Appendix-4

Domain wall resistance of constricted nonuniform structure

The calculation of domain wall (DW) resistance is shown below.

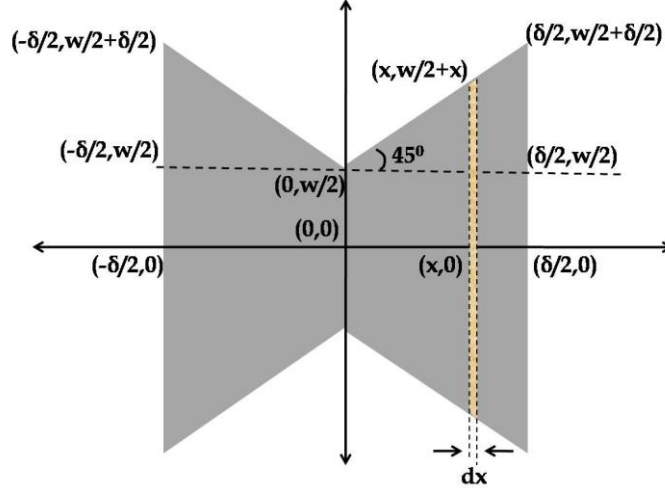


FIG. A4. 1. Schematic diagram of DW at the constriction. The coordinate at the centre of the constriction is (0,0).

The thickness of the constriction is w . The DW of width δ is created around the constriction. We consider a strip dx at a distance x from the centre of the constriction. If ρ_w is the DW resistivity and t is the thickness of the film, the DW resistance R_w can be written as,

$$R_w = 2 \int_0^{\delta/2} \frac{\rho_w dx}{(w + 2x)t}$$

Here 2 come due to the series combination of the same resistance present at the both side of the x-axis.

$$\begin{aligned} R_w &= \frac{2\rho_w}{wt} \int_0^{\delta/2} \frac{\rho_w dx}{\left(1 + \frac{2x}{w}\right)} \\ &= \frac{\rho_w}{t} \int_1^{1+\delta/w} \frac{dz}{z} \\ &= \frac{\rho_w}{t} \ln \left(1 + \frac{\delta}{w}\right) \\ \frac{R_w t}{\rho_w} &= \frac{\delta}{w} - \frac{\delta^2}{2w^2} + \frac{\delta^3}{3w^3} - \dots \end{aligned}$$

Since $\delta \ll w$, we can neglect the higher order terms $\left(\frac{\delta}{w}\right)^3, \left(\frac{\delta}{w}\right)^4 \dots$ etc. Again $\rho_w = \frac{\varphi^2 \rho_0 \alpha_T}{5\delta^2}$. Therefore,

$$\frac{5R_w t \delta^2}{\rho_0 \varphi^2 \alpha_T} = \frac{\delta}{w} - \frac{\delta^2}{2w^2}$$

$$\delta = \frac{2w}{\left(\frac{10R_w w^2 t}{\rho_0 \varphi^2 \alpha_T} + 1\right)} = \frac{\varphi^2 \rho_0 \alpha_T}{5wtR_w} \left(1 + \frac{\rho_0 \varphi^2 \alpha_T}{10R_w w^2 t}\right)^{-1}$$

$$\delta = k \frac{\varphi^2 \rho_0 \alpha_T}{5wtR_w}$$

$$k = \left(1 + \frac{\rho_0 \varphi^2 \alpha_T}{10R_w w^2 t}\right)^{-1}$$

Table A4.1: The value of k at different temperatures.

T (K)	100	126	150	170	215	235	250
k	0.9770	0.9670	0.9560	0.9540	0.9520	0.9518	0.9516